Investigation of Fore-Aft Element Connectors for an ultra-efficient Slotted, Natural-Laminar-Flow Aircraft Wing

A Dissertation Presented for the
Doctor of Philosophy
Degree
The University of Tennessee, Knoxville

Corey Michael Arndt
December 2022

Copyright © 2022 by Corey Michael Arndt.
All rights reserved.

ACKNOWLEDGEMENTS

To begin I would like to provide a generic thank you to the many people whom I have met along the way. From the kids who played football in the backyard, the students and teachers that made learning and sports fun during elementary and high school, the coworkers at my first job at Walgreens, the many friends at Penn State that stretched my social boundaries, or the fellow graduate students I've met during my graduate studies, be it that you left a footprint or a trail, I am forever grateful for the memories. Regardless if you are still active in my life or not, I wish you the best always.

Thank you to my family for their support and bolstering of my intellectual ego for as long as I can recall. I am not the most affectionate person and don't call as much as I should, but your support has and will always be appreciated.

To my Pittsburgh friends, thank you for many hours of games and events we've shared together. The time you took to hang out with me when I would come home from Penn State or Tennessee was invaluable. I cherish our group chats and your ability to take me out the head space academia puts me in. You may not have always understood my research, but you've listed to my complaints nonetheless. Here's to our adventures and the many to come.

WE ARE … Yeah you should be expected to fill that in, even if it is in text. Penn Staters, thank you so much for helping me come out of my shell with your antics. Our years together at Penn State and our friendship after has given me many memories that I hope we can recall in the coming years, even when we are old. From late night boardgames, monkey boys, football tailgates, and even weddings I can't thank you enough for the fun times. Fourth Floor let's make sure to meet up over the years.

To my graduate research group, the ones who were there when I started and the ones am leaving, thank you for helping me over the years and providing an ear. Having a group to chat about research issues with is sometimes all it takes to move a project along. You are some of the smartest people I have met, and I hope to see the rest of you graduate. I wish we would have done more events together, but between research and a global pandemic I guess group meetings and weekend porch chilling will have to suffice.

I would like to thank Dr. William Ferrell who falls into two of these groups. Your friendship at Penn State helped me become more social and step out of my boundaries. We shared a lot of good nights with our friends. You made me reach out to Dr. TerMaath and enter graduate school. I am grateful for that encouragement. The many lessons on graduate life allowed me to tutor our friend Cody Crusenberry. I am also thankful for the animals, Astrid and Loki, that you housed. I told myself I wouldn't get a pet while in school and being able to petnap them was wonderful. Your friendship has been much appreciated and I can't wait to join you for your wedding in Iceland.

Dr. Stephanie TerMaath, thank you so much for the amazing support and guidance you have provided over my graduate career at the University of Tennessee. I would not have grown into the researcher I am today without your support. I look forward to wrapping up remaining papers and working with you in the future as peers.

I also wish to express my thanks to the faculty members who agreed to serve on my Ph.D. committee and for their patience on my dissertation. Thank you for your support, Dr. Reza Abedi, Dr. Richard Bennett, and Dr. Russell Zaretzki.

Financial support was partially provided by the Office of Naval Research (ONR) Structural Reliability Program through grant N00014-21-1-2041 under the direction of Dr. Paul Hess.

This material is partially based upon work supported by the National Aeronautics and Space Administration (NASA) under cooperative agreement award number NNX17AJ95A. The work was performed under the University Leadership Initiative (ULI) led by the University of Tennessee, Knoxville "Advanced Aerodynamic Design Center for Ultra-Efficient Commercial Vehicles". Any opinions, findings, and conclusions or recommendations expressed in this material are those of the author(s) and do not necessarily reflect the views of NASA.

The author thanks Dr. Daniel Hart (Naval Surface Warfare Center, Carderock Division) for providing experimental data, assisting in metal/composite hybrid manufacturing, providing initial literature for DIC, and overall review of some of the work provided in this dissertation.

The author thanks Dr. Adam Sobey (The Alan Turing Institute) for guidance and insight for the application of neural networks to generate the surrogate models utilized in this dissertation.

ABSTRACT

The SNLF [slotted, natural-laminar-flow airfoil] is a revolutionary technology projected to contribute significant decreases in fuel consumption and carbon emissions. The SNLF is designed to allow favorable pressure gradients to extend further aft increasing the extent of laminar flow achievable to about 90% of the entire airfoil, thus reducing the wing profile drag and subsequently fuel consumption. The SNLF is not without its complexity as it introduces several design challenges to maintain laminar flow. The slot width must be maintained during flight to engage the favorable pressure gradients that enable these benefits. As such a crucial aspect for implementing this technology is how the two elements of the slotted airfoil are joined. The slot connectors must be adequately analyzed to transfer the induced high-lift from the aft element while ensuring minimal impedance on the laminar flow within the slot. This dissertation presents the analyses and considerations for the slot connectors including their overall placement within the slot, size, and shape with the effects they have on the structural components of the aircraft half-span wing. Investigations using finite element (FE) modeling, computational fluid dynamics (CFD), and topology optimization inform of potential material distributions and design considerations to ensure the slot connectors transfer the load while maintaining the slot width. To further evaluate potential weight reduction the adhesive joining of composite overlay to a metallic substrate is investigated with the use of non-deterministic approaches including global sensitivity analysis, surrogate modeling, and reduced order modeling.

Table of Contents

Chapter One Introduction 1
Chapter Two Slotted, Natural-Laminar-Flow Airfoil: A Revolutionary Technology for Fuel Efficiency 6
Preface 6
Introduction 6
Challenges of Achieving Laminar Flow & SNLF Airfoils 8
The SNLF Airfoil Development Timeline 10
S103, SNLF Airfoil 20
S204, SNLF Airfoil 20
S414, SNLF Airfoil 22
S207, SNLF Airfoil 25
X207LS, SNLF Airfoil 28
Current SNLF Research 30
Aerodynamics 30
Structures 35
Advanced Technologies 38
Future Goals and Conclusions 40
Chapter Three A review 42
Aft-Loading on Airfoil 42
Flaps 45
Topology Optimization 46
Chapter Four Aero-structural Considerations of Fore-Aft Element Connectors for a Slotted, Natural-Laminar-Flow Airfoil 52
Introduction 52
Study I: Location and Shape Effects 52
Technical Approach for Location and Shape Effects 53
Results for Location and Shape Effects 55
Study II: Transonic Size and Location Study 59
Technical Approach for Transonic Size and Location Study 62
Results for Transonic Size and Location Study 62
Study III: Investigation of Slot Connector Number and Size 67
Technical Approach for Slot Connector Number and Size Study 67
Results for Transonic Number and Size Study 71
Conclusions and Current Work 73
Chapter Five Topology Optimization of the AFT Element 76
Introduction 76
Technical Approach 76
Results and Discussion 82
Conclusions and Manufacturability 86
Chapter Six Full Half-Span Wing Structural Demonstration 90
Introduction 90
Technical Approach 90

Results 98
Conclusion 103
Chapter Seven Nondeterministic Parameter Space Characterization of the Damage Tolerance of a Composite/Metal Structure 106
Preface 106
Introduction 106
Materials and Methods 108
Hybrid Structure Configuration 108
Experimental Testing 108
Computational Simulation 111
Non-deterministic Parameter Study 125
Results and Discussion 130
Computational Validation and Results 130
Surrogate Modeling of Total Energy Absorption 130
GSA of Total Energy Absorption 134
UQ of Total Energy Absorption 134
Reduced Order Surrogate Modeling with FDR LogWorth 137
Parameter Mapping of Total Energy Absorption and Subsectional Energies 137
GSA for Subsectional Energies with Reduced Order Models 143
Equational Comparison of the Total Energy Absorption to the Reduced Order Subsectional Energies 147
Conclusion 152
Chapter Eight Conclusions and Recommendations 153
List of References 155
Vita 165

LIST OF TABLES

Table 2-1: Various SNLF airfoil models and the corresponding design specifications [36]. 19
Table 4-1: Variables for take-off conditions for the S207 [5] 54
Table 4-2: Material Properties for Aluminum 6061 [84] 54
Table 4-3: Number of C3D10 elements for each Connector for shape and location study 56
Table 4-4: Flight Conditions used for the CFD analyses for shape and location study 57
Table 4-5: Aerodynamic coefficient changes due to introduction of connectors D and F 61
Table 4-6: Material Properties for Ti-6Al-4V 63
Table 4-7: Number of C3D10 elements comprising the slot connectors. 66
Table 4-8: Material Properties for Al 6061, A36, and Ti-6Al-4V 72
Table 4-9: Slot connector size and locations. 74
Table 5-1: Twist angle provided for various span locations for the S207 SNLF airfoil 77
Table 5-2: ETA information for the S207 SNLF Airfoil utilized for generation of aft element topology. It should be noted that the numbers below have been rounded for simplicity of showing. 79
Table 5-3: Cruise flight conditions for the S207 SNLF airfoil 83
Table 6-1: Material Properties for Toray M35J 93
Table 6-2: Aft Element Rib Thickness 95
Table 6-3: Aft Element Skin Panel Thickness 95
Table 6-4: Fore Element Individual Spar Loads 95
Table 6-5: S207 SNLF Wing EI and GJ Requirements 96
Table 6-6: Fore Element Rib Thickness 99
Table 6-7: Fore Element Skin Panel Thickness 99
Table 6-8: Number of C3D10 Elements for the Slot Connectors. 101
Table 7-1: Elastic and plastic properties for aluminum 5456-H116 119
Table 7-2: Mechanical properties of resin between laminate plies 121
Table 7-3: Mechanical properties of resin between composite/metal interface 121
Table 7-4: Mechanical Properties of Laminates I 122
Table 7-5: Mechanical Properties of Laminates II 122
Table 7-6: Mechanical Properties of Laminates (Laminar Shear) 123
Table 7-7: Total index vs. FDR LogWorth 135
Table 7-8: Convergence study for UQ 135
Table 7-9: UQ analysis results with 5,000 data points 136
Table 7-10: FDR LogWorth for the three subsection energies 138
Table 7-11: FDR LogWorth for two subsection energies 139
Table 7-12: Reduced order surrogate results for the five subsection energies 139
Table 7-13: Reduced Order Modeling Error with Interface Contribution 151
Table 7-14: Reduced Order Modeling Error without Interface Contribution 151

LIST OF FIGURES

Figure 1-1: Total fuel consumed and number of passengers of U.S. carriers (both national and international) over the past decade with predictions for the next 20 years [1]. 2
Figure 1-2: S207 SNLF airfoil developed by Somers [5]. 2
Figure 1-3: SNLF aircraft wing's relative placement on a generic fuselage. 4
Figure 2-1: Total Domestic and International U.S. Passenger Traffic for U.S. Commercial Air Carriers; Historical and Projected Jet Fuel and Aviation Fuel Consumptionm by U.S. Civil Aircraft [1]. 7
Figure 2-2: Comparison of the sections and Cp plots for (a) NACA 23012 [23] and (b) NACA 27-215 [24] airfoils. 11
Figure 2-3: (a) Section of a 6 series airfoil, NACA 653-018 with a plot of (v/V)2 which is analogous to Cp and (b) Comparison of the minimum section drag coefficient across different NACA airfoils for a wide range of Reynolds number, together with laminar and turbulent flow [25]. 12
Figure 2-4: Comparison of (a) flow characteristics and (b) Cp plots of conventional (example NACA 6-series) and NASA supercritical airfoils at supercritical Mach numbers [27]. 13
Figure 2-5: NLF(1)-0215F airfoil shape and inviscid, incompressible velocity distributions (analogous to Cp plots) [31]. 15
Figure 2-6: (a) Original slotted, supercritical airfoils [12] (b) MDA 3-element high lift airfoil [14]. 17
Figure 2-7: Depiction of pressure distribution for an SNLF airfoil (from patent) [6]. 17
Figure 2-8: Compilation of the SNLF airfoil shapes with design annotations [36]. 18
Figure 2-9: Timeline of the development and testing of various specialized SNLF airfoils [36]. 18
Figure 2-10: Pressure distribution over the SNLF, S103 airfoil at the design point (cruise). Note that 'ls' and 'us' are abbreviations for the lower and upper surfaces, respectively. 21
Figure 2-11: Results for SNLF, S103 airfoil (a) Comparison of theoretical and experimental pressure distributions for Re = 3 x 10^6, M = 0.10 and α = -1.07° with transition free [15]. Open symbols represent data for upper surface; crossed symbols, data for lower surface. (b) Comparison of theoretical and experimental section characteristics (cl vs. cd and cl , cm vs. α) at Re = 3 x 10^6 and M = 0.10 with transition free [15]. 21
Figure 2-12: Theoretical pressure distribution for the SNLF, S204 airfoil at M = 0.65 and Re = 12 x 10^6 for α= -1° and -2° transition free. 23
Figure 2-13: Theoretical transition locations and section characteristics for the SNLF, S204 airfoil at M = 0.10 and Re = 3 x 10^6 [34]. 24
Figure 2-14: Section characteristics for the SNLF, S204 airfoil at M=0.70 and Re= Re = 2.26 x 10^6 [34]. 24

Figure 2-15: Results for SNLF, S414 airfoil: (a) Comparison of theoretical and experimental pressure distributions at $c_l = 0.518$ and $Re = 1.5 \times 10^6$ [Coder-15] (b) Comparison of predicted and measured section characteristics for $Re = 1.5 \times 10^6$ [21]. 26
Figure 2-16: Results for SNLF, S207 airfoil at $Re=13.2 \times 10^6$: (a) Effect of lift coefficient on predicted pressure distribution at M = 0.71 [6] (b) Lift and pitching moment at various Mach numbers [Coder-6] and (c) Profile drag at various Mach numbers [Coder-6] and (d) Impact of Gortler instabilities on profile drag at M = 0.71 [19]. 27
Figure 2-17: (a) Effect of compressibility on SNLF, S207 surface pressure distributions for fixed $Re=13.2 \times 10^6$ (b) Pressure distributions for the SNLF, S207 and SNLF, X207LS at their respective design Mach numbers and $Re=13.2 \times 10^6$ [35]. 29
Figure 2-18: Performance of the SNLF, X207LS airfoil at various Reynolds numbers: (a) Lift and pitching coefficients and (b) Profile drag [35] 29
Figure 2-19: Configuration of the Boeing Transonic, Truss-Braced Wing [41]. 31
Figure 2-20: Effect of Flap Deflection on the Flow Structure near Maximum Lift [42]. 33
Figure 2-21: Digitized S207 NSU2D Results with Implemented Transition Model for Mach = 0.7, $\alpha = -1.3°$, $Re = 13.2 \times 10^6$. Provided Courtesy of the Mavriplis CFD Lab. (a) Mach Flow Field of S207, SNLF Airfoil. (b) Convergence History. 34
Figure 2-22: Comparison of the turbulent viscosity ratios of a 200" baseline region with no connector A) and a circular connector B). 36
Figure 2-23: The adjusted NASA CRM shape utilized for the fore-aft element connector study. 36
Figure 2-24: Weight of various connector numbers required to transfer flight loads from aft element to fore element. 37
Figure 2-25: Drag acting on various connector numbers showing impedance of local laminar flow in the slot. 37
Figure 2-26: Overview of fore and aft element rib and spar placements. Green dictates fore element components and blue indicates aft element components. 39
Figure 2-27: Mach Contours of baseline flow (left) and active flow control applied along the slot (right) at $\alpha=26°$. Provided courtesy of Boeing Research and Technology. . 39
Figure 3-1: Cp plot distributions for Cruise Conditions of the S207 SNLF airfoil with Cl = 0.70 and $Re = 13.2 \times 10^6$ [19]. 43
Figure 3-2: Cp plot distributions for Take-off conditions of the S207 SNLF airfoil with M = 0.225 and $Re = 16.0 \times 10^6$ [19]. 44
Figure 3-3: Comparison of a single element airfoil, NASA CRM (left), to a slotted airfoil, S207 (right). Graphs depict the Cp of the two airfoils [19]. 44
Figure 3-4: Categories of Optimization Methods [69]. 48
Figure 3-5: Airbus Topology, Sizing, and Shape Optmization Process [70]..... 51
Figure 4-1: The eight connector shapes studied for shape and location effects. 54
Figure 4-2: Generic Mesh cross-section for shape and location study. 56
Figure 4-3: Tetrahedral mesh generation for connectors for shape and location study… 56
Figure 4-4: Stress buildup in the eight different connectors detailing yielding in five of the shapes. 57

Figure 4-5: Max deflection of aft element for several of the connector shapes evaluated. 58
Figure 4-6: Eddy Viscosity ratio displaying the difference between a section with no connector, and external connector, and an internal connector. 60
Figure 4-7: Separation of flow occurring around the connectors compared to a clean, no connector, section. 61
Figure 4-8: Adjusted CRM.65 blunt shape. Camber removed and mirrored to upper surface. 63
Figure 4-9: General Mesh for the Fore and Aft element finite sections utilized for several of the studies in Ch. 4. 64
Figure 4-10: General Mesh generation for slot connector utilized for size and locations studies. 65
Figure 4-11: A) Slot connector placed in the lower region of the slot. B) Slot connector placed in the middle region of the slot. C) Slot connector placed in the upper region of the slot..... 66
Figure 4-12: FE results detailing the collapse of the slot region when the slot connector was placed in the lower region of the slot..... 68
Figure 4-13: FE results for the max deflection of the aft element for the middle and upper region slot connectors. 68
Figure 4-14: FE results comparing yielded elements in middle and upper region slot connectors. 69
Figure 4-15: Weight of various connector numbers required to transfer flight loads from aft element to fore element. 72
Figure 4-16: Drag acting on various connector numbers showing impedance of local laminar flow in the slot. 74
Figure 5-1: CAD model detailing the half-span wing utilized for aft element topology. 77
Figure 5-2: Unit shape of the S207 SNLF airfoil developed by Somers [5]. 80
Figure 5-3: Mesh for aft element skin with C3D8R elements. 80
Figure 5-4: Mesh for design region of the aft element using C3D8R elements. 81
Figure 5-5: Cp plots for the S207 SNLF airfoil for various span locations..... 81
Figure 5-6: Pressure distribution on the aft element for utilized for the topology optimization. 83
Figure 5-7: Half-span wing material distribution informed by topology optimization of the aft element with displacement control. 83
Figure 5-8: Material distribution underneath the connectors illustrating the ribs. 84
Figure 5-9: Trailing edge view of the material distribution underneath a connection and along the span between two connection points. 84
Figure 5-10: Material distribution of the tip region for the aft element under topology optimization. 84
Figure 5-11: Interior view of tip region of the aft element demonstrating increased skin gauge across the span. 85
Figure 5-12: Half-span wing material distribution informed by topology optimization of the aft element without displacement control. 87

Figure 5-13: Material distribution underneath the connections without displacement control. 87
Figure 5-14: Deformation of the upper skin region between two connectors for the topology optimization with displacement control. 88
Figure 5-15: Deformation of the upper skin region between two connectors for the topology optimization without displacement control. 89
Figure 6-1: Fore element geometric illustration. 91
Figure 6-2: Aft element geometric illustration. 92
Figure 6-3: Generic slot connector geometric illustration. 92
Figure 6-4: Representation of loading input into VisualAnalysis Edu for wing strut calculations. 96
Figure 6-5: Fore element spar thickness at various spans. 97
Figure 6-6: Overview of fore and aft element rib and spar placements. Green dictates fore element components and blue dictate aft element components. 100
Figure 6-7: Representation of fore element spar locations and slot connector location within the slot. 101
Figure 6-8: Y-direction (upwards) deflection of the entire FE model. 102
Figure 6-9: Stress build-up on the aft element skin and ribs underneath the slot connectors. 104
Figure 6-10: Comparison of fore element ribs with stress build-ups. Eta 0.8125 (upper) is representative of the fore element ribs without slot connectors attached. Eta 0.8750 (bottom) is representative of fore element ribs with a slot connector attached. 105
Figure 6-11: Fore element rib displaying tension stress caused by strut brace connection. 105
Figure 7-1: Integrated approach to characterize the parameter space. 109
Figure 7-2: Stacking sequence of composite/metal hybrid structure. 110
Figure 7-3: a) Representation of Experimental Configuration. b) DIC image captured to display speckling pattern [142]. 112
Figure 7-4: CZM triangular traction-separation law. 116
Figure 7-5: Color gradation for data quality. 118
Figure 7-6: a) FE model illustrating the different layers. b) Breakdown of FE model illustrating the damage models for each aspect. 124
Figure 7-7: Visualization of surrogate model generation and use. 127
Figure 7-8: Validation of FE model illustrated by the comparison of experimental force-displacement curves vs the simulation. Original graph provided courtesy of Heng et al. [142]. 131
Figure 7-9: DIC results compared to the simulation for further validation. Original images provided courtesy of Heng et al. [142]. 131
Figure 7-10: Distribution of energies absorbed by the FE model. 132
Figure 7-11: Error of 25 randomly selected data points generated by the surrogate model. 133
Figure 7-12: Sobol indices for the 41 parameter space. 135
Figure 7-13: 4-dimensional parameter space visualization contoured with the total energy absorbed. 141

Figure 7-14: 3-D mesh contours for plastic deformation in the aluminum substrate. ... 141
Figure 7-15: 3-D mesh contours for shear plasticity in the composite overlay. 142
Figure 7-16: 3-D mesh contours for interlaminar fracture in the composite overlay. ... 144
Figure 7-17: 3-D mesh contours for intralaminar delamination in the composite overlay. 144
Figure 7-18: 3-D mesh contours for interface disbond between the metal substrate and the composite overlay. 145
Figure 7-19: Sobol indices for plastic deformation in the aluminum substrate. 146
Figure 7-20: Sobol indices for shear plasticity in the composite overlay. 148
Figure 7-21: Sobol indices for interlaminar fracture in the composite overlay. 149
Figure 7-22: Sobol indices for intralaminar delamination in the composite overlay. ... 150

Chapter One

Introduction

Traveling is an integral part of everyday life. People travel to work, to visit friends and family, and to enjoy vacations. Traveling by aircraft is one of the most widely used and safest methods of transportation. As such, the aerospace industry consumes billions of gallons of fuel costing billions of dollars each year. Figure 1-1 illustrates the expected rise of future aircraft enplanements for United States carriers [1-4]. Enplanements and fuel consumption have been climbing since the early 2010's. The only deviation occurred during the COVID pandemic which resulted in a sudden drop in enplanements and fuel consumption. However, aircraft enplanements are predicted to recover in a few short years. As enplanements continue to rise so will fuel consumption. The continual increase in fuel consumption has two major concerns. Firstly, growth in fuel consumption contributes to the destructive impact humanity is having on the global climate. The highest levels of carbon emissions and heat indexes are being observed. Changes to the way humans travel are pivotal in reducing humanity's carbon footprint. The second major concern is the supply of oil. Global economic policies greatly impact the price of oil. Wars, change in leadership or alliances, pressure from outside influences, and many other factors can affect the price of oil on the global market. The price of oil can be sporadic and has the potential to greatly affect the aerospace industry. Another concern with the supply of oil is the limitation of its production. Many predictions can be made about when humanity will run out of non-renewable resources, with several stating as early as the year 2050. These compounding concerns highlight the need for innovation in the aerospace industry. Greener technology can be a major way to stem the growth in fuel consumption and reduce the aerospace industry's carbon footprint and annual running cost.

One of the state-of-the-art technologies that is helping to revolutionize the aerospace industry is the slotted, natural-laminar-flow (SNLF) airfoil. This technology is expected to contribute to fuel consumption reduction with its implementation on aircraft such as the Boeing 737 and aircraft with similar enplanements around 150. SNLF airfoils have been under development for several years with several iterations having been investigated. The particular airfoil utilized for this dissertation is the S207 SNLF airfoil developed by Somers at Airfoils, Inc. as shown in Figure 1-2 [5]. The SNLF airfoil provides additional benefits without advanced technology development. The introduction of the slot allows for favorable pressure gradients to form and extend further aft when compared to traditional single element airfoils [6, 7]. The fore element of the SNFL airfoil is entirely laminar while the aft reaches 80%. The favorable pressure gradients reduce the streamwise instabilities on the boundary layer and decrease the drag while increasing the lift. The proposed benefits can help reduce the fuel consumption of the aircraft.

However, the SNLF airfoil introduces several new design challenges that need to be addressed. The SNLF airfoil differs from most traditional single element airfoils with its aft element producing a considerable amount of lift during both take-off

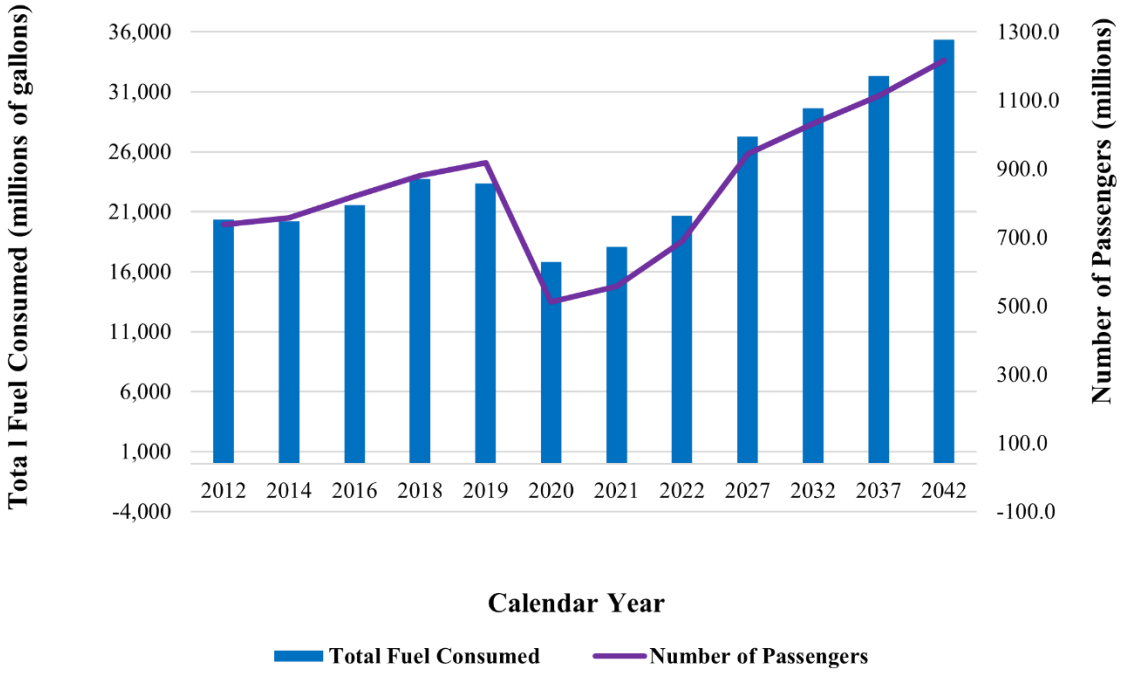


Figure 1-1: Total fuel consumed and number of passengers of U.S. carriers (both national and international) over the past decade with predictions for the next 20 years [1].

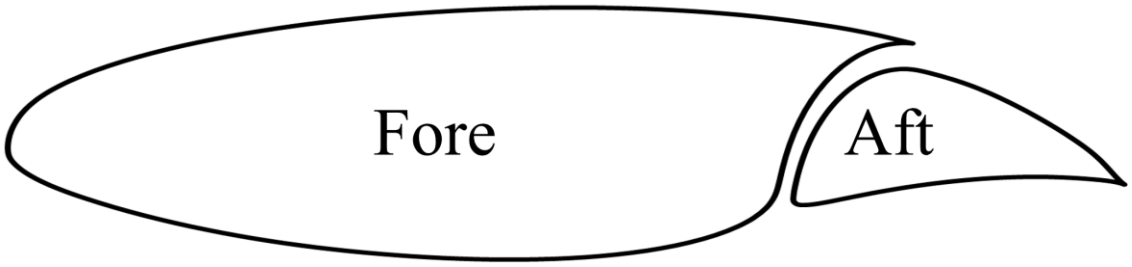


Figure 1-2: S207 SNLF airfoil developed by Somers [5].

and cruise conditions. The slot also creates a ‘floating’ aft element, is not connected to the fuselage, and must be supported by the fore element’s rear spar. The relative placement of the fore and aft elements is detailed in Figure 1-3. These two design considerations raise a vital question in how to connect the high-lift aft element to the fore element without excessive weight or blockage of the laminar flow through the slot. Another interesting consideration is the material distribution within the aft element required to transfer the load. The focus of this dissertation is on the connectors placed within the slot and their effects on the material distribution in the aft element needed for structural integrity.

The following chapters in this dissertation explore how to efficiently transfer load from the aft element to the fore element with the use of slot connectors while minimizing weight, reducing impedance on the laminar flow through the slot, and highlighting potential material distribution and properties for design considerations. These structural investigations are performed with the state-of-the-art S207 SNLF airfoil previously discussed [5]. This airfoil causes new loading scenarios and complex constraints on the laminar and weight goals. The main focus is on the slot connectors utilized to transfer load from the aft element to the fore element. Prior to a full analysis of the topology of the wing, the connectors are investigated with several analyses including shape, location, number, and size. The goal of these analyses is to develop a slot connector that transfers the load and reduces its local effects on the laminar flow through the slot. Structural analysis was informed by computational fluid dynamics (CFD) to perform these analyses. Material distribution within the aft element was also investigated to determine if a traditional spar and rib wingbox was required or if a reduced component wingbox could be used to assist in weight goals. This was performed with topology optimization to highlight where material was most needed. A final full topology of the fore element, aft element, and slot connectors was generated to demonstrate the behavior of the two-element wing with the previous considerations. To assist in weight reduction goals adhesive joining was investigated. In the scope of this dissertation, adhesive joining was considered for the joining of the slot connectors to the fore and aft elements instead of traditional bolts or rivets. However, adhesive joining leads to complex parameter spaces. The investigation for the dissertation evaluates the complex parameter space of adhesive joining using non-deterministic methods such as global sensitivity analysis, surrogate modeling, and reduced order modeling. This is done to investigate the feasibility of reducing complex interacting damage mechanisms to better understand the design considerations that can assist in implementing the slot connectors.

This dissertation is broken into several chapters with a short description listed below to reiterate the previously discussed goal of each chapter.

Chapter Two describes the revolutionary concepts behind the SNLF airfoil. This includes the development of natural-laminar-flow over the years and the evolution of the SNLF airfoil itself. It expands on the aerodynamic concepts of the SNLF and how it is assisting in reducing fuel consumption with NLF. It highlights the major differences in aerodynamics compared to traditional single element airfoils.

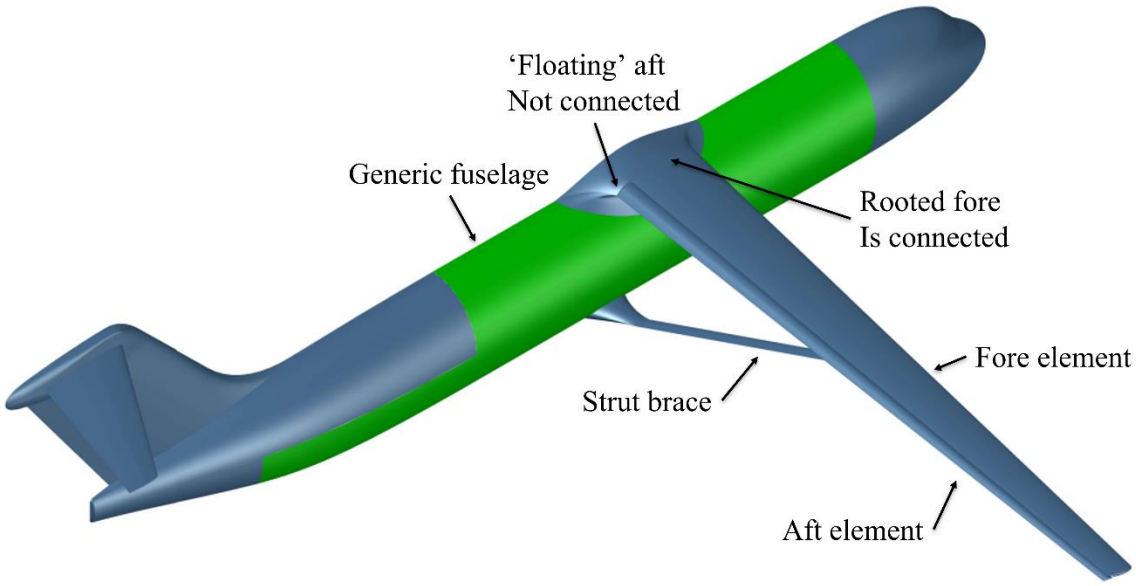


Figure 1-3: SNLF aircraft wing's relative placement on a generic fuselage.

Chapter Three is a literature review for topics not discussed in Chapter Two. Topics included are the main differences in the loading scenario of the SNLF airfoil when compared to single element airfoils. The SNLF has a high-lift aft element and behaves similarly to aft loaded single element airfoils. Currently employed connections for control surfaces are also explored to explain how these connectors differ than current implementations. The last topic is topology optimization.

Chapter Four focuses on the exploration of the structural and aerodynamic considerations when investigating the slot connectors required to support the aft element. This chapter features three studies. The first focuses on the general shape and location of the slot connectors. Finite element (FE) models and CFD are utilized to explore these considerations. The second study highlights the change to a more streamlined slot connector shape and reinforces the location within the slot that assists in maintaining the slot distance during flight. The final study explores the optimal number of connectors along the half-span of the wing topology with structural and aerodynamic considerations.

Chapter Five investigates the material distribution of the aft element with cruise flight conditions. This was performed with topology optimization in Abaqus CAE for the half span wing topology. The goal of the topology optimization was the strain density of the elements, while the optimization was constrained by the total volume and the displacement of several control nodes along the upper surface of the aft element. The combination of the goal and constraints ensured that the optimization highlighted the preferred material distribution for transferring the load to the slot connectors while maintaining the slot width at midspans between the slot connectors.

Chapter Six combined the previous chapters' results to produce a demonstration of the S207 SNLF airfoil's half-span wing in terms of the major components including the fore element spars and ribs, the connectors placed within the slot, and the ribs for the aft element. A FE model was generated with these previous considerations and loaded with the cruise conditions. The purpose of this chapter was to demonstrate that the previous chapters' considerations produce a viable initial half span aircraft wing structure.

The final chapter discusses the application of composites on aircraft structures with the use of adhesive bonding as a method to reduce the weight of connections. The chapter focuses on investigating the parameter space of the complex damage mechanisms observed in adhesive bonding allowing for further understanding and considerations when joining composite structures to metallic substrates.

Chapter Two

Slotted, Natural-Laminar-Flow Airfoil: A Revolutionary Technology for Fuel Efficiency

Preface

This paper is currently being prepared for publication by Kumpatla et al. [8]. The author of this dissertation contributed to this publication with conceptualization, content research, writing, and editing.

Introduction

The current need for improved aircraft fuel efficiency is unprecedented and more urgent than ever before. The data from the Federal Aviation Administration's (FAA) yearly Aerospace Forecast reports for the fiscal years of 2019 and 2020 indicates that the aerospace industry's demand will continue to increase [1]. As Figure 2-1 illustrates, the projected rate of passengers flying through the United States and total fuel usage by U.S. commercial aircraft is continuously growing, and this shows that while the COVID-19 pandemic has significantly impacted the airline industry, the FAA predicts that current passenger traffic levels will increase once vaccinations are more widespread and infection rates are under control [2]. Therefore, air travel is consistently considered to be vital, making fuel-efficient aircraft design a necessity. However, sustainable aircraft design encompasses many conflicting requirements, including accommodating the continuous increase of commercial airplane passengers, while simultaneously protecting the environment and preparing for a diminishing supply in fuel and associated rapid increase in fuel costs [9]. Therefore, such a daunting task entails the development of revolutionary new operations and aircraft technologies in order to properly ensure long-term sustainability for the aerospace industry.

Several studies have been performed to develop new concepts that can improve fuel efficiency, namely the studies by Boeing [9], the Massachusetts Institute of Technology (MIT) and Deutsches Zentrum für Luft- und Raumfahrt (DLR) [10]. The Boeing study was essentially focused on evaluating and identifying the future needs of aircraft design, and they created five different aircraft designs called the Subsonic Ultra Green Aircraft Research (SUGAR) to highlight various advanced technologies. Advanced technologies such as a strut-braced wing design, electric propulsion, high L/D ratio through the use of riblets, supercritical airfoil design, and natural laminar flow (NLF) were considered. The research conducted by MIT was similar in conceptualizing two design concepts, the D8 "double bubble" series and Hybrid Wing Body aircraft, and they were also emphasizing the need to incorporate advanced technologies to support future air transport needs. Among the list of technologies created for both aircrafts were fuselage boundary layer ingestion (BLI) and NLF on the bottom wing, both of which are suggested to improve aerodynamic performance by reducing the payload fuel energy intensity (PFEI), or the ratio of fuel energy burned divided by the payload and then

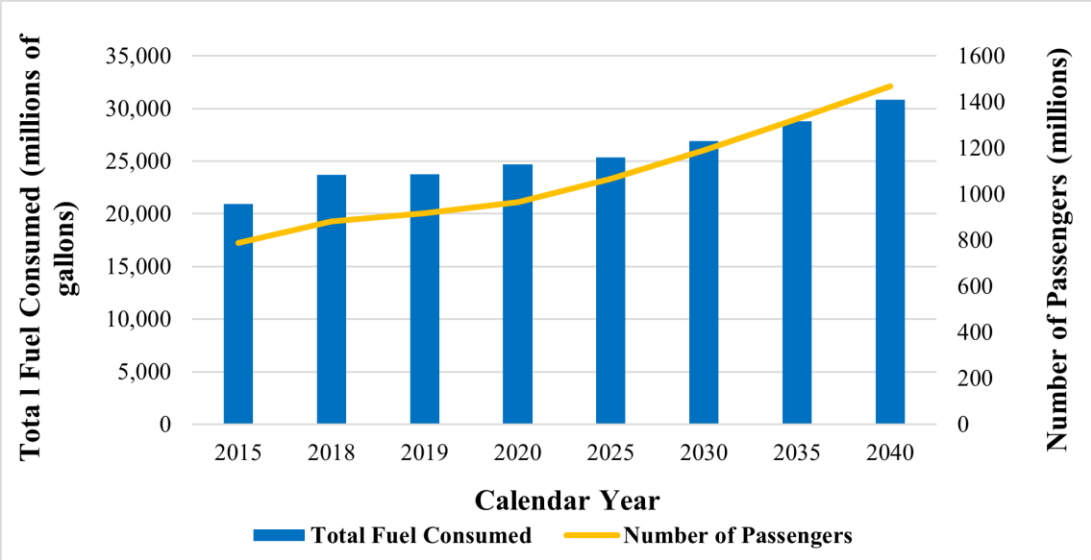


Figure 2-1: Total Domestic and International U.S. Passenger Traffic for U.S. Commercial Air Carriers; Historical and Projected Jet Fuel and Aviation Fuel Consumptionm by U.S. Civil Aircraft [1].

multiplied by the range. Lower PFEI values lead to aircrafts with more efficient fuel consumption that will drastically reduce the environmental impact of future aircrafts, fulfilling a major criterion within MIT's design goals. Finally, researchers at DLR considered the possible benefits from extensive laminar boundary layers on the wing surface by greatly reducing the additional drag that accompanies laminar-turbulent transition. This insight resulted in the establishment of Project Laminar Aircraft Research, or LamAiR, with the central goal to design a forward swept wing for short and medium range transport aircraft that would produce a greater extent of natural laminar flow without substantially increasing the wave drag. A recurring theme within these studies is the appearance of natural laminar flow while discussing advanced technologies that contribute to reduced fuel burn and enhanced aerodynamic performance. While NLF has been studied and utilized for aircraft design previously, many researchers believe that it can be further implemented to drastically improve future aircraft designs further.

One way of utilizing NLF in the aircraft design is through the airfoil design. NLF airfoils have been designed for different classes of aircraft to produce high lift coefficients and reduce wing profile drag coefficients [11]. NLF airfoils produce laminar flow over a reasonable extent of the airfoil chord, therefore enabling these reduced drag coefficients. While NLF airfoils alone have been very effective in contributing to a reduction of fuel consumption, another category of airfoils has also shown similar desirable behaviors. Slotted airfoils, which have been researched and developed more recently, showed increased maximum lift coefficient along with reduced wetted area and overall drag [12-14]. In an attempt to develop a more efficient airfoil, the NLF and slotted airfoil concepts were combined, which gave rise to the slotted, natural-laminar-flow (SNLF) airfoil [15]. As a result, SNLF airfoils can achieve favorable pressure gradients over a large portion of the chord while still maintaining high maximum lift coefficient and reduced overall drag.

Challenges of Achieving Laminar Flow & SNLF Airfoils

Maintaining laminar flow is extremely challenging because the airfoil must simultaneously fulfill multiple flight conditions, such as high Mach numbers, high Reynolds numbers, and increased section lift conditions. If the Reynolds number is very high, then the favorable pressure gradient must also extend along the entire length of the airfoil to stabilize the flow and maintain the laminar boundary layer [16]. Additionally, accounting for the various range of instabilities is crucial to prevent the boundary layer from transitioning from laminar to turbulent. For wings with relatively large sweep angles, the predominant instability is crossflow; however lower swept wings have primarily Görtler instabilities [17]. This presents a conflict as reducing the wing sweep could lower crossflow instabilities (CFI), but wing sweep is also crucial for increasing the critical Mach number, which is desirable for better aircraft efficiency [18]. Therefore, due to the various issues presented by the transition from laminar flow to turbulence flow, researchers are investigating approaches to reduce this wing profile drag to allow for more laminar flow and higher lift coefficients.

While such a solution may appear to be straightforward, examining the technical details reveals certain issues. For example, one approach to achieve reduced wing profile drag is to utilize a mechanical high-lift system to increase the maximum lift coefficient; however, such a complex structure tends to be heavy, expensive, and could strain the system to the point of potential failure [15]. An ideal solution would not need extreme additions of materials and would be easily integrated into the existing framework of the aircraft.

Another attempt to decrease wing profile drag is via passive laminar flow by designing the shape of a single-element airfoil to provide an increased extent of natural laminar flow (NLF) on the surface. Utilizing this airfoil allows for a higher achievable maximum lift coefficient while also decreasing the profile drag coefficient. While many such airfoils have been designed and developed, single-element NLF airfoils have certain design limits that cannot be overcome through mere airfoil shaping. For instance, the extent of laminar flow along the aft and leading-edge sweep of the airfoil is limited to around 70-percent chord. Additionally, once the adverse pressure gradient reaches a certain point, trailing edge separation occurs [15]. The separation decreases the maximum lift coefficient, further reducing the L/D ratio of the aircraft.

One example of a single-element NLF airfoil is the NASA Common Research Model (CRM), specifically the CRM.65 model. It has been heavily researched and developed, and while the airfoil has been able to reach a higher level of laminar flow than standard airfoils, analyses show that there is also a 25 percent increase in total profile drag due to an early transition to turbulent flow on the lower surface [19, 20]. This indicates that the benefits that NLF provides to the CRM.65 are counteracted by the increased drag, and this design cannot sustain large extents of laminar flow while also preventing early transition.

In contrast, the slotted design of the SNLF airfoil overcomes the technical barriers that make laminar flow difficult to maintain. The SNLF airfoil provides an elegant solution while still allowing for a remarkable amount of increased fuel efficiency and airplane performance. While there has traditionally been a limited amount of naturally produced laminar flow for any aircraft wing, the two-element SNLF airfoil redefines those limits past any that is achievable by a single-element airfoil, solely through its slotted design [21]. This slot configuration allows for laminar flow across multiple parts of the airfoil. By including a slot that is always open between the fore and aft elements, the favorable pressure gradient can extend farther aft and along both surfaces of the fore elements. This allows the fore element to be entirely laminar, while the aft element also achieves 60 percent on the upper surface and 100 percent on the lower, which results in the entire SNLF airfoil reaching around 90 percent laminar flow on its surface [6, 7]. Thus, the SNLF airfoil concept brings about lower wing profile drag coefficients and higher maximum lift coefficients through revolutionary wing design while simultaneously preserving the conventional airfoil shape.

The SNLF Airfoil Development Timeline

Early research in the development of laminar flow airfoils resulted through some of the research programs carried out by the National Advisory Committee for Aeronautics (NACA) in the 1930s. Drag coefficients as low as 0.0078 (C_{Dmin}) arising from the presence of laminar boundary layers over a reasonable fraction of the chord length had been observed for the NACA 23012 airfoil during wind tunnel tests with moderately low levels of turbulence for a low Reynolds number range of 1×10^6 to 8×10^6 [22]. The corresponding value of C_{Lmax}/C_{D0min} was found to be 208. Jacobs [23] advanced the airfoil testing by modifying the existing NACA smoke wind tunnel to achieve very low levels of turbulence. This was an important milestone as it led to the development of low-speed airfoils (Reynolds number up to 6×10^6) with laminar flow boundary layers extending up to around 70% of the chord length and drag coefficients as low as 0.0022 (C_{Dmin}) and C_{Lmax}/C_{D0min} values as high as 290. These airfoils were designed by locating the maximum thickness station of the airfoils further aft along the chord line. This ensured that the minimum pressure point was moved toward the back of the airfoil leading to the extension of the laminar boundary layer along a larger portion of the airfoil. Figure 2-2.b shows the section and the C_p plot for the NACA 27-215 airfoil which was one of the laminar flow airfoils developed by Jacobs [23, 24]. Also, the section and the C_p plot for the NACA 23012 airfoil is illustrated in Figure 2-2.a for comparison purposes.

Later in the 1940s, NACA developed and verified a variety of high-speed airfoils such as the NACA 6-series airfoils, which showed lower drag characteristics and higher critical Mach numbers than its predecessors [25]. The NACA 6 series airfoils were designed by utilizing improved theoretical methods such as Theodorsen's method [26] which were more accurate as compared to the methods utilized for designing NACA 2 to 5 series sections [23]. Figure 2-3.a shows the section of one of the 6-series airfoils, NACA 65_3-018 along with the corresponding C_p plot. Figure 2-3.b shows a comparison of the minimum section drag coefficient (C_{Dmin}) for different NACA airfoils including few airfoils from the 6-series for a range of Reynolds number. At high Reynolds numbers between 1×10^7 and 3×10^7, it can be seen from Figure 2-3.b that NACA $65_{(421)}$-420 and NACA 66(2x15)-116 exhibit lower values of C_{Dmin} as compared to NACA 23021 and NACA 0012.

In the 1950s NACA shifted its focus to the development of supersonic aircraft. In 1958, space applications were included along with the existing focus on aeronautics research and NACA was transformed into the National Aeronautics and Space Administration (NASA). Airfoil research was once again a topic of interest at NASA with the development of a supercritical, turbulent-flow airfoil by Richard Whitcomb in 1965 [12]. These supercritical airfoils were developed to increase the supercritical Mach number beyond which a rapid increase in drag, buffeting and loss of stability are observed when conventional airfoils such as the NACA 6-series. As shown in the top half of Figure 2-4, when a conventional airfoil is subjected to supercritical Mach numbers, a shock wave is seen at the mid-chord location. A subsonic pressure recovery is observed upon moving further toward the trailing edge. As shown by the C_p plot in the upper half of Figure 2-4, there is a drastic increase in the pressure at the trailing edge leading to a

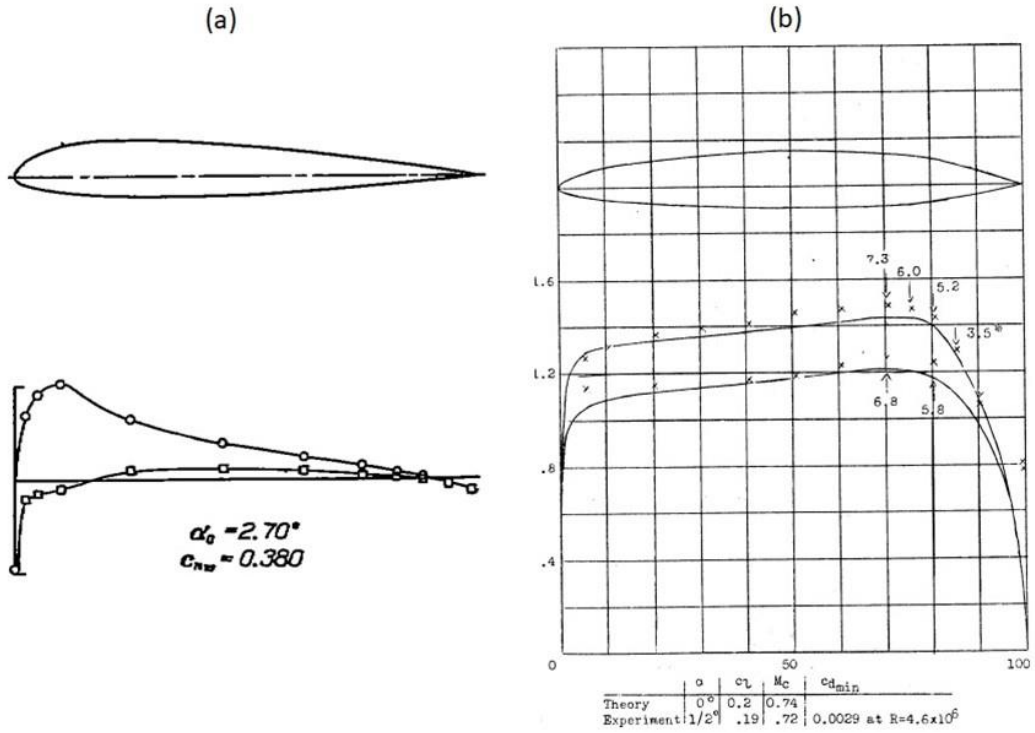


Figure 2-2: Comparison of the sections and Cp plots for (a) NACA 23012 [23] and (b) NACA 27-215 [24] airfoils.

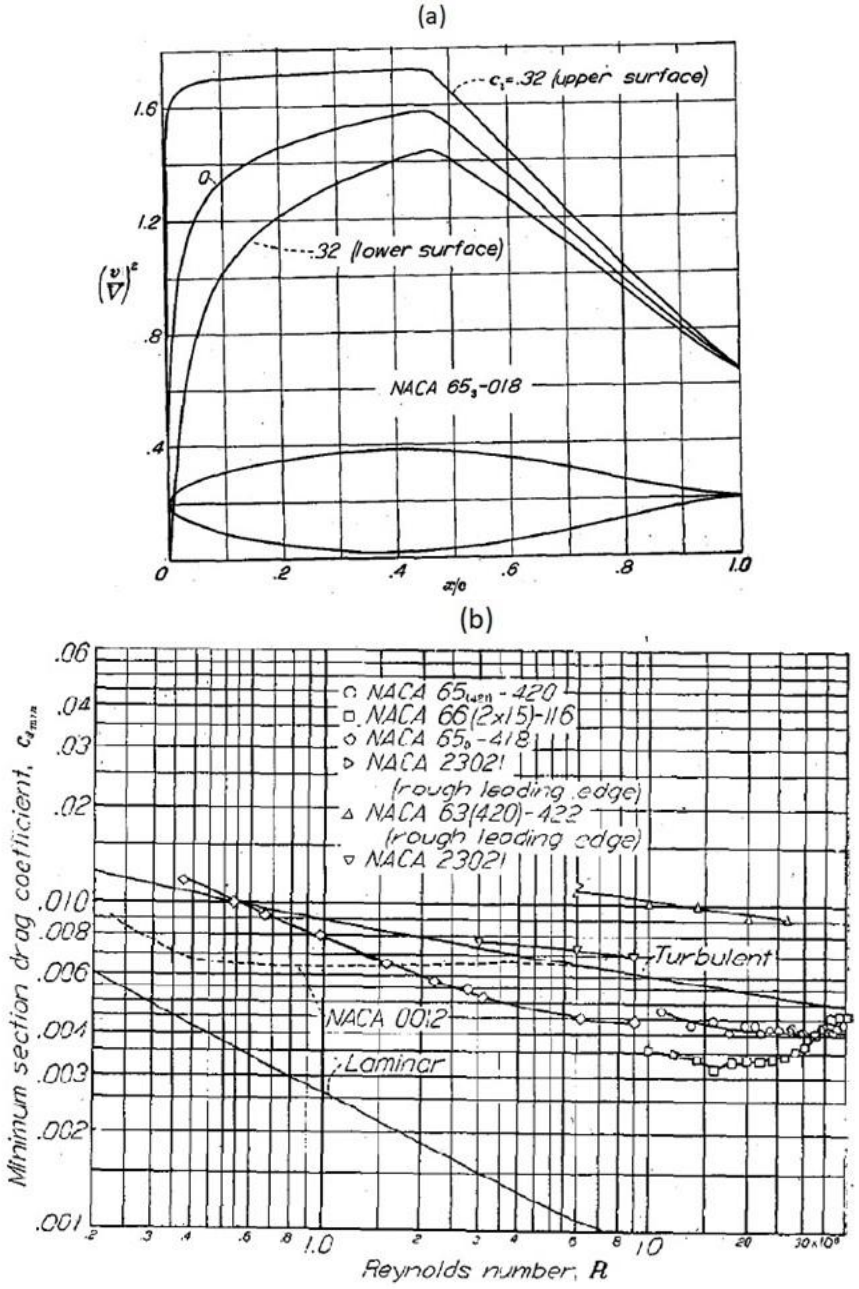


Figure 2-3: (a) Section of a 6 series airfoil, NACA 653-018 with a plot of (v/V)2 which is analogous to Cp and (b) Comparison of the minimum section drag coefficient across different NACA airfoils for a wide range of Reynolds number, together with laminar and turbulent flow [25].

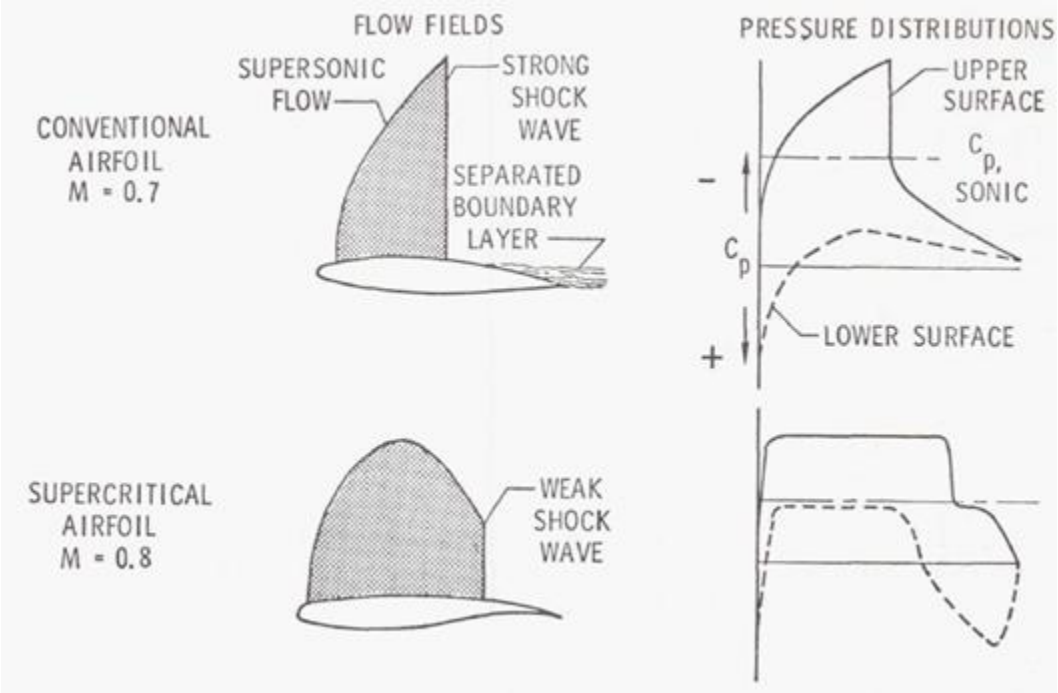


Figure 2-4: Comparison of (a) flow characteristics and (b) Cp plots of conventional (example NACA 6-series) and NASA supercritical airfoils at supercritical Mach numbers [27].

severe separation of the boundary layer. This separation is associated with the above-mentioned rapid increase in drag, buffeting, and loss of stability. The supercritical airfoils were shaped to have a reduced curvature in the mid-chord region on the upper surface combined with an increased camber near the trailing edge as seen in the lower half of Figure 2-4 [27]. The reduced curvature of the supercritical airfoil ensures that the flow does not accelerate before it meets the shock wave. This reduces the strength of the shock wave. Also, the pressure distribution now has a plateau as can be seen in the lower half of Figure 2-4, which minimizes the chance of boundary layer separation near the trailing edge. Therefore, with the use of supercritical airfoils the supercritical Mach number could be increased by around 0.1 as shown in Figure 2-4. Besides, at subcritical Mach numbers or low speeds, thicker supercritical airfoils did not show a significant decrease in the drag coefficient as had been previously reported for the thick versions of prior conventional airfoils [28]. The use of an airfoil section such as a thicker supercritical airfoil allows for higher lift coefficients while reducing the structural weight [28].

Motivated by thick supercritical airfoils, turbulent flow airfoils were designed by NASA for low-speed applications [29, 30]. These low-speed airfoils achieved higher maximum lift coefficients as compared to their predecessors while having a higher L/D at the climb condition together with a better defined and controlled stall behavior [29, 30]. However, the low-speed airfoils showed no improvements in the cruise drag coefficients over their predecessors and around 1980, NASA decided to create NLF airfoils that combined low drag from the NACA 6-series airfoils with the high lift from the low-speed airfoils [31]. One of the NLF airfoils designed for general aviation was the NLF(1)-215F airfoil [31]. This aircraft was designed to achieve two main objectives. Firstly, the airfoil should generate a maximum lift at a Reynolds number of 3×10^6 comparable to that produced by the low-speed, turbulent flow airfoils. Secondly, the airfoil should exhibit low profile-drag coefficients at a Reynolds number of 9×10^6 corresponding to cruise condition with $C_L = 0.2$ and also for climb condition with $C_L = 0.5$ to 1.0. Normally, it can be very difficult to achieve these conditions simultaneously, as a low profile-drag coefficient causes the pressure gradient on the aft's upper surface to increase, consequently decreasing the maximum lift coefficient. However, because the NLF(1)-0215F is a flapped NLF airfoil, the airfoil is permitted to have a relatively high amount of camber, which is crucial to maintain a high maximum lift coefficient, while still allowing it to maintain a low pitching moment coefficient ($c_{m,0}$) [31]. Figure 2-5 shows the airfoil shape and inviscid, incompressible velocity distributions for the NLF(1)-0215F airfoil at different flap deflections and different values of C_L. Upon theoretical and experimental analysis, the NLF(1)-0215F successfully met both of the primary objectives and was able to capture a high extent of laminar flow.

Some of the earlier laminar flow airfoils including the NLF(1)-0215 are aft loaded which leads to large nose-down pitching moments and can result in trim-drag penalties [32]. Also, using these airfoils in the region of the wing where control surfaces are installed can cause large control forces and the control surfaces can have a tendency to 'float' [32]. Therefore, another NLF airfoil, entitled the NLF(1)-0115, was designed for general aviation applications [60]. Several of the favorable features were adopted from previously successful airfoil designs to create the NLF(1)-0115 airfoil. Firstly, the lift

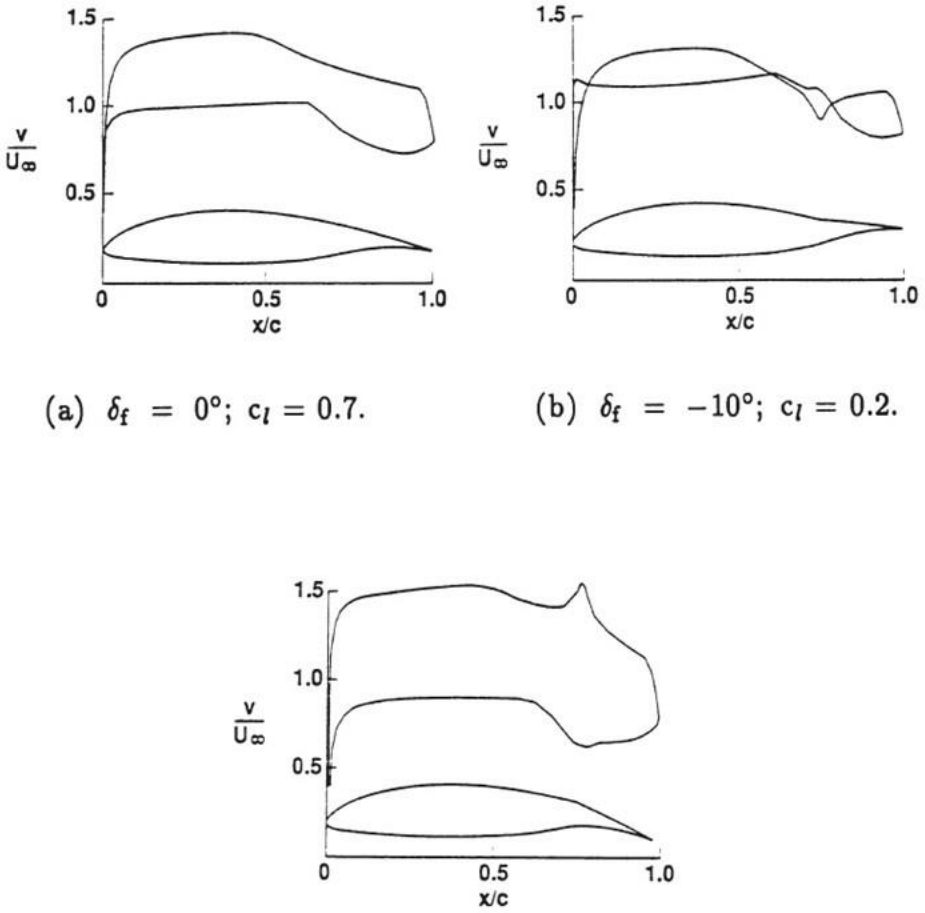


Figure 2-5: NLF(1)-0215F airfoil shape and inviscid, incompressible velocity distributions (analogous to Cp plots) [31].

range of the turbulent flow NACA 23015 airfoil which gets impacted only slightly due to leading-edge contamination, was incorporated. Furthermore, an attempt was made to replicate the low drag characteristics of the NACA 632-215 airfoil. However, there was an increase in the nose-down pitching moment as a tradeoff that had to be made for the low drag characteristics. Finally, the desired performance was achieved through the design of the NLF(1)-0115 airfoil which was developed through careful consideration of the boundary-layer development and paying great attention to the movement of the transition location with lift coefficient [32].

While NLF airfoils offered the advantage of low drag characteristics, it was still desirable to augment the low drag capabilities with higher maximum lift coefficients. Slotted airfoils were known to deliver higher maximum lifts as compared to unslotted airfoils. Slotted airfoils have multiple elements separated by slots [12-14]. Examples of slotted airfoil are the original slotted, supercritical airfoils [12] and the MDA 3-element high lift [14] as shown in Figure 2-6. The presence of a slot ensures that the pressure at the trailing edge of the element forward of the slot can be lower than the free stream and pressure recovery can be carried out off the surface. This effect is also termed as a "dump velocity" [14] that exists as the flow accelerates just after exiting the trailing edge of the element forward of the slot. Also, the slot prevents the formation of a strong suction peak on the element aft of the slot. Further, generally a fresh boundary layer is allowed to form at the element aft of the slot and since we do not have a strong suction peak, the airfoil can operate at much higher angles of attack before a stall occurs. The slotted, natural laminar flow (SNLF) airfoil technology was developed by Somers combining the low drag characteristics of NLF airfoils and the higher maximum lift coefficients offered by a slotted design [6]. Figure 2-7 shows the shape of a typical SNLF airfoil along with the corresponding pressure distribution or C_p plot. The airfoil has two elements, namely- fore and aft elements. Because the design of the forward or the fore element does not need to meet the requirement of a pressure recovery at the trailing edge of the fore element, the minimum pressure can now be located near the trailing edge. This means that the entire fore element can have a favorable pressure gradient. The aft element produces circulation and therefore aids in supporting the 'dumping velocity' at the exit of the fore element. A fresh boundary layer develops at the aft element and again, favorable pressure gradients can be maintained almost throughout the aft element. In conclusion, laminar flow can be developed over entire of the fore element, the entire lower surface of the aft element and majority of the upper surface of the aft element.

Four models of the SNLF airfoil have been developed, namely- S103 for general aviation, S204 for business jet, S414 for rotorcraft and S207 for transport aircrafts [15, 19, 33, 34]. In addition, a fifth model designated as the X207LS was created to support the development of the S207 airfoil [35]. Figure 2-8 depicts the shapes of these five models [36]. Figure 2-9 shows the timeline of the major events related to the development and testing of these airfoils. The following text describes the development and testing of each of the five models of the SNLF airfoil in detail. Table 2-1 presents a summary of the intended application and design specifications of different SNLF airfoils. Note that M_{dd} is the drag-divergence Mach number and t/c is the ratio of the airfoil thickness to the chord length.

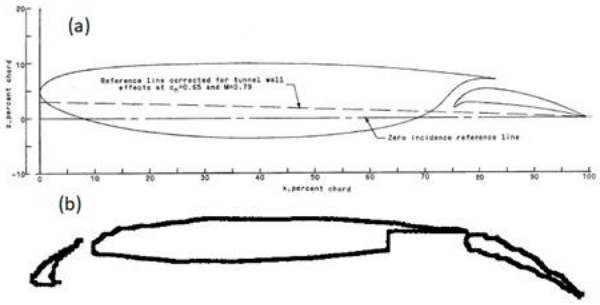


Figure 2-6: (a) Original slotted, supercritical airfoils [12] (b) MDA 3-element high lift airfoil [14].

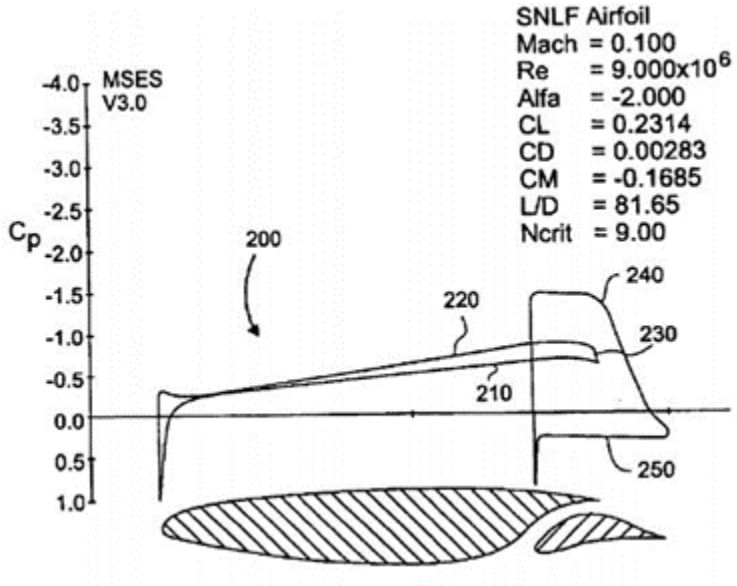


Figure 2-7: Depiction of pressure distribution for an SNLF airfoil (from patent) [6].

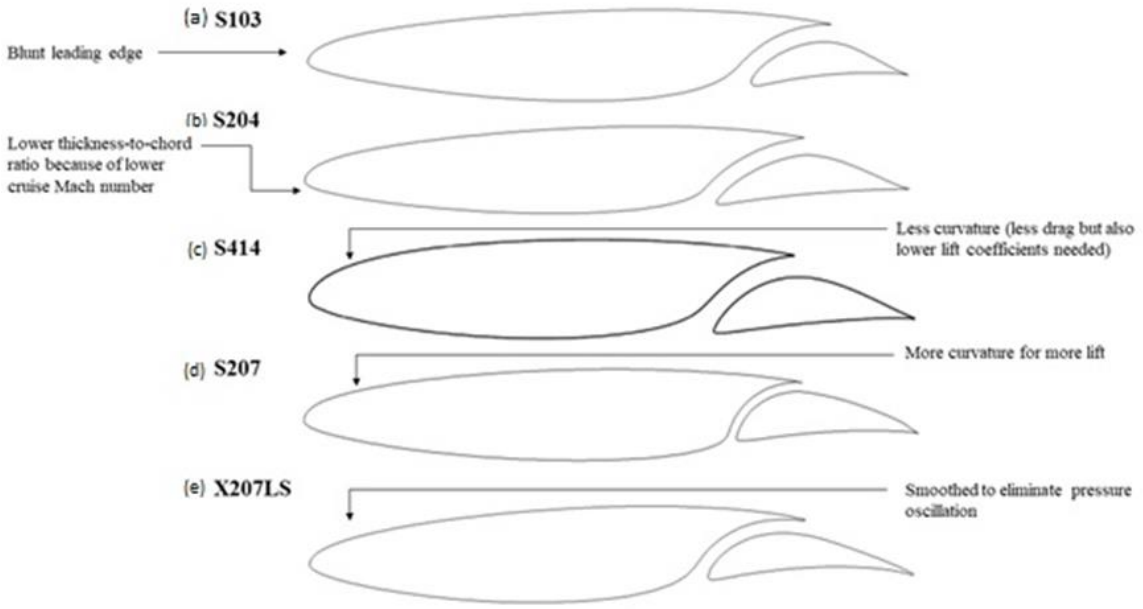


Figure 2-8: Compilation of the SNLF airfoil shapes with design annotations [36].

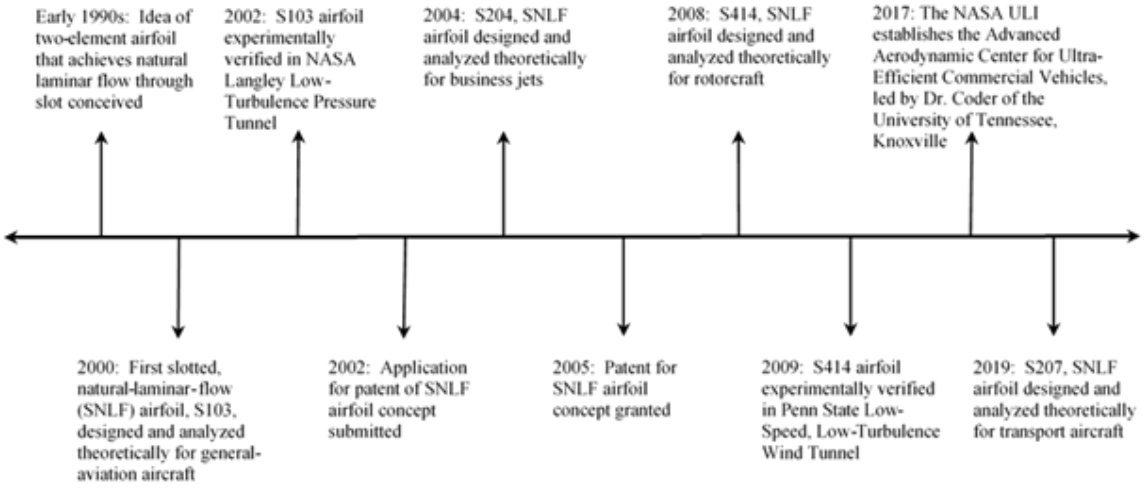


Figure 2-9: Timeline of the development and testing of various specialized SNLF airfoils [36].

Table 2-1: Various SNLF airfoil models and the corresponding design specifications [36].

Airfoil	Designated aircraft	Parameter	Value	Reynolds number	Mach Number
S103	*General Aviation*	$C_{l,max}$	≥ 1.72	3×10^6	M = 0 (incompressible, low speed application)
		$C_{l,ll}$	0.20	9×10^6	
		$C_{l,ul}$	1.00	6×10^6	
		$C_{m,0}$	≥ -0.20	9×10^6	
		M_{dd}	Unconstrained	-	
		t/c	0.15	-	
S204	*Business Jet*	$C_{l,max}$	≥ 1.55	3×10^6	0.10
		$C_{l,ll}$	0.20	12×10^6	0.65
		$C_{l,ul}$	0.40	12×10^6	0.30
		$C_{m,0}$	Unconstrained	-	-
		M_{dd} at C_l=0.25	≥ 0.70	12×10^6	-
		t/c	0.15	-	-
S414	*Rotorcraft*	$C_{l,max}$	≥ 1.25	0.97×10^6	0.30
			≥ 1.20	1.29×10^6	0.40
		$C_{l,ll}$	0.10	2.26×10^6	0.70
		$C_{l,ul}$	0.65	1.45×10^6	0.45
		$C_{m,0}$	-	-	-
		M_{dd}	-	-	-
		t/c	0.14		
S207	*Transport Aircraft*	$C_{l,max}$	≥ 2.30	16×10^6	0.225
		$C_{l,ll}$	0.39	13.2×10^6	≥ 0.66 (0.70 actual)
		$C_{l,ul}$	0.65	13.2×10^6	≥ 0.66 (0.70 actual)
		$C_{m,0}$	Unconstrained	-	-
		M_{dd}	Unconstrained	-	-
		t/c			

S103, SNLF Airfoil

The first SNLF airfoil, S103 was designed in 2000 [15]. Created with general-aviation applications in mind, specifically low-speed aircraft, the S103 had to meet the primary objectives of high maximum lift and low profile drag coefficients while also meeting the pitching moment and airfoil thickness constraints [15]. The goals were to reach a maximum lift coefficient of at least 1.72 at a Reynolds number of 3×10^6, as well as to achieve low-profile drag coefficients from the range of a cruise lift coefficient of 0.20 at a Reynolds number of 9×10^6 to a climb lift coefficient of 1.00 at a Reynolds number of 6×10^6 [15]. Figure 2-8.a shows the shape of this airfoil. The airfoil contains fore and aft elements. The Eppler Airfoil Design and Analysis Code which is a single-element code was used to generate initial shape of fore and aft elements [37, 38]. Design optimization of fore and aft elements was performed using a multi-element, MSES code to arrive at the final design [39]. Figure 2-10 shows the pressure distribution for the cruise (design) condition with C_l of 0.2 and Re of 9×10^6. As seen from Figure 2-10, a minimum pressure occurs near the trailing edge at both upper and lower surfaces of the fore element. This is indicative of a favorable pressure gradient over the entire fore element. Pressure recovery takes place over the aft element. The wake of the fore element does not impinge on the aft element and therefore, the aft element can also exhibit laminar flow over a large extent.

Later in 2002, wind-tunnel tests were conducted in NASA's Langley low-turbulence pressure tunnel to evaluate the performance of the S103 airfoil. Figure 2-11.a shows a comparison of the pressure distribution between theoretical and experimental results for $Re = 3 \times 10^6$, $M = 0.10$, and $\alpha = -1.07°$ with transition free i.e. transition was not fixed to the leading edge of the fore element. The theoretical results show good agreement with the experiments, especially for the aft element. Figure 2-11.b shows the section characteristics at $Re = 3 \times 10^6$ and $M = 0.10$. A max lift coefficient of 2.00 is achieved, which is greater than the design target of 1.72. The S103 exhibits a rapid stall which is indicated by the trend of C_l vs. α as shown in the Figure 2-11.b. For $\alpha \geq 17°$, the lift decreases rapidly. Thus, the S103 does not meet the airfoil's goal of having minimal and docile stall characteristics [15]. Overall, the airfoil exhibits favorable pressure distributions and section characteristics that fulfill the design objectives except for the rapid stall. The S103 has a 12 percent higher maximum lift coefficient when compared to the NLF(1)-0215F with a flap deflection of $10°$ and a 7 percent lower drag coefficient when compared to the NLF(1)-0215F with a flap deflection of $-10°$ [15]. It should be noted that the MSES code doesn't account for Gortler instabilities [39]. These instabilities are expected to cause transition in the concave region of the lower surface of the fore element [15].

S204, SNLF Airfoil

The succeeding SNLF design is the S204 airfoil, as shown in Figure 2-8.b. It was conceptualized and analyzed theoretically for business-jet applications in 2004. The S204 had the same design objectives as the S103 — high maximum lift and low profile drag — however, the S204 design also aimed for relative insensitivity to roughness [33]. Specifically, the objectives were to reach a maximum lift coefficient of at least 1.55 at a

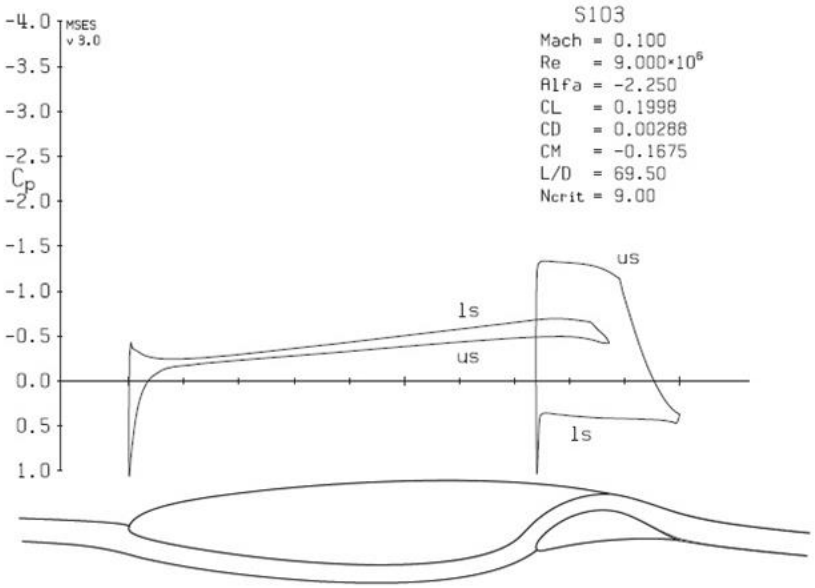


Figure 2-10: Pressure distribution over the SNLF, S103 airfoil at the design point (cruise). Note that 'ls' and 'us' are abbreviations for the lower and upper surfaces, respectively.

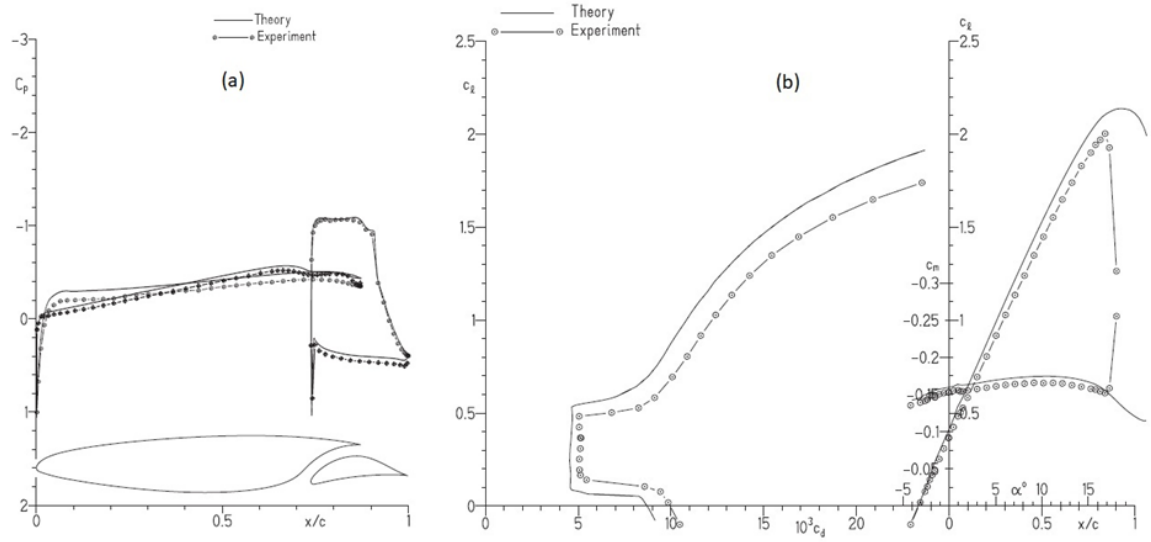


Figure 2-11: Results for SNLF, S103 airfoil (a) Comparison of theoretical and experimental pressure distributions for Re = 3 x 10^6, M = 0.10 and α = -1.07° with transition free [15]. Open symbols represent data for upper surface; crossed symbols, data for lower surface. (b) Comparison of theoretical and experimental section characteristics (c_l vs. c_d and c_l , c_m vs. α) at Re = 3 x 10^6 and M = 0.10 with transition free [15].

Mach number of 0.10 and a Reynolds number of 3×10^6 (which is the tip chord at a minimum velocity), and to obtain low profile-drag coefficients from a lift coefficient of 0.20 at a Mach number of 0.65 and a Reynolds number of 12×10^6 (the root chord at cruise condition) to a lift coefficient of 0.40 at a Mach number of 0.30 and a Reynolds number of 12×10^6 (the root chord at climb condition). Further, the design of S204 should prevent the maximum lift coefficient from decreasing with fixed transition near the leading edge. In addition, the design should also display docile stall characteristics. Even though there was a constraint for the airfoil thickness to equal 15-percent chord, the final design was 14 percent to account for the higher cruise Mach number of business jets with respect to an aircraft used for general aviation [33].

While the S204 has not undergone experimental testing to date, it was theoretically designed and verified. The design analysis and computational analysis was conducted using the single-element, Eppler Airfoil Design and Analysis Code as well as the multi-element, MSES code. Figure 2-12 shows the theoretical pressure distribution at the cruise condition. Figure 2-13 shows the theory-based transition locations and section characteristics predicted by the theory for $M = 0.1$ and $Re = 3 \times 10^6$. Transition lines showing the location of the transition point on the fore and aft elements have been marked on Figure 2-13 for the transition free case. The theoretical results show that the laminar flow extends to the trailing edge on both surfaces of the fore element, 60 percent chord on the upper surface of the aft, and to the trailing edge on the lower surface of the aft [33]. Based on Figure 2-13, theory predicts a maximum lift coefficient of 2.13 which is greater than 1.55, the design objective. Additionally, when considering the effect of roughness, there was only a decrease of approximately 1 percent in maximum lift coefficient from the airfoil that was transition-free, indicating that the design objective pertaining to roughness insensitivity is fulfilled [33]. The S204, SNLF airfoil design successfully met its main design objectives through theoretical analysis.

S414, SNLF Airfoil

As shown in Figure 2-8.c, the S414, SNLF airfoil was designed for rotorcraft applications [21, 34]. The overall goal was to maximize rotor L/D ratio by increasing the section maximum lift coefficient for the retreating blade while reducing the cruise section profile-drag coefficient. A higher lift coefficient delays the stall-flutter on the retreating blade while a lower section profile-drag coefficient leads to a decreasing drag on the advancing blade [34]. Specifically, the first primary design objective was to achieve a maximum lift coefficient of 1.25 at a Mach number of 0.3 and a Reynolds number of 0.97×10^6, and a maximum lift coefficient of 1.20 at a Mach number of 0.40 and a Reynolds number of 1.29×10^6 [21, 34]. Additionally, fixing the transition to the leading edge of either or both elements should not reduce the maximum lift coefficient significantly. Further, the airfoil should show docile stall characteristics. Another design objective is to obtain low profile-drag coefficients from a lift coefficient of 0.10 at a Mach number of 0.70 and a Reynolds number of 2.26×10^6 to a lift coefficient of 0.65 at a Mach number of 0.45 and a Reynolds number of 1.45×10^6 [21, 34]. Besides, the thickness should equal approximately 14 percent chord. The Eppler Airfoil Design and Analysis Code and the MSES code were utilized to design the S414 airfoil. As seen from Figure 2-14, the

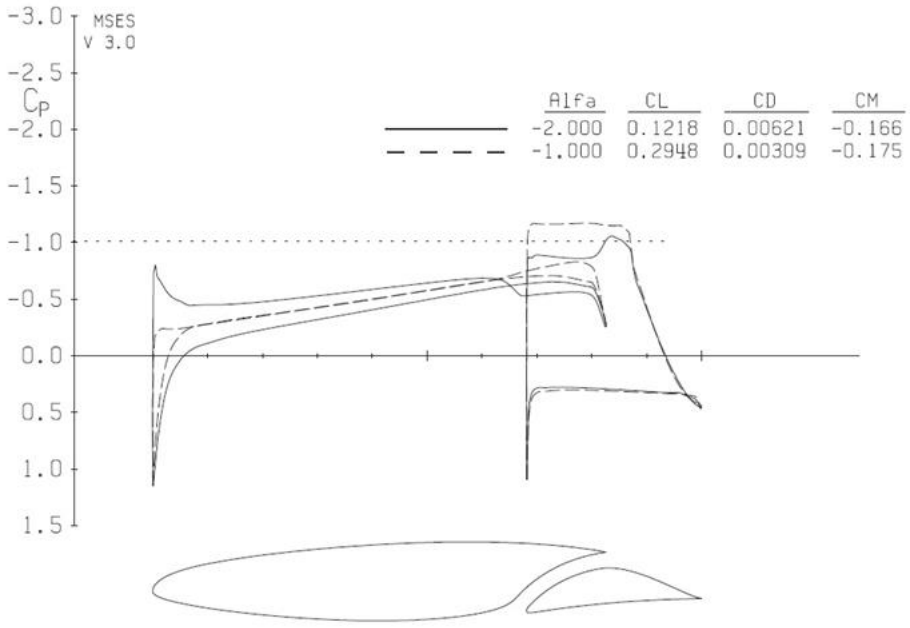


Figure 2-12: Theoretical pressure distribution for the SNLF, S204 airfoil at M = 0.65 and Re = 12 x 10^6 for α= -1° and -2° transition free.

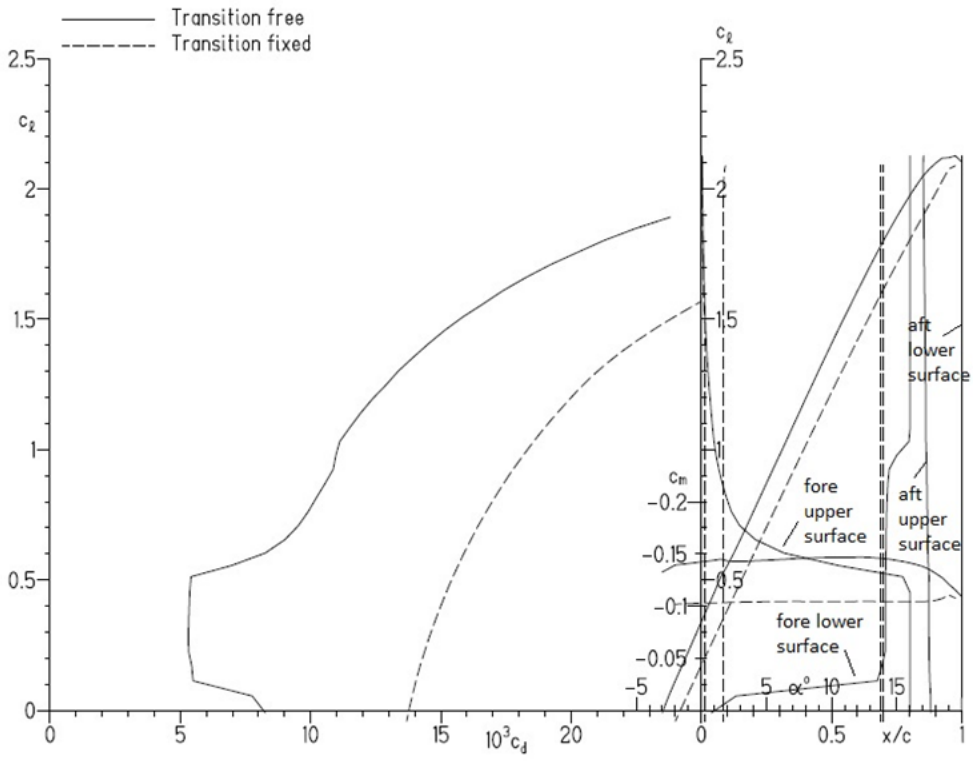


Figure 2-13: Theoretical transition locations and section characteristics for the SNLF, S204 airfoil at M = 0.10 and Re = 3 x 10^6 [34].

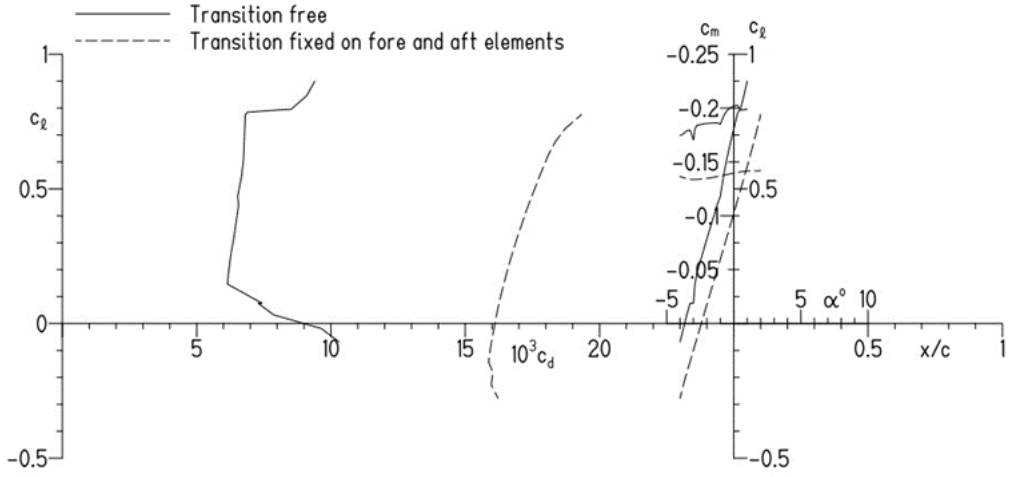


Figure 2-14: Section characteristics for the SNLF, S204 airfoil at M=0.70 and Re= Re = 2.26 x 10^6 [34].

lower limit of the low-drag, lift-coefficient range was higher than 0.1. However, the remaining results yielded by the theoretical analysis align with the specified objectives and constraints [34].

In 2009, the S414, SNLF airfoil was successfully tested and experimentally verified through a series of wind-tunnel tests in the Pennsylvania State University Low-Speed, Low-Turbulence Wind Tunnel (LSLTT) [21]. Furthermore, CFD analysis of the S414 airfoil was performed using OVERFLOW and comparisons with experiments and MSES-based theoretical predictions were performed [21]. Figure 2-15.a illustrates a comparison of pressure distributions from the experiments, MSES and OVERFLOW for $Re = 1.5 \times 10^6$ [21]. The predictions from MSES and OVERFLOW are in very close agreement for the first element but show small differences at the slot entrance. The theoretical pressures on the fore element are lower than the experimental values, possibly due to the theoretical pressures that are recovered at the trailing edge of the fore element being lower than the experimental value. Also, MSES and OVERFLOW results are in close agreement on the aft element. However, there are differences between the theoretical and experimental pressure distributions on the aft element. This could be due to the fact that the MSES and OVERFLOW were run to match the combined lift coefficients of the fore and aft elements with that from the experiment instead of matching the lift coefficients of either elements [21]. Nevertheless, the overall consistency between MSES and OVERFLOW demonstrated validation for the computational fluid dynamics approach for analyzing the SNLF airfoil [21].

S207, SNLF Airfoil

Another variation of the SNLF airfoil is the S207 which was designed to address the needs of transport aircrafts [5, 19]. The shape of this airfoil is shown in Figure 2-8.d. As with the previous designs, the core goals revolve around the reduction of wing profile drag and achievement of high maximum lift that is insensitive to roughness. The design specifications were initially derived from the Boeing SUGAR study and further refined as the design progressed [5, 19]. The primary objectives were to achieve a maximum lift coefficient of 2.30 at a Mach number of 0.225 and a Reynolds number of 16.0×10^6, as well as to obtain low profile-drag coefficients over the range of lift coefficients from 0.39 to 0.65 at a Mach number of at least 0.66 and a Reynolds number of 13.2×10^6 [19]. As with the S103, S204, and S414, the S207 airfoil design was also derived using the Eppler Airfoil Design and Analysis Code for the MSES code [5, 19].

The pressure distributions over the S207 airfoil predicted by MSES at $M = 0.71$ and $Re = 13.2 \times 10^6$ for lift coefficients of 0.39, 0.65 and 0.78 are shown in Figure 2-16.a. The lift coefficients of 0.39 and 0.78 represent values fairly close to the lower and upper limits of the low drag range, respectively for $M = 0.71$. Looking at the pressure distributions over the fore element, as the lift coefficient increases, the pressure gradient on the upper surface becomes less favorable and the pressure gradient on the lower surface becomes more favorable [19]. There is almost no effect of increasing the lift coefficient on the pressure distribution over the aft element. This is consistent with the observations for previous SNLF airfoils. As for the boundary-layer transition, when within the low-drag range, the airfoil achieves complete laminar flow on both surfaces of

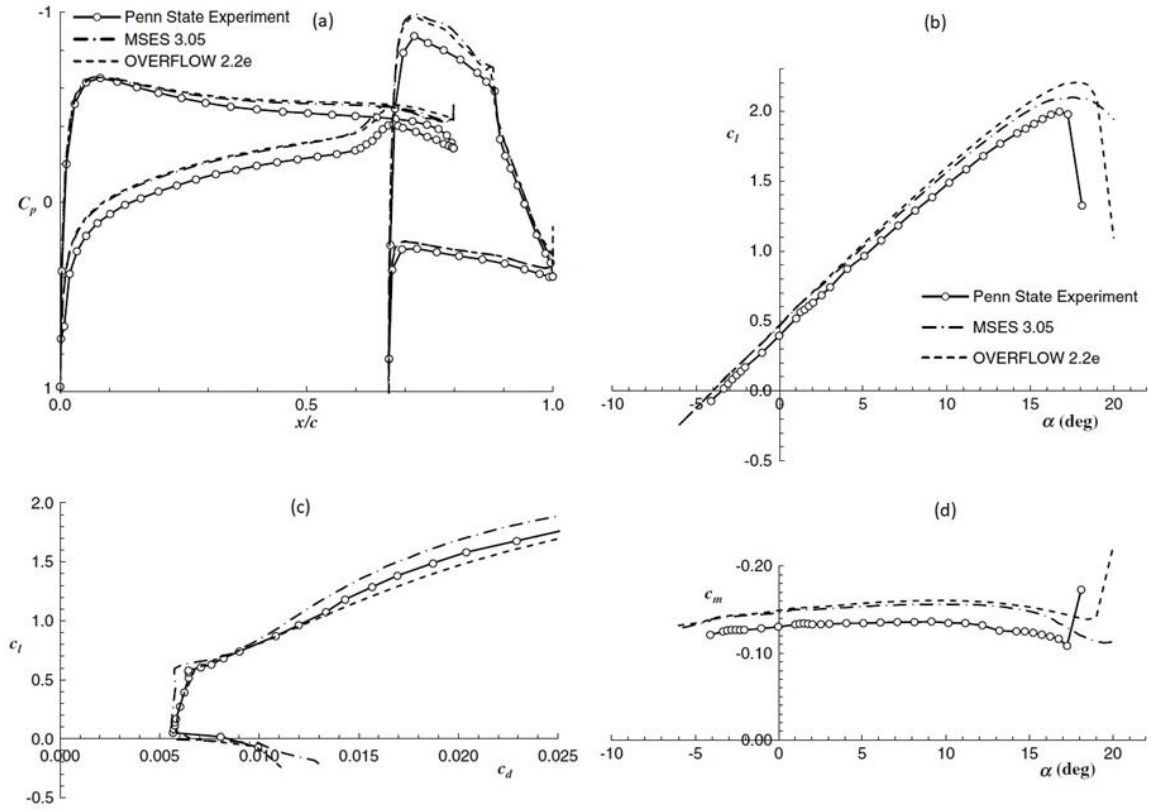


Figure 2-15: Results for SNLF, S414 airfoil: (a) Comparison of theoretical and experimental pressure distributions at $c_l = 0.518$ and $Re = 1.5 \times 10^6$ [Coder-15] (b) Comparison of predicted and measured section characteristics for $Re = 1.5 \times 10^6$ [21].

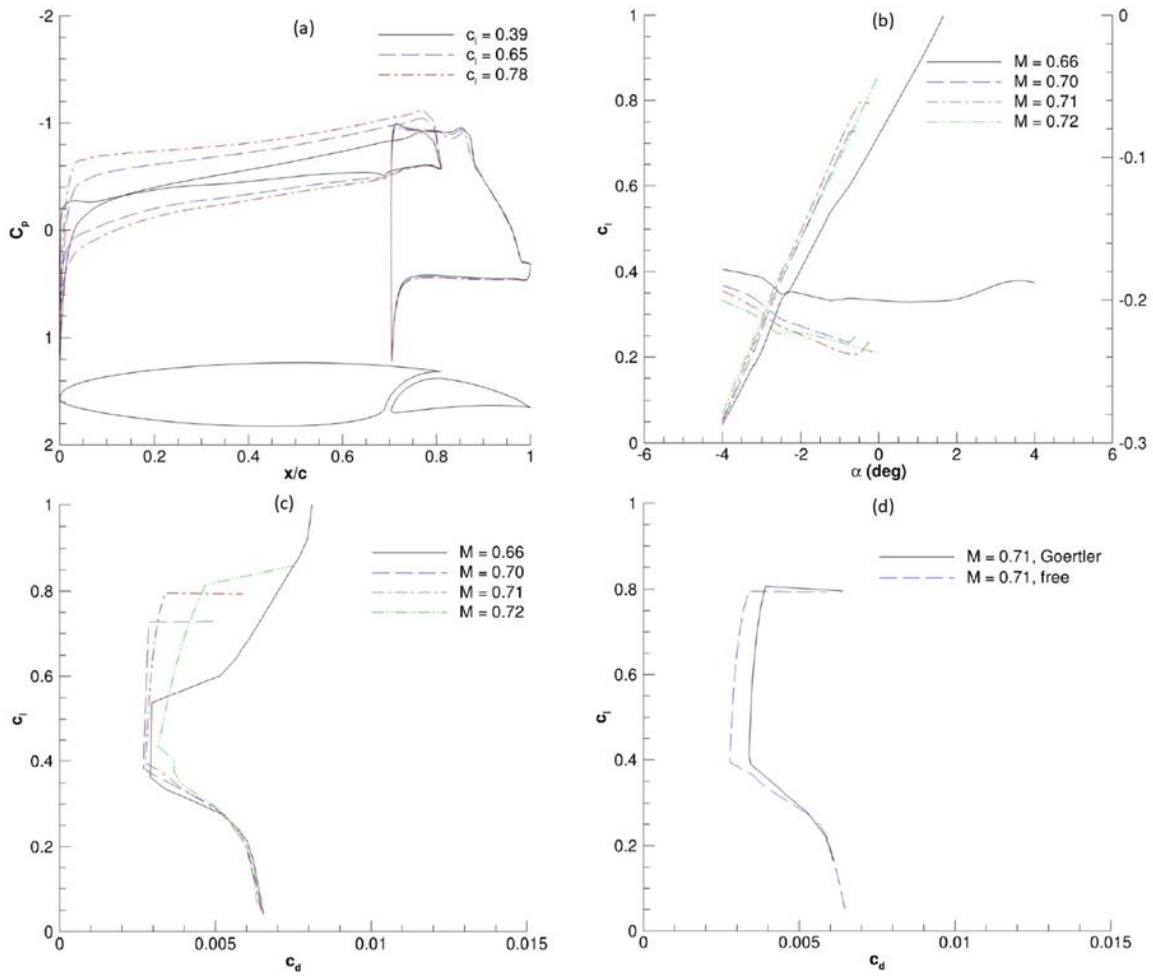


Figure 2-16: Results for SNLF, S207 airfoil at Re=13.2 × 10^6: (a) Effect of lift coefficient on predicted pressure distribution at M = 0.71 [6] (b) Lift and pitching moment at various Mach numbers [Coder-6] and (c) Profile drag at various Mach numbers [Coder-6] and (d) Impact of Gortler instabilities on profile drag at M = 0.71 [19].

the fore element, 55 percent laminar flow on the aft element's upper surface, and laminar flow all the way to the trailing edge on the lower surface of the aft element [5, 19]. Figure 2-16.b-c depict the MSES predicted lift coefficients, pitching moments and drag coefficients for different Mach numbers. For the design Mach number of 0.7 and a slightly lower Mach number of 0.66, we observe from Figure 2-16.c that significantly low levels of drag coefficients (< 0.003) are predicted in the low drag range [19]. There is almost no wave drag for Mach numbers of 0.66 and 0.7. Upon increasing the Mach number, however, we see the appearance of drag divergence due to wave drag becoming a significant portion of the total drag even in the low drag range [19]. An estimated impact of Gortler instabilities was determined by tripping the boundary layer at the entry of the slot on the lower surface of the fore element [19]. The impact of Gortler instabilities on the lift and drag coefficients at $M = 0.71$ and $Re = 13.2 \times 10^6$ is shown in Figure 2-16.d. While the lift coefficients don't change significantly, the drag coefficients increase by around 17% in the low drag range. Even after accounting for the Gortler instabilities, the S207 airfoil met or exceeded the design objectives and was identified as one of the potential airfoil designs for transonic transport aircraft.

X207LS, SNLF Airfoil

An airfoil such as the SNLF, S207 that is designed for transonic conditions produces very different pressure distributions and boundary layer characteristics when tested at low speeds. Figure 2-17.a shows the two different pressure distributions that are obtained over the S207 airfoil at Mach numbers of 0.7 and 0.05. The SNLF, X207LS airfoil was created as a low-speed surrogate of the S207 airfoil to enable testing in a low-speed wind tunnel [35]. The shape of the X207LS airfoil is shown in Figure 2-8.e. X207LS was designed by mapping transonic pressure gradients to an equivalent low-speed airfoil. The airfoil was developed in two stages. First, an inverse design method based on conformal mapping was utilized to develop a single-element airfoil for low speeds [35]. This was followed by adapting the single element airfoil into a slotted configuration. Besides the need to replicate the pressure distribution as produced by S207 at $M = 0.7$ and $Re = 13.2 \times 10^6$, the X207LS airfoil needed to have a reduced lift coefficient ($C_l = 0.45$ as compared to $C_l = 0.65$ for S207) to eliminate any wall separation issues [35].

Figure 2-17.b compares the pressure distributions for the S207 and X207LS airfoils at their design Mach numbers of 0.7 and 0.05, respectively. The X207LS does reproduce the favorable pressure gradients at the upper and lower surfaces of the fore element, closely resembling the pressure gradients of the S207 [35]. However, the pressure gradients on the lower surface of the fore element are less favorable as compared to those for the S207. The major aspects of the X207LS that differ from the S207 are the leading radius of the former being 0.958% chord (compared to the radius of S207 as 1.068% chord) and additionally, the entire X207LS airfoil was smoothed to avoid a predicted pressure oscillation [35]. Figure 2-18 depicts the lift coefficients, pitching moments and profile drag for various Reynolds numbers. As seen from the Figure 2-18.a, MSES predicted the maximum lift coefficient of the X207LS to be above 1.8 for the given Reynolds number range, with the pitching moment coefficient showing low

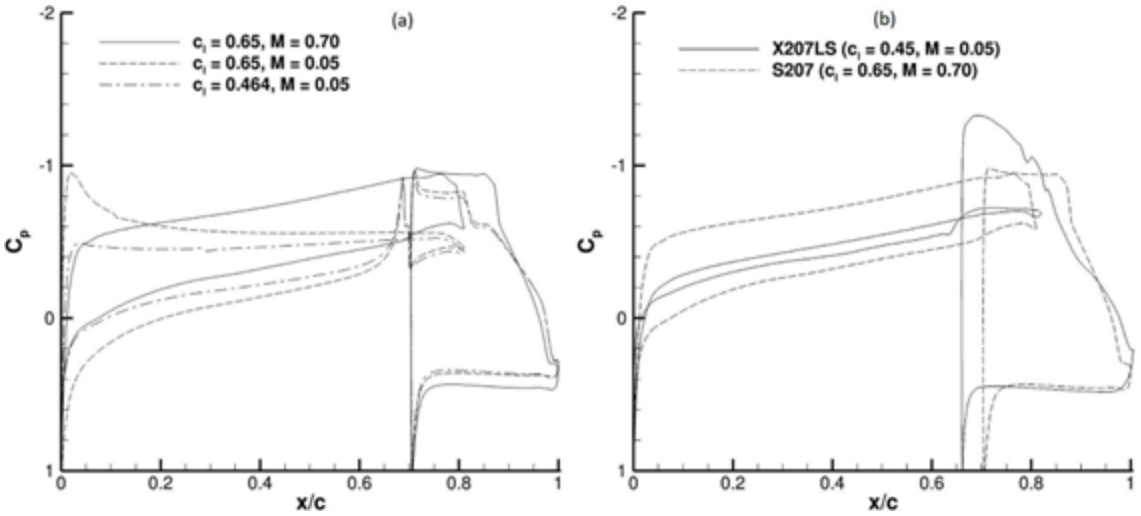


Figure 2-17: (a) Effect of compressibility on SNLF, S207 surface pressure distributions for fixed Re=13.2 × 10^6 (b) Pressure distributions for the SNLF, S207 and SNLF, X207LS at their respective design Mach numbers and Re=13.2 × 10^6 [35].

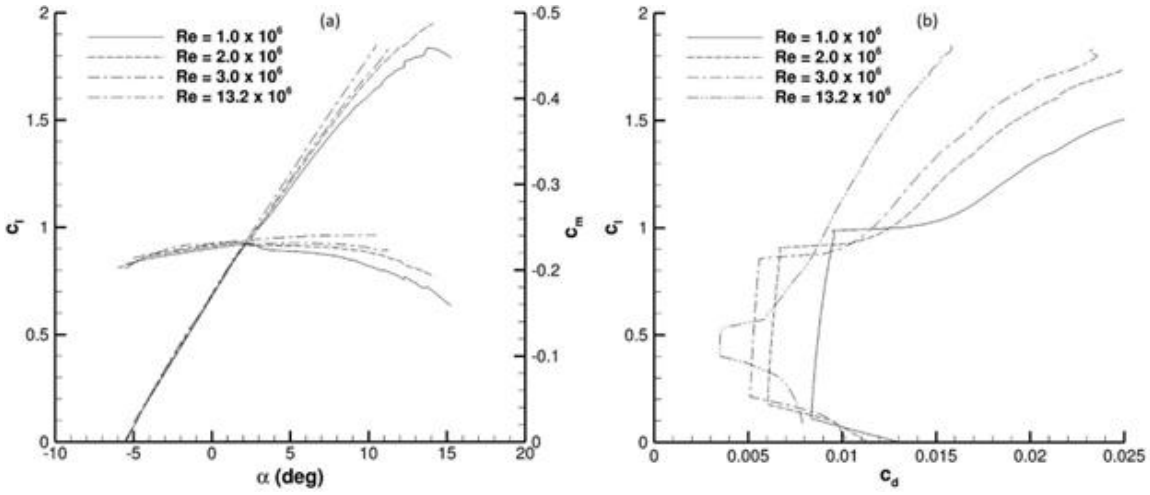


Figure 2-18: Performance of the SNLF, X207LS airfoil at various Reynolds numbers: (a) Lift and pitching coefficients and (b) Profile drag [35]

sensitivity to the Reynolds number for low to moderate lift coefficients. Further, it is observed from Figure 2-18.b that the low-drag lift-coefficient range decreased with increased Reynolds number [35]. Overall, the X207 was found to be a successful surrogate model of the S207 that reproduced similar favorable pressure gradients at low speeds.

Current SNLF Research

As demonstrated by the NASA studies, the LamAiR report, and the development of the SNLF airfoil, laminar flow is rapidly gaining recognition as an advanced solution that can be incorporated into existing aircraft designs. Considering the findings that emerged from the Boeing and MIT studies, as well as the need to meet increasing demand and costs in the aircraft industries, NASA chose to invest in laminar flow technologies further as a part of their University Leadership Initiative (ULI). The NASA ULI program was initiated to encourage partnerships with university researchers and aims to seek innovative ideas that support the goals and interests of the NASA Aeronautics Research Mission Directorate (ARMD) and the overall United States aeronautics community. Upon ARMD's designation of various strategic thrusts for research, NASA ULI then accepts applications from universities and industry partners across the nation and awards the finalists with funding and resources to address their respective thrusts. In the first round of ULI awardees, James Coder of the University of Tennessee was chosen as the Principal Investigator of the Advanced Aerodynamic Design Center for Ultra-Efficient Commercial Vehicles to focus on the ARMD strategic thrust of developing ultra-efficient commercial vehicles [40]. By developing and testing an SNLF airfoil specific to the commercial vehicles NASA is seeking to optimize, the NASA ULI team led by UTK aims to prove the value of investing in the unique airfoil design. The current design that the NASA ULI group is focused on is the S207, SNLF airfoil, and while the design is finalized and has been successfully analyzed theoretically, development is still ongoing.

The core goal of the Advanced Aerodynamic Design Center for Ultra-Efficient Commercial Vehicles centers around developing the SNLF airfoil so that it can be integrated with Boeing's Transonic, Truss-Braced Wing (TTBW) Aircraft to create a more fuel-efficient aircraft, as depicted in Figure 2-19. The ULI researchers are analyzing various aspects of the SNLF airfoil's performance, methods of analysis and optimization, and advanced technologies that would be integrated into the airfoil to better improve fuel and energy efficiency. These parallel strategies refine the airfoil's shape and behavior to integrate with the Boeing airplane, while also exploring cutting-edge technologies that would greatly enhance multiple aspects of the airfoil's performance, such as aerodynamics, structures, propulsion, stability, and acoustics [41]. The various branches of this research are discussed in the order of their respective technical categories: aerodynamics, structures, and advanced technologies.

Aerodynamics

The ULI team's aerodynamics research is two-fold; while some researchers focus on optimizing the design and geometry of the S207, SNLF airfoil and how it affects its



Figure 2-19: Configuration of the Boeing Transonic, Truss-Braced Wing [41].

behavior, others investigate different methodologies and technologies that can enhance the S207's aerodynamic benefits. One method of analyzing the S207's aerodynamic behavior is utilizing computational fluid dynamics (CFD) to make high-lift predictions. ULI researchers Coder and Ortiz-Melendez, along with Shmilovich from Boeing, conducted a study on the most suitable configuration of the aft element of the SNLF airfoil (in this case, the S204 airfoil was used as a baseline) in order to satisfy the high-lift target for commercial aircraft [42]. The study aimed to explore two different configurations of the aft element of the SNLF airfoil, the first being a micro-flapped aft element, and the second being a Fowler flap aft element. In total, the four combinations that these versions produce are a baseline S204 aft element, a deflected aft element, a deflected micro-flap, and both a deflected aft element and micro-flap [42]. The computational approach chosen was a Reynolds-Averaged Navier-Stokes (RANS) procedure, which is used to calculate the flow near maximum lift by integrating the lift-forces of the system, as shown in Figure 2-19 [42]. Through the use of CFD in the design and verification process, the required costs and efforts for preliminary wind-tunnel testing have been greatly reduced. Meshes of the S204 airfoil were also generated with the use of NASA's Chimera Grid Tools, and multiple grid systems were produced to incorporate the two flap configurations being studied, as shown in Figure 2-20 [42]. By the conclusion of the study, results depicted that the S204 airfoil micro-flap (when deflected downwards) and the Fowler flap have provided a greater maximum lift than the airfoil without the flap [42]. Thus, this research is paving the way for future studies that investigate these configurations in more depth and in conjunction with the use of an active flow control device to further optimize the SNLF airfoil's performance in terms of high lift.

In addition to Coder and Ortiz-Melendez's work with CFD, the Mavriplis CFD lab at the University of Wyoming has also made contributions to the NASA ULI team concerning high-fidelity aerodynamic analysis of the S207 airfoil. Their in-house-developed application NSU2D (Navier-Stokes Unstructured 2D) has been utilized to study various loads on the wing at cruise conditions. It should be noted that results acquired thus far are relative to a digitized S207 geometry, as the proprietary coordinates are not currently accessible. Regardless, for a Mach number of 0.7, angle of attack of -1.3, and a Reynolds number of 13.2 million; a lift coefficient of 0.6505 was achieved. This value aligns well with original design specifications and already published results [5, 19]. However, a drag coefficient of 0.0032 was observed. This is five counts higher than the low-drag profile target value of 0.0027 [5, 19]. This can partially be attributed to the small geometric discrepancies that arise as a result of the digitizing process, but other possibilities are under consideration. NSU2D is a RANS solver and with the implementation of a transition model, convergence becomes more difficult to achieve. Though current results, shown in Figure 2-21, are sufficient within the current scope of this project, further work is necessary to eliminate oscillatory behavior. Additionally, extensive study of the flow through the slot is still necessary, as the greatest differences between published data and NSU2D results are located on an interval equal to roughly 69-81% of the chord length. A convergence and grid study will be employed to fully capture and validate the physical phenomena present. Three-dimensional analysis with

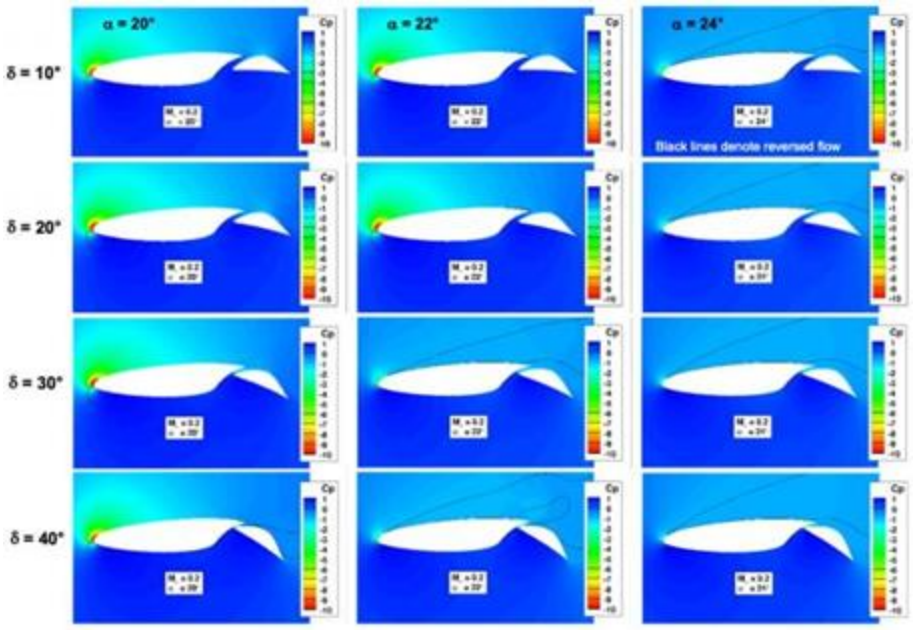


Figure 2-20: Effect of Flap Deflection on the Flow Structure near Maximum Lift [42].

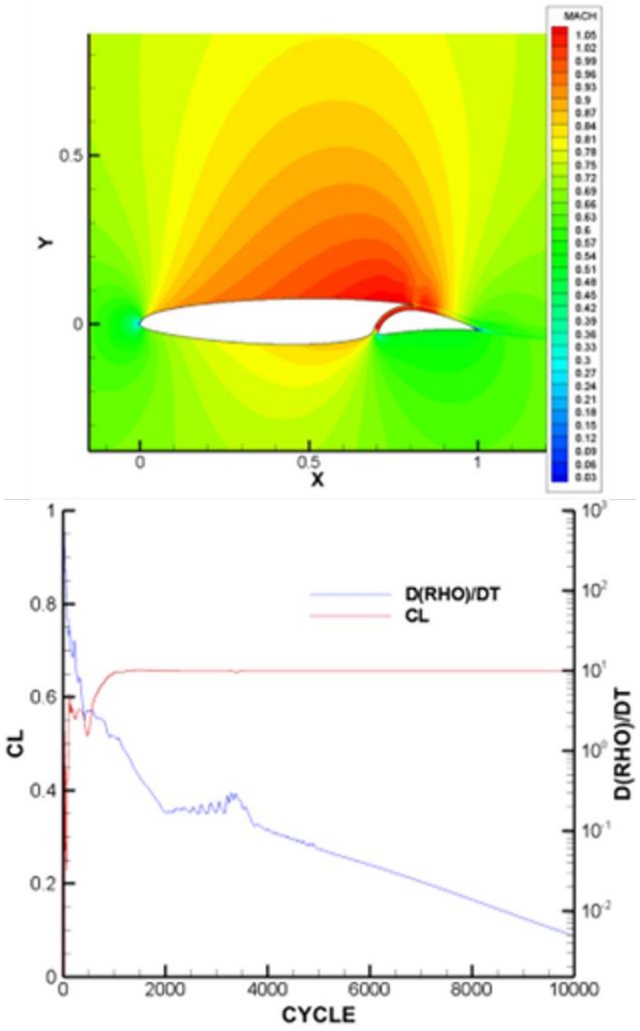


Figure 2-21: Digitized S207 NSU2D Results with Implemented Transition Model for Mach = 0.7, α = -1.3°, Re = 13.2 x 10^6. Provided Courtesy of the Mavriplis CFD Lab. (a) Mach Flow Field of S207, SNLF Airfoil. (b) Convergence History.

NSU3D will also be pursued in collaboration with colleagues fabricating a structural model at Penn State University.

Another example of the methodologies that explore ways to better improve the S207's performance is by identifying and decomposing the types of aircraft drag to inform the SNLF's design and optimization process. While multiple methods for drag decomposition exist, maintaining a consistent methodology is extremely important, especially when the design deviates from traditional aircraft configurations, as in the case of Boeing's TTBW design. Therefore, one facet of the NASA ULI project is to explore an alternative methodology based on partial-pressure fields in compressible flow calculations, which provides more insight into pressure drag and could also present more resolved surface-pressure contours that would better guide the high-performance adjoint-based optimization in the future [43].

Structures

Another facet of the NASA ULI's research and development effort is the structural design and optimization of the S207's wingbox and fore-aft slot connectors. As detailed in Ch. 3: A review, the S207 SNLF airfoil observed higher lift occurring from the aft element compared to many single element airfoils. While aft loaded elements aren't uncommon, the slot between the high-lift aft element and the fore element introduces a new challenge. That is how to support and transfer the high-lift aft element load to the fore element while maintaining the slot and its benefits to the aerodynamic performance. To achieve this several studies were performed to investigate an efficient slot connector and its effects on the structural components of the wingbox.

The first set of studies performed focused on the slot connectors. The goal of these investigations was to provide a preferred slot connector shape and location that transfers the high-lift aft element load to the fore element and minimizes the disturbance to the aerodynamic performance within the slot, i.e. laminar flow. An initial eight connector shapes and locations were evaluated. Structural analysis using Abaqus CAE informed of the preferred shape and location due to stress buildup and aft deflection [44]. Computational fluid dynamics (CFD) followed up to investigate the effect that the slot connector's location within the slot had on the laminar flow. A comparison from this study is shown in Figure 2-22, where a baseline span, no connector, was compared with that of an internal and external slot connector span. The slot connector was then adjusted to a more streamlined shape as shown in Figure 2-23. This symmetric shape was chosen to reduce the impedance on the local laminar flow. Structural analysis was performed to evaluate the adjusted slot connector's preferred location within the slot. The final substudy of the investigation was an optimization of the slot connector's number and individual size along the half-span of the wing. Considerations from the previous substudy dictated the slot connector's shape and location within the slot. The optimization was a one-factor-at-a-time (OFAT) study with the goal of minimizing the weight of the slot connectors while considering the drag produced by each slot connector. Figure 2-24 shows the OFAT for the weight and Figure 2-25 shows the OFAT for drag. The resulting number of slot connectors was further influenced by a study for flutter stability performed by Bottai et al. [45].

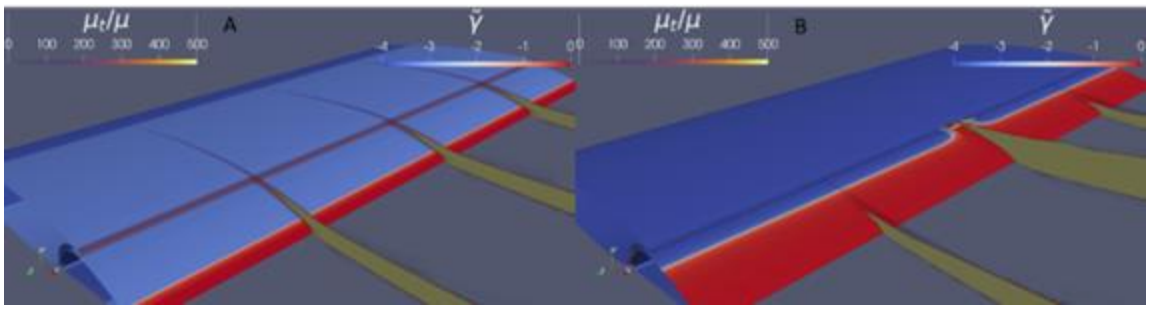


Figure 2-22: Comparison of the turbulent viscosity ratios of a 200" baseline region with no connector A) and a circular connector B).



Figure 2-23: The adjusted NASA CRM shape utilized for the fore-aft element connector study.

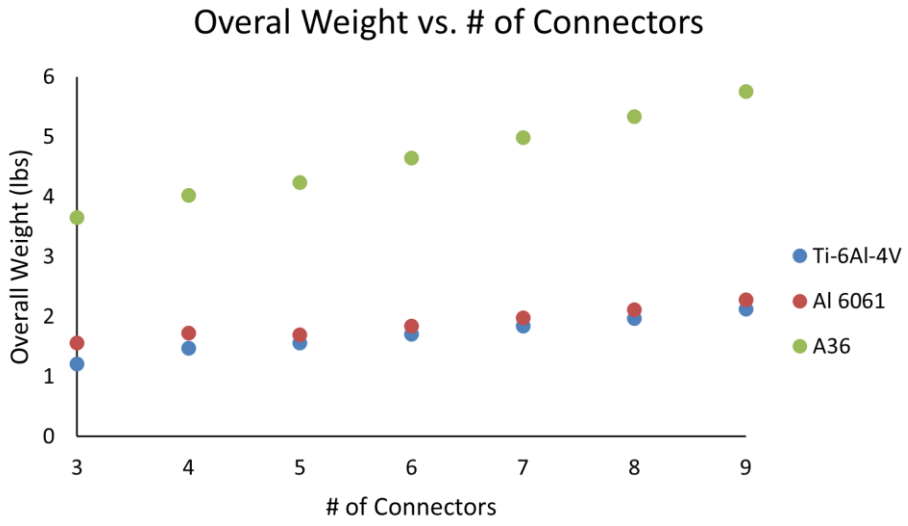


Figure 2-24: Weight of various connector numbers required to transfer flight loads from aft element to fore element.

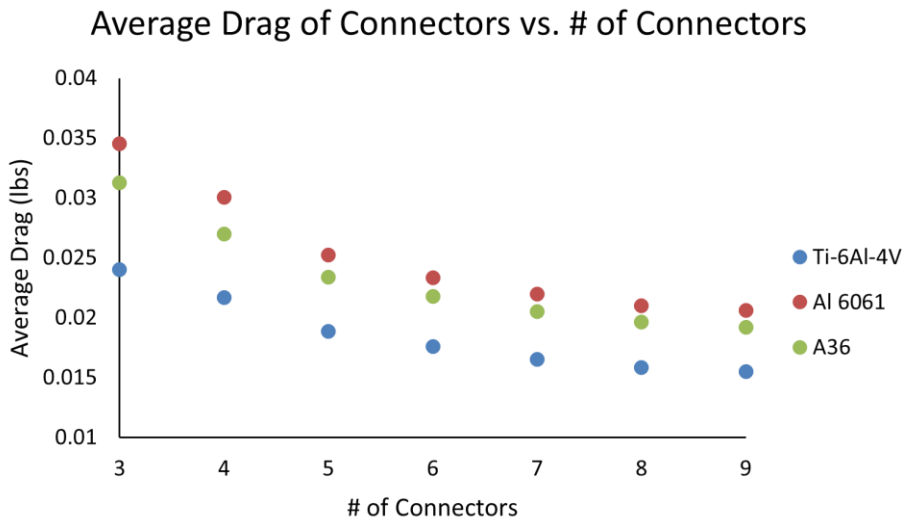


Figure 2-25: Drag acting on various connector numbers showing impedance of local laminar flow in the slot.

The next major concern was the topology of the aft element and what components of the aft wingbox were required to transfer the high-lift aft load to the fore element. To assist in weight reduction goals, topology optimization was utilized to evaluate material distribution in the aft element supported by the slot connectors. Solid Isotropic Material with Penalization (SIMP) was used as the built-in Abaqus topology optimizer [46]. The results of the topology optimization highlighted that an aft element spar was not needed to transfer the high-lift load to the fore element.

Finally, a full half-span topology demonstration was performed using Abaqus CAE. A representation of the ribs and spars for the full geometry can be seen in Figure 2-26. Sizing was performed using structural mechanics and beam analysis. Demonstration of the slot connectors placed within the full half-span geometry provided vital detail on how the wing would deflect and transfer load with a 'floating' aft element.

Advanced Technologies

When looking into various advanced technologies that the NASA ULI is exploring, one example is the experimental research being conducted with inclined fluidic oscillators for active flow control to improve boundary layer separation control and heat transfer, among other aspects [47]. Fluidic oscillators are devices that generate a continuous stream of oscillations without the use of moving parts. In the main chamber of the oscillator, the supplied flow enters through the inlet and passes through towards the outlet, but through a narrow feedback channel, small amounts of the stream pass back through to the other side of the mixing chamber and switch sides, thus causing the flow to have an oscillating frequency as it recirculates [48].

In a similar study, presented at AIAA SciTech 2021, active flow control is considered in order to recover the shortcomings of SNLF airfoil performance while also meeting the surface constraints for laminar flow [49]. Active flow control applied in the slot of a slotted natural laminar flow airfoil was analyzed using computation fluid dynamics through a modified version of OVERFLOW. A digitized S207 airfoil with a morphed leading edge, provided by UIUC, was used in a sensitivity analysis to determine how the performance of the airfoil would be affected by actuation ports based on the location, mode, and mass flow, as shown in Figure 2-27. Actuation ports, based on blowing and suction, were considered such that they are consistent with potential integration of flow control systems on future aircraft equipped with natural laminar flow wings.

Blowing actuation demonstrated significant improvements in the L/D along the range of angles of attack and each location considered, with slight improvements in the C_l. When positioned along the main element, the application of blown actuation demonstrated larger improvements in the $C_{l,\,max}$ and slightly delayed stall. This behavior suggests that the boundary layer is being re-energized and active flow control is providing separation control. Suction actuation demonstrated little impact on the overall performance of the airfoil but is still important to quantify for integration in practical flow control layouts [49]. The initial results are encouraging since an increase in L/D during take-off can lead to a shorter runway, longer range, and higher payload. Moreover, the takeoff and climb-out portions of the flight profile often determine the engine rating

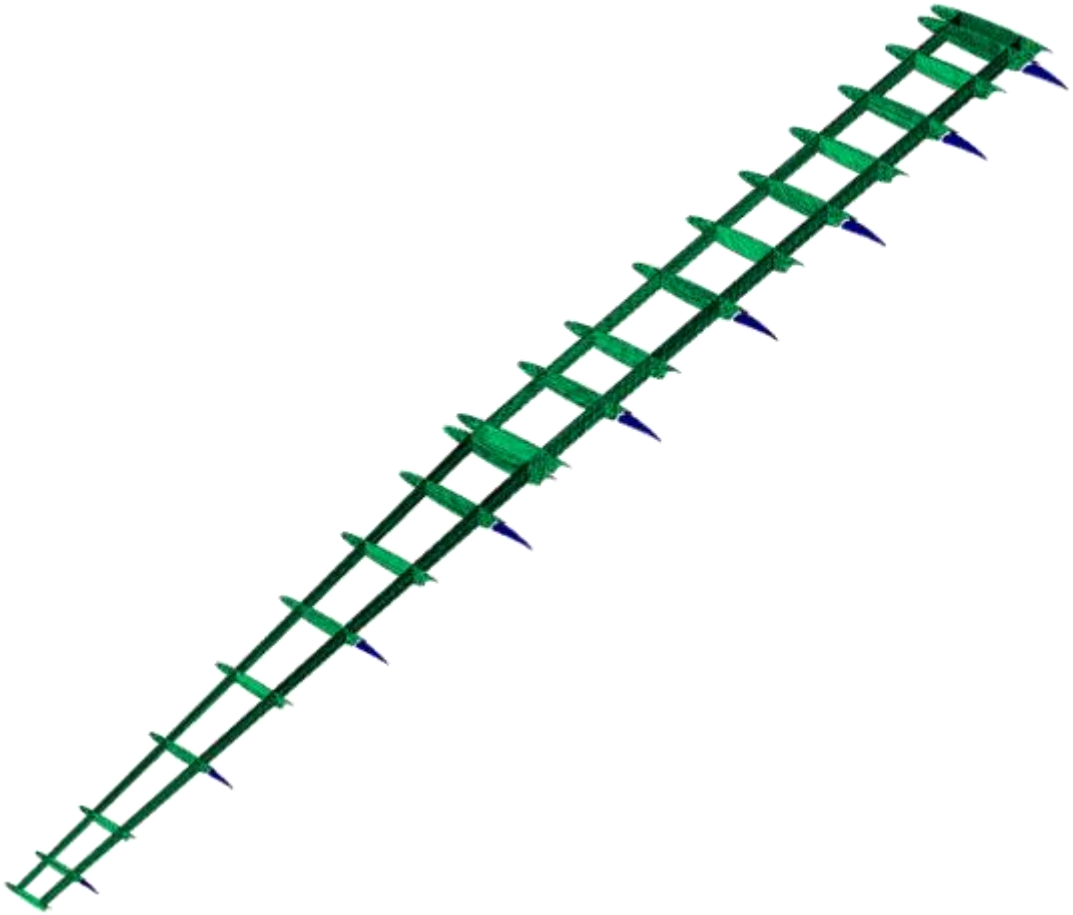


Figure 2-26: Overview of fore and aft element rib and spar placements. Green dictates fore element components and blue indicates aft element components.

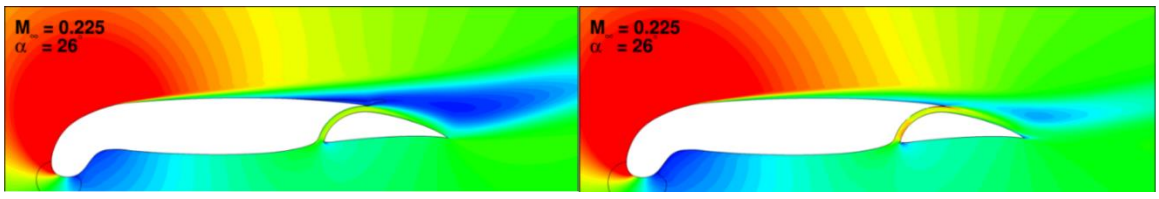


Figure 2-27: Mach Contours of baseline flow (left) and active flow control applied along the slot (right) at α=26°. Provided courtesy of Boeing Research and Technology.

and thereby the engine core size. Therefore, applications that improve the *L*/*D* will enable a reduction in the engine core size, resulting in lower airplane weight. Consequently, this will lead to lower fuel consumption and reduced emissions. Since 2D analysis only provides general guidance, implementation of these flow control systems on a representative SNLF wing will be required to establish more realistic objectives for an integrated flow control system.

Another example of advanced concepts that the ULI team is investigating is the aero-elastic behavior of flutter mitigation of multi-element wings, such as the S207, SNLF airfoil. Aero-elastic instability arises from the interactions of inertial, elastic, and aerodynamic forces on the wing. The instabilities are characterized as either static or dynamic instabilities. Divergence is a static instability that occurs at high angles of attack when the elastic twisting moment is no longer sufficient to counterbalance the aerodynamic pitching moment. The consequences include loss of aerodynamic efficiency and high risk of structural failure. Flutter is a dynamic, oscillatory instability that can be triggered by any external perturbation (e.g., gust, sudden change in angle of attack) on the wing and can cause structural failure. Task 1.08 focuses on the aero-elastic stability of the strut-braced (SB) SNLF wing. A beam-rod aero-elastic framework in modal space has been developed with static equilibrium calculation and time-marching solution capabilities [50]. The aerodynamics are based on Theodorsen's theory for two aerodynamically independent flat plates. The two elements are structurally coupled with springs. The component mode synthesis method is employed to study the effects of varying connection stiffnesses and locations. The mode shapes are obtained by performing a frequency analysis of a three-dimensional finite element model of the SNLF wing using the commercial software ABAQUS. The wing model was developed to include structural reinforcement while preserving the aerodynamic shape of the wing. Future work includes improving the aerodynamic model to capture the fore-aft element interactions in the aero-elastic calculation tool.

Future Goals and Conclusions

As previously discussed, the NASA ULI team is currently in the process of optimizing the S207's shape and geometry to best fit the dimensions of the target vehicle, the Boeing Transonic, Truss- Braced Wing aircraft, while also investigating other enabling technologies to further reduce drag and enhance maximum lift on the wing. Shortly after completing the S207 airfoil's development and finalizing the design, the SNLF airfoil will be experimentally verified by conducting wind tunnel experiments at the NASA Ames 11ft Transonic Wind Tunnel to prove the technology's efficiency and functionality. The wind tunnel testing will be the final step in the NASA ULI team's five-year project, and if successful, will conclusively demonstrate the SNLF airfoil's viability as a revolutionary wing design and will most likely lead towards a permanent incorporation into the Boeing TTBW aircraft.

In summary, the need for advancing aircraft optimization by finding solutions to global aircraft issues that can be incorporated into existing structures is prevalent in the aerospace industry. In the area of reducing wing profile drag and optimizing the lift-to-

drag ratio, the SNLF airfoil is an elegant solution and, by allowing almost 90% of its surface to achieve laminar flow, can contribute to the N+3 goal of reducing fuel consumption by 70%. The slot configuration of the airfoil extends the favorable pressure gradient farther along the wing, increasing the extent of laminar flow, which in turn decreases the skin friction drag and increases the maximum lift coefficient, thus improving overall flight efficiency.

Reviewing the conception of the SNLF airfoil and its various developments provides a recap of its recent history. In addition, discussing previous projects that investigated the use of laminar flow in future aircraft designs provides insight as the ULI team works towards improving the airfoil to integrate it with the Boeing Transonic, Truss-Braced Wing aircraft. Therefore, this paper successfully traces the need for laminar flow technology, details the developments on the novel SNLF airfoil design, and surveys recent developments of the NASA ULI research on the SNLF airfoil and their progress towards incorporating NLF technology in commercial aircraft.

Chapter Three

A review

Aft-Loading on Airfoil

The slotted, natural-laminar-flow (SNLF) airfoil differentiates itself from other airfoils with its aft element producing a large amount of lift as it recovers the pressure gradients [5]. The slot in the airfoil allows the wing to achieve natural-laminar-flow (NLF) on the entirety of the lower surface of both elements and upper surface of the fore element. The NLF reduces the profile drag and increases the factor of merit (FOM). The result is that the aft element produces higher lift as it recovers to the free-stream pressure. During cruise the aerodynamic and pressure centers shift further aft away from the quarter chord.

The aerodynamic center is the chord location when the pitching moment coefficient, C_m, doesn't vary with the lift coefficient, C_L [51]:

$$\frac{x_{a.c.}}{c} = -\frac{dc_{m_{c/4}}/d\alpha}{dc_l/d\alpha} \qquad \textit{Equation 3-1}$$

where $x_{a.c.}$ is the chord location of the aerodynamic center in relation to the quarter chord, c is the chord length, $dc_{mc/4}$ is the change in the coefficient of moment about the quarter chord, $d\alpha$ is the change in the angle of attack, and dc_l is the change in the lift coefficient.

Figure 3-1 and Figure 3-2 detail coefficient of pressure, C_p, plots of the S207 SNLF airfoil for cruise and take-off conditions [19]. The C_p, C_L, and C_m of the S207 SNLF airfoil indicates that as the aircraft accelerates toward the transonic regime, the $x_{a.c.}$ shifts further aft closer to the mid-chord location [19, 52]. The center of pressure, *c.p.*, for an airfoil is the location along the chord where all the aerodynamic pressure can be represented as a concentrated force where no moment would act about that axis [51]. Aircraft dynamics usually don't use the *c.p.* as it shifts during the aircraft's change in angle of attack, α. The concentrated load is typically placed at the quarter chord or the $x_{a.c.}$. As the airfoil reaches maximum lift at cruise, the C_p shifts further aft away from the quarter chord as the aft element provides a larger percentage of the lift during this condition.

Figure 3-3 shows a comparison of the S207 SNLF airfoil *Cp* in relation to a single element airfoil [19]. Included in this comparison are the NASA CRM.65 and S207 SNLF in cruise conditions. This difference can also be observed when comparing to the Boeing 737, a similar class aircraft to what the S207 will be applicable to [53]. The S207 SNLF airfoil's aft element produces a considerable amount of lift during cruise while the

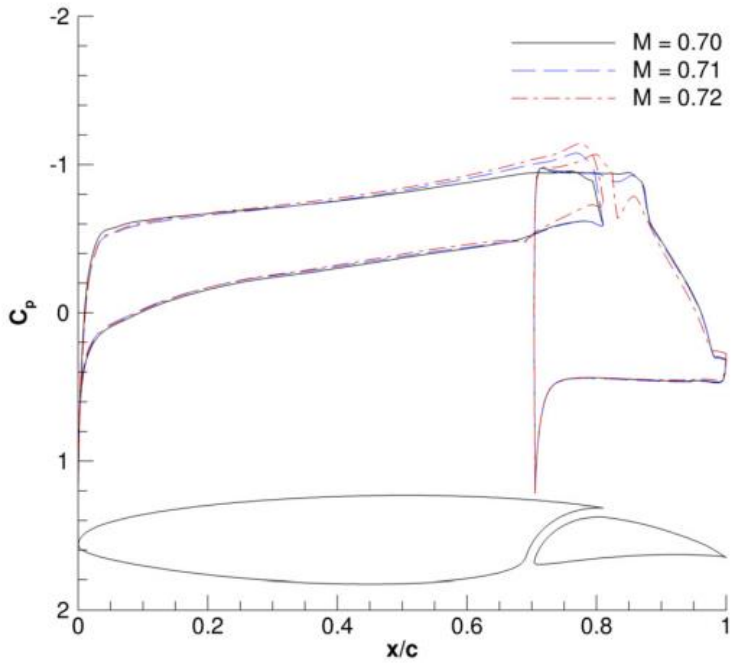


Figure 3-1: Cp plot distributions for Cruise Conditions of the S207 SNLF airfoil with Cl = 0.70 and Re = 13.2 x 10^6 [19].

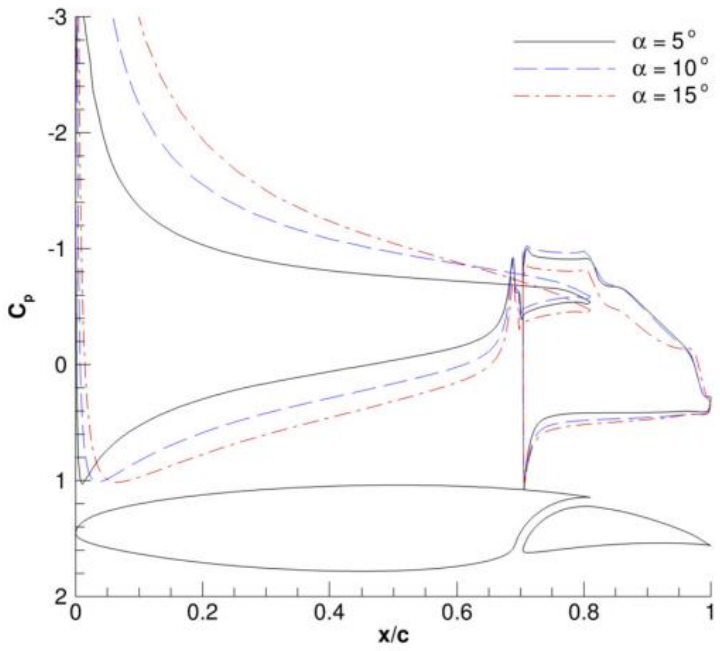


Figure 3-2: Cp plot distributions for Take-off conditions of the S207 SNLF airfoil with M = 0.225 and Re = 16.0 x 10^6 [19].

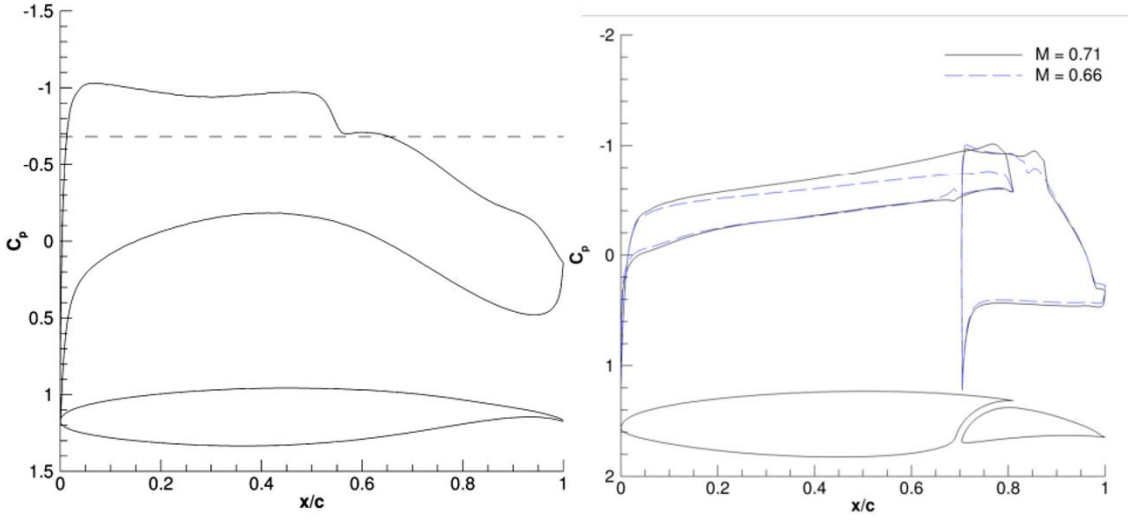


Figure 3-3: Comparison of a single element airfoil, NASA CRM (left), to a slotted airfoil, S207 (right). Graphs depict the Cp of the two airfoils [19].

trailing edge of the single element airfoils display little to no lift. This difference will shift the *c.p.* towards the aft and require a larger rear spar to support the additional lift in both the cruise and the take-off conditions.

Aft loaded airfoils are not novel and can be seen in a variety of airfoils with supercritical and motorsport applications, such as the Boeing 767 and 777 [54-57]. The aft loading assists in high-lift applications and pressure recovery, thus creating a higher maximum C_L. The S207 SNLF airfoil differentiates itself from other aft loaded airfoils with its slotted design. The aft element of this two-element system produces the aft load but is not rooted at the fuselage. It is left 'floating' to be supported by the rear spar of the fore element. With the requirement that the slot between the fore and aft element remain open during cruise, the aft loading must be transferred to the rear spar with the minimal number of connections required while remaining stiff enough to maintain the slot. The concentrations of these aft loads require additional weight to be factored into the rear spar to support the loading as well as material in the aft element for it to remain stiff.

Flaps

One of the main constraints with the SNLF airfoil is the continual slot width between the fore and aft element. While the adaptation of SNLF airfoil onto commercial aircraft is revolutionary and no connector design has been investigated for the aft to fore element application, aircraft have several components that fold or extend out of the wing. These flight control systems assist with safety and lift [58]. These are broken into two categories, the primary and secondary systems and are connected to the aircraft wing in a variety of fashions. It should be noted that the major components of these connections are proprietary in nature and slightly differ from the application of the SNLF airfoil slot connectors. Thus, some initial knowledge of how they are connected can be acquired and adapted for use with the SNLF airfoil.

The primary control system of interest are the ailerons. Ailerons are conventional applications on modern-day aircraft. Their first introduction occurred in 1909 by a French aviator Henri Farman who installed flaplike aileron's to the trailing edge of his biplane [51]. Other aviators soon followed, including the Wright brothers. Ailerons assist pilots in controlling the roll about the longitudinal axis, thus providing lateral stability [58, 59]. Standard ailerons are connected and controlled through a system of cables, pulleys, and bellcranks, and metal rods or with a system of hinge joints and actuators [60]. The ailerons rotate in place on that hinge.

Secondary control systems consist of flaps and spoilers. Spoilers are deployed on landing to disrupt the smooth airflow, thus increasing the drag. Flaps assist with high-lift capabilities of aircraft. These control systems are also attached to the trailing edge of the airfoil. Plain flaps were introduced by the Royal Aircraft Factory in 1914 as an evolution of the aileron's produced by Farman. Single-slotted flaps appeared in 1920 by three different aviators, G.V. Lachmann, Sir Frederick Handley Page, and O. Mader. The split flap was introduced by Orville Wright in 1920 while working for the Army Air Corp's but did not see application until 1932 by Jack Northrop. Harlan D. Fowler of the United States Army Air Corps produced the final flap of discussion, the Fowler flap, in 1924

[51]. Flaps are capable of increasing lift and induced drag providing the ability for high cruising speed and low landing speed [58].

The plain flaps assist with *CL* by increasing the airfoil's camber while shifting the *c.p.* towards the aft inducing a nose-down pitching moment. Similarly, the split flap increases the *CL* by extending from the lower surface of the wing. A slotted flap is more common on modern aircraft. These are connected by a hinge and create a sort of slotted airfoil that provides a higher *CL* and maximum increase in drag without effecting the extra lift produced. An example of this sort of flap can be seen in Keller [61], where the Kruger flap was investigated for a natural laminar flow wing. Another type of slotted flap is the fowler flap that extends outward from the trailing edge instead of rotating. This increases the wing area and camber of the wing to produce more lift without inducing too much drag initially. As the flap continues to extend it deflects increasing drag with slight increase to lift.

As flaps are more similar to the aft element of the SNLF airfoil their connections were especially of interest. These control systems require a structural member to attach and transfer the load onto the main components of the wing. The flaps are connected to the wing by a flap track covered by a fairing [60, 62, 63]. The flap track serves to connect the flaps and hold the servos and wiring required to extend the flaps. The fairings help maintain the aerodynamics of the aircraft wing. However, the multiple fairings imposed on the underside surface of the aircraft wing results in a penalty on the performance by increasing the drag and creating turbulent airflow [64]. For extension the connections require the use of a hydraulic ram actuator or track that allows motion.

The main difference between the S207 SNLF airfoil's aft element and ailerons and flaps is that the current iteration is to remain constant during flight. It does not require a track or hydraulic ram actuator to shift positions. However, it must remain constant in its separation from the fore element. Another challenge is the disruption of the local laminar flow. Flaps and ailerons are connected to internal wing structures with the use of controllable mechanisms as previously discussed such as the flap track and the ram actuator. These allow the pilots to shift their position in flight. The ram actuators seen on aircraft are circular actuators that extend shifting the control surface out. This approach is efficient but relies on additional bracing along the control surface span. The flap track is traditionally hidden within a fairing. The fairing produces turbulence on the adjacent surfaces of the wing. Both designs are developed with the main goal of connecting and moving the control surface while the aerodynamic disturbance isn't as crucial when compared to the SNFL airfoil. The SNLF airfoil requires that the aerodynamic disturbance be minimized, and that the aft element doesn't shift in cruise. As no desire to control the location of the aft element has been expressed, traditional connectors as discussed aren't required and their lack of aerodynamic efficiency deters their implementation.

Topology Optimization

Topology optimization is a mathematical method that optimizes material distribution within a given design space, for a given set of loads, boundary conditions, and constraints with the goal of maximizing the performance of the system [46]. Topology optimization is

becoming more prevalent in aerospace design. The foundation of topology optimization was derived by Michell in 1904 [65], in which he studied the structural optimization of trusses using multiple loading patterns. Michell's work was expanded on by Drucker and Prager in 1952 using a yield criterion for pressure dependent soils [66]. Further implementation of topology optimization was performed by Dorn *et al.* using the 'ground structure approach' and Bendsøe and Kikuchi who introduced the 'homogenization approach', in 1964 and 1988 respectively [67, 68]. Topology optimization differs from generic shape optimization and size optimization by allowing the design space to obtain any shape to maximize the performance compared to predefined configurations. Figure 3-4 illustrates the difference between shape, size, and topology optimization [69]. Topology optimization has continued to evolve into a mature design tool for industries such as aerospace, automotive, and infrastructure [70-72]. In the aerospace industry topology optimization for aircraft wing design has been flourishing with several researchers investigating not just topology optimization, but multi-disciplinary design optimization (MDAO) with aero-structural or thermal-structural interactions [73-76]. A general review of topology optimization in aircraft design can be explored in Zhu et. al., where the authors discuss different optimization applications for use with pylons, ribs, engine brackets, and other aircraft components [77].

Topology optimization is generally an initial design phase tool. Post-processing is required to ensure that the optimal structure meets requirements in manufacturing, ease of connection, and safety. Manufacturing of a complex structure requires time and money. Computer numerical control (CNC) and additive manufacturing (AM) techniques have matured allowing these more complex shapes to be made. However, without dedicating CNC and AM machines to only produce one component the plausibility of using an optimal shape is low. In respect to the proposed research, topology optimization is utilized to evaluate the design space of the high-lift 'floating' aft element. The application of topology optimization is vital to the study's goal. Abaqus CAE is the software selected to perform the topology optimization for the study. As such, the mathematics behind the topology optimization are referenced from the Abaqus CAE User's Manual [78]. This is only a review of topology optimization, for a more thorough explanation behind the theory of topology optimization refer to detailed texts by Bendsøe *et al.* [79, 80]. The stiffness-based topology optimization calculates the compliance, the measure of the structures overall flexibility or stiffness defined as the sum of the strain energy of all the elements, written as:

$$U = \sum u^t k u \qquad \textit{Equation 3-2}$$

Where U is the strain energy, u is the displacement vector, and k is the global stiffness matrix. k is calculated using the uniform material properties density, elastic modulus, and yield strength. The compliance of a structure is the reciprocal of the stiffness. By minimizing the strain energy, the global stiffness of the structure is maximized. This is the ideal process for the aft element since the governing loads are driven by pressure. The structure is broken into elements with relative densities and material properties. The

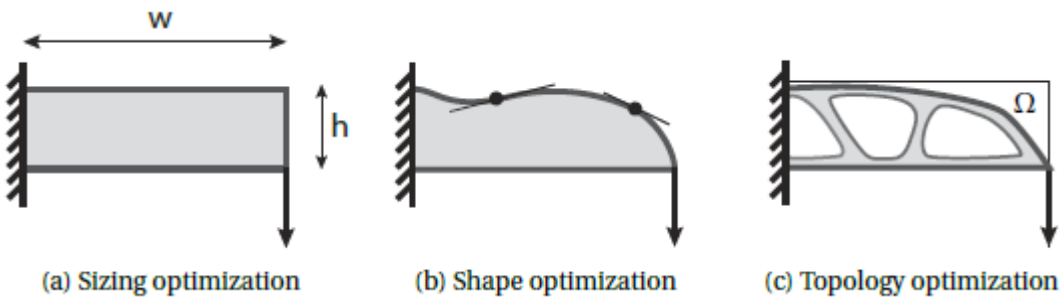


Figure 3-4: Categories of Optimization Methods [69].

topology optimization process calculates the *strain energy density* (*SED*) of the elements. To accomplish this the loading vector *F*, and stiffness matrix are used to calculate the displacement vectors. The stresses and strains for each element are calculated for the *SED* to be calculated.

$$F = k_0 u \qquad \textit{Equation 3-3}$$

$$SED = \frac{1}{2}\sum_i \sum_j \sigma_{ij}\epsilon_{ij} \qquad \textit{Equation 3-4}$$

This will be the objective function defined by the goal of the optimization, and can be stated as:

$$\min\left(\Phi(U(x), x)\right) \qquad \textit{Equation 3-5}$$

Where Φ is the objective function depending on the state variables, *U*, and the design variables, *x*. Formulas for the objective functions that maximize or minimize *N* design responses are stated as:

$$\Phi_{min} = \min\left(\sum_{i=1}^{N} W_i(\varphi_i - \varphi_i^{ref})\right) \qquad \textit{Equation 3-6}$$

$$\Phi_{max} = \max\left(\sum_{i=1}^{N} W_i(\varphi_i - \varphi_i^{ref})\right) \qquad \textit{Equation 3-7}$$

W_i is a weight factor and φ_i^{ref} is a reference factor given to each design response, φ_i. Default values for the weighting factor and reference factor are 1.0 and 0.0 respectively. Constraints can also be placed on the objective functions and design response.

$$\Psi_i(U(x), x) \leq 0 \qquad \textit{Equation 3-8}$$

$$K_i(x) \leq 0 \qquad \textit{Equation 3-9}$$

Where Ψ is the constraint placed on the optimization problem and K is the constraint applied to the design variables. The constraints prevent the function from arriving at trivial solutions. One such constraint would be to constrain the weight to a percentage of the initial value. Another constraint can be the displacement in a region being limited to a certain amount. The user may also freeze sections of the structure. This would allow the user to keep sections of the structure unaffected and it would be easier to apply geometric constraints for applications such as connections to adjacent structures.

When elements reach a local *SED* lower than that of a critical value, the element density is penalized to a very low density. This method is known as the Solid Isotropic Material with Penalization (SIMP) [46]. The optimization is looped where the stiffness matrix, displacement vectors, and SED values are calculated over the iterations. The iterations continue until the objective function and constraints have been met. Once these objectives and constraints have been met, a final revision is made prior to finalizing the structure.

An example of the topology optimization process is demonstrated by Airbus's design of aircraft wing ribs conducted by Altair Engineering [70]. Figure 3-5 displays the process, where first the shape is defined then ran through a topology optimizer. The optimal design sufficiently carries the load applied to the structure. However, as demonstrated in Figure 3-5, the optimal design is not practical to manufacture. The optimal design is post-processed to smooth out the design.

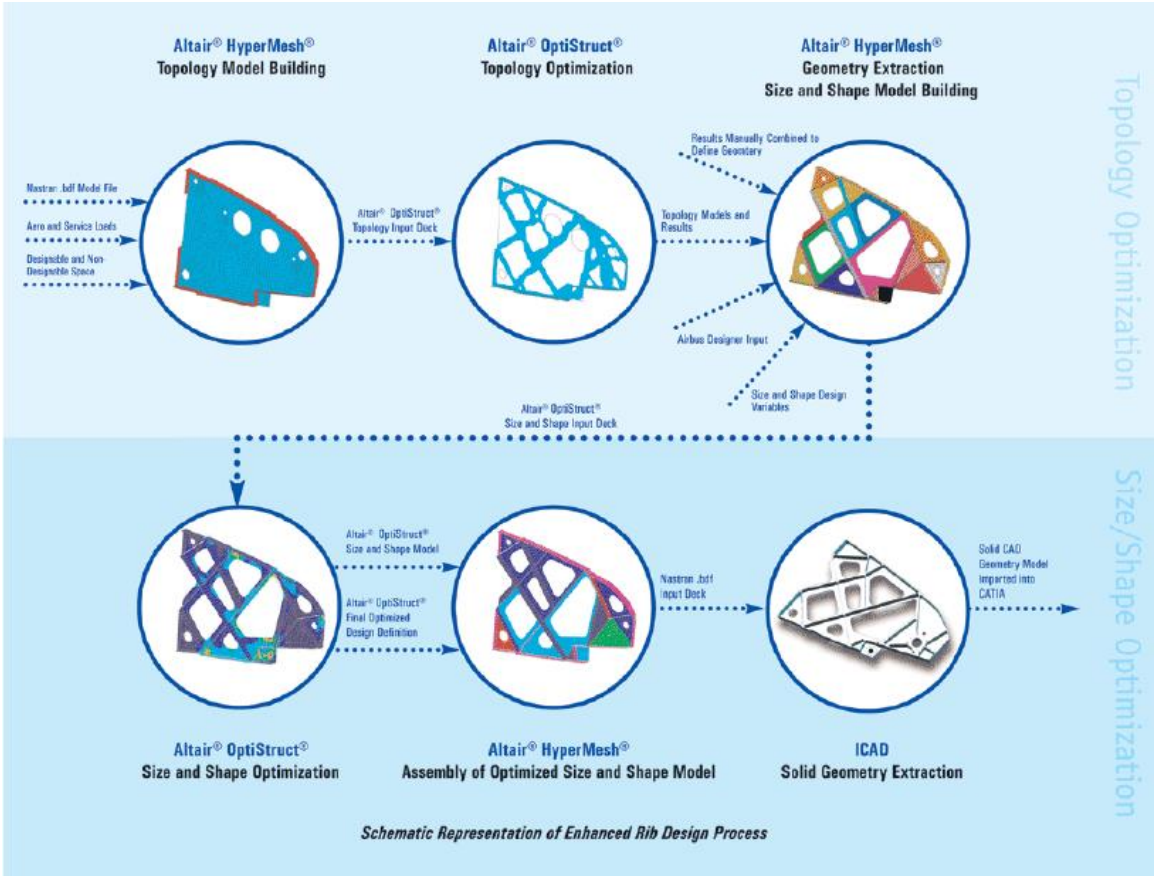


Figure 3-5: Airbus Topology, Sizing, and Shape Optmization Process [70].

Chapter Four

Aero-structural Considerations of Fore-Aft Element Connectors for a Slotted, Natural-Laminar-Flow Airfoil

Introduction

A major concern with the slotted, natural-laminar-flow (SNLF) airfoil occurs with the slotted design. While such a technology is favorable and overcomes the technical barriers that make laminar flow difficult to maintain, any separation in the laminar flow causes a decrease in the maximum lift coefficient. Several iterations of the SNLF airfoil have been introduced for various applications and rely on laminar flow across the chord with constant separation of the fore and aft elements [15, 19, 21, 33, 34, 81]. To maintain the constant separation of the elements during cruise, a slot connector must be introduced to keep the elements separated.

The introduction of these slot connectors serves two functions. The first, as stated, is to maintain the slot distance during cruise. The second is to transfer the load induced by the high-lift aft element. The aft element is not adjoined to the fuselage and is supported by the fore element. Along with keeping the elements separated and transferring the load, the design of the slot connectors must consider the impedance on the laminar flow. These connectors locally impede the laminar flow affecting the pressure distribution on the aft element leading to a decrease in the lift. Such a reduction will negate the benefits of implementing the SNLF design. It is important to consider these requirements during the design process.

To study the impact of the slot connectors' effects on the slot and determine the preferred shape and location, an investigation consisting of multiple studies was performed. The first of these studies analyzed the general shape and location of the connectors. This included preliminary structural mechanics, finite element (FE) modeling, and computation fluid dynamics (CFD). The second study refined the shape to assist in the reduction of the impedance on laminar flow and investigated the location preference inside the slot from a structural standpoint with FE analysis. The final study utilized simple structural mechanics and aerodynamics to investigate the number and size of connectors along the half-span of the aircraft. The overall goal of this investigation was to determine the final shape, size, location, and number of connectors required to support the aft element and maintain the slot distance during cruise conditions.

Study I: Location and Shape Effects

The first study in this investigation highlighted the localized study of the fore-aft element connectors including a shape and location in the slot study [82].

Technical Approach for Location and Shape Effects

The preliminary sizing of the connectors were determined using simple structural mechanics. The loading for this calculation was simplified using 2D take-off conditions and applied using a lifting line for the finite section at the quarter chord, *c/4*. To isolate the effects of the connector, a 200-inch section was detailed. For this case span percentage (η) = 0.5766 was selected as the cross-section. The cross-section was extruded to 200 inches with the connector placed in the center of the span. The connector carried the entire lifting load on the aft element for this 20-inch span. The following equation was utilized to generalize the overall lift placed on the connector. Take-off flight conditions were utilized for the preliminary design of the connectors [5, 83].

$$L_{aft} = C_{l,max} q_\infty c S_{eff} \qquad \textit{Equation 4-1}$$

Where L_{aft} is the lift force applied from the aft element, $C_{l,max}$ is maximum section lift coefficient, q_∞ is the dynamic pressure, c is the chord of the η, and S_{eff} is the effective span. The $C_{l,max}$ is based on the mean chord length and minimum speed, take-off conditions. q_∞ was calculated using:

$$q_\infty = M_\infty^2 \frac{1}{2} \gamma p_\infty \qquad \textit{Equation 4-2}$$

Where M_∞ is the Mach number for the flight condition, γ is the ratio of specific heats for air, p_∞ is the static pressure of the gas. The variables for the take-off condition are detailed in Table 4-1.

The initial shape of the connector was set to a square for simplicity. The stress placed on the connector was calculated using simple mechanics and checked against an Aluminum 6061 alloy, a common aerospace material. The properties for Al 6061 are listed in Table 4-2 [84]. The resulting connector cross-section was utilized for each of the different shapes investigated during this study for ease of comparison between the shapes. In this preliminary step, only one material was considered. Additional material consideration was factored in later in the investigation.

To provide a variety of disturbance and a thorough study, several locations in relation to the slot were considered. These included the lower slot region, the upper slot region, and outside of the slot. With the change in location several connector shapes were also investigated. These are detailed in Figure 4-1 and consist of the three subgroups established by the location of the connectors. The first group consisted of connectors A-C including the square, circle, and teardrop connectors placed near the lower slot region. These are detailed in Figure 4-1.A-C. The second group was a singular circle connector placed in the upper region of the slot as shown in Figure 4-1.D. The third group were the connectors outside of the slot detailed in Figure 4-1.E-H. This group was further broken into two subsections of small and large gap distances. The small connectors had a 3-inch

Table 4-1: Variables for take-off conditions for the S207 [5]

Variable	Take-off conditions
$C_{l,max}$	2.3
c	109.33 inches
S_{eff}	200 inches
Altitude	0 ft
M_∞	0.225
γ	1.4
p_∞	2040.9 psf

Table 4-2: Material Properties for Aluminum 6061 [84]

Variable	Value
ρ	0.0975 lb/in^3
E	10000 ksi
ν	0.33
σ_y	41000 psi

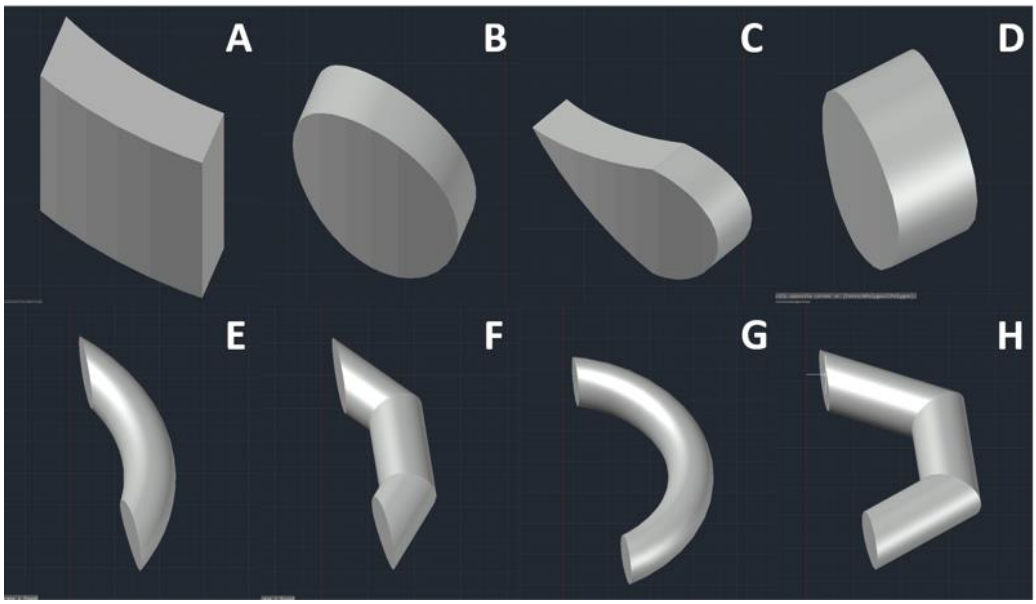


Figure 4-1: The eight connector shapes studied for shape and location effects.

gap between the bottom of the slot and the center of the connector. The large connectors had a 6-inch gap instead. The geometry of the models were developed in AutoCAD using an extruded cross-section of the S207 SNLF airfoil, $\eta = 0.5766$, with the connectors placed in the center of the span [85].

The eight connectors were then imported into Abaqus CAE to be meshed and loaded for FE analysis [44]. The root of the finite section was pinned on the fore element only, while the aft element was left floating to be supported by the connector. The fore and aft element were modeled as rigid bodies to isolate the connectors structural integrity. Figure 4-2 shows the generic cross-section generated for the FE analyses. Figure 4-3 shows the mesh generated for the connectors, using the square connector as an example. For the connectors, C3D10 elements were utilized. The connectors were constrained to the fore and aft element using a tie constraint. The loading was applied to both the fore and aft element surfaces and consisted of pressure loads generated for a 2D loading scenario of the S207 SNLF airfoil. The pressure was swept over the finite section. Table 4-3 lists the number of elements generated for each of the eight connectors.

The final aspect of the location and shape study was to investigate the impedance of the local laminar flow caused by the various connectors. CFD was utilized to investigate this and was performed with the use of COFFE by Dr. Stefanski at Oak Ridge National Laboratory [86-88]. Table 4-4 highlights the flight conditions used for the analysis, cruise conditions for the S207 SNLF airfoil were utilized [5]. The CFD mesh consisted of 14 million nodes for the finite section of the wing and was a transitional model.

Results for Location and Shape Effects

The first study was assessed with both FE structural analysis and CFD analysis. The connectors were evaluated for both stress transfer and deflection of the aft element during loading. Figure 4-4 shows a comparison of the carrying capacity of the various connectors. It is noted that the three lower slot region connectors, A-C, were capable of carrying the applied loading scenario, see Figure 4-4.A-C. The upper slot region connector, Figure 4-4.D, and the external connectors, Figure 4-4.E-H, failed to carry the load and reached yielding prior to the slot collapsing. These connectors would need to be sized or rematerialized to assist in the transfer of the loading.

Figure 4-5 illustrates the deflection of the aft element supported by each connector. The deflection of the aft element is important as it details the collapse of the slotted portion of the S207 SNLF airfoil. Similar to the stress capacity of the connectors, the lower slot region connectors, A-C, performed best. They displayed a smaller max deflection of 0.048”. This is compared to the upper slot region connector, D, resulting in 4.133” of aft element deflection prior to the connector failing. The external connectors, E-H, showed max deflections of 3.630”. The collapse of the slot with the external connectors suggests that if this approach was utilized, a larger number of external connectors would be required or that they could be assisted by internal slot spacers. However, this would disturb the local laminar flow in two aspects, compounding the loss observed in the slot.

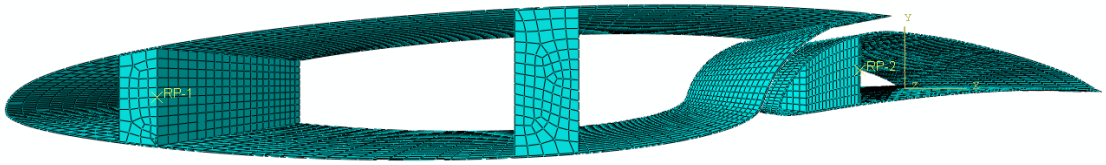


Figure 4-2: Generic Mesh cross-section for shape and location study.

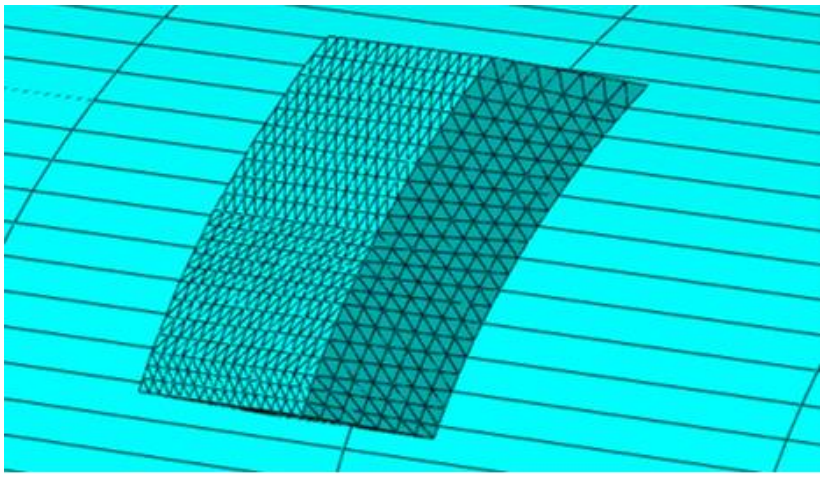


Figure 4-3: Tetrahedral mesh generation for connectors for shape and location study.

Table 4-3: Number of C3D10 elements for each Connector for shape and location study

Connector	Number of Elements
A. Square	15250
B. Circle	14524
C. Teardrop	15194
D. Upper Circle	4868
E. Small Circular	58168
F. Small Bucket	32863
G. Large Circular	36192
H. Large Bucket	16040

Table 4-4: Flight Conditions used for the CFD analyses for shape and location study

Variable	Cruise conditions
M_∞	0.7
Re	13.2 x 10^6
α	0.25°
Altitude	41,000 ft

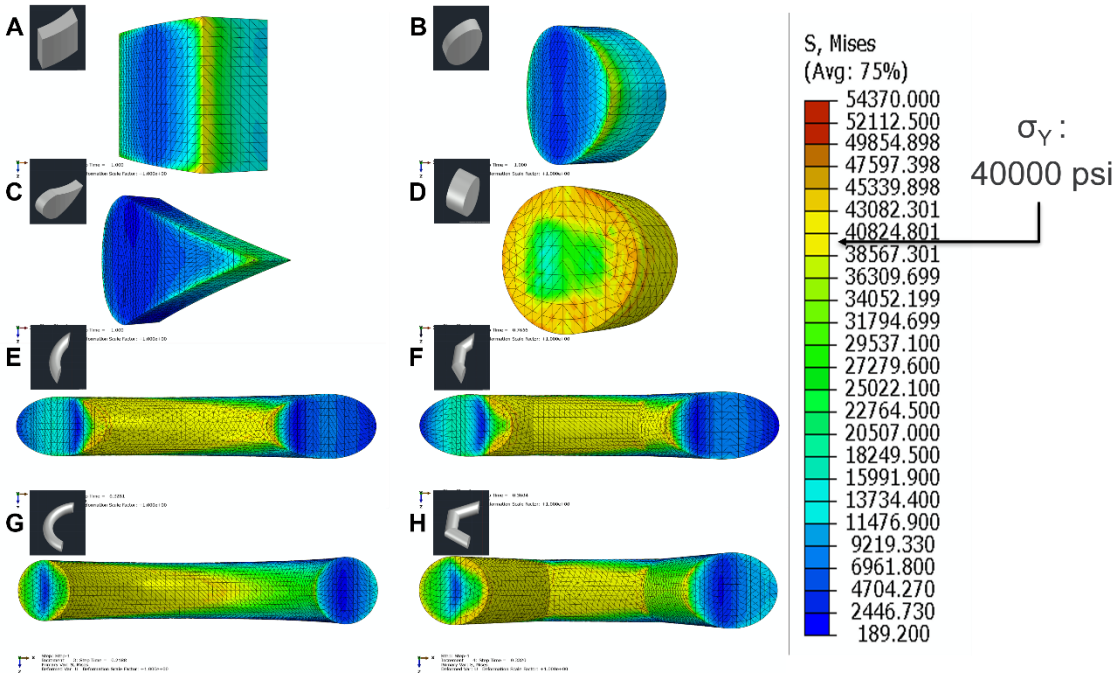


Figure 4-4: Stress buildup in the eight different connectors detailing yielding in five of the shapes.

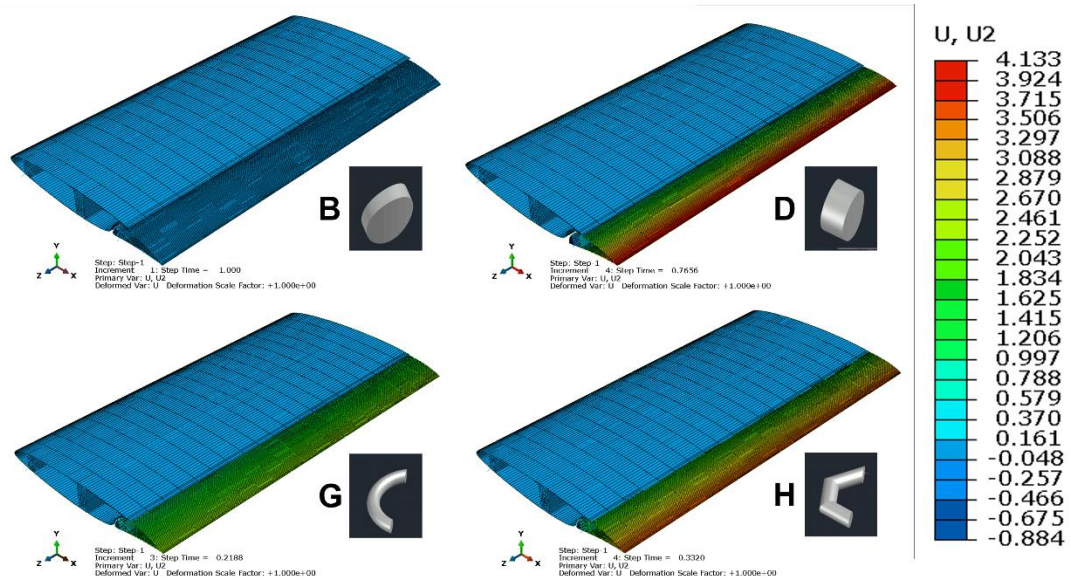


Figure 4-5: Max deflection of aft element for several of the connector shapes evaluated.

The final comparison for this study was to observe a few cases of the slot region performance with laminar flow through the slot and over the aft element. CFD was performed for three cases; a baseline section (i.e. a section without a connector), an upper slot region section (D), and an external connector (F). These were selected through internal discussion with Dr. Stefanski to save time on computational resources. A section without a connector provided a baseline to compare the others to. The upper slot region connector (D) provided an internal comparison and was selected over the other internal connectors due to its placement; an upper region connector was expected to provide less disturbance. The external connector (F) was selected to demonstrate how external connectors would disturb the flow before it enters the slot. The CFD results were visualized with eddy viscosity ratio and coefficient of friction, C_f, see Figure 4-6 and Figure 4-7 respectively. The eddy viscosity ratio details the disruption of the flow in the slot and over the aft element. A separation of flow and the introduction of a wake can be observed when compared to the clean run. C_f illustrates the separation of flow around the connectors as seen by the change in C_f on the surface of the aft element. There is also an increase in the drag coefficient, C_d, accompanied with a decrease in C_l as detailed in Table 4-5. The internal connector, D, reduces C_l by 15.89% and increases C_d by only 0.3%. While, the external connector, F, decreases C_l by 18.18% and increases C_d by 4.87%. The loss of lift is significant and informs us that the connectors need to be minimized to reduce this disturbance.

This first study indicated that the preferred location of the connectors were internally placed both with respect to the structural integrity and the aerodynamic disturbance. The lower slot region connectors, A-C, were able to transfer the stress and maintain the slot connection. The upper slot region connector, D, showed better performance when investigating the local impedance of the laminar flow. This study informed the following study by indicating that the preferred structural location was the lower slot region, while the preferred aerodynamic location was shown to be the upper slot region. The following study expanded on the structural analysis of the internal connectors with a refined transonic shape.

Study II: Transonic Size and Location Study

The second study in this investigation adjusted the shape of the slot connectors to assist in reducing the impedance on the local laminar flow shown by the loss of C_l and C_f from Study I. After deliberation, the connector was adjusted to a more streamlined shape. The slot connector was then swept for a simple size study. This included adjusting the size from 5” up to 7 ½” to determine a general sizing. This scaling was performed by adjusting a unit scale geometry in AutoCAD prior to placement within the slot. The slot connector was then placed in three locations in the slot: lower, middle, and upper regions. The connectors were extruded from the fore element’s skin to the aft element’s skin. The goal for this study was to determine the sizing and location of the slot connector that can safely transfer the load with reasonable scaling.

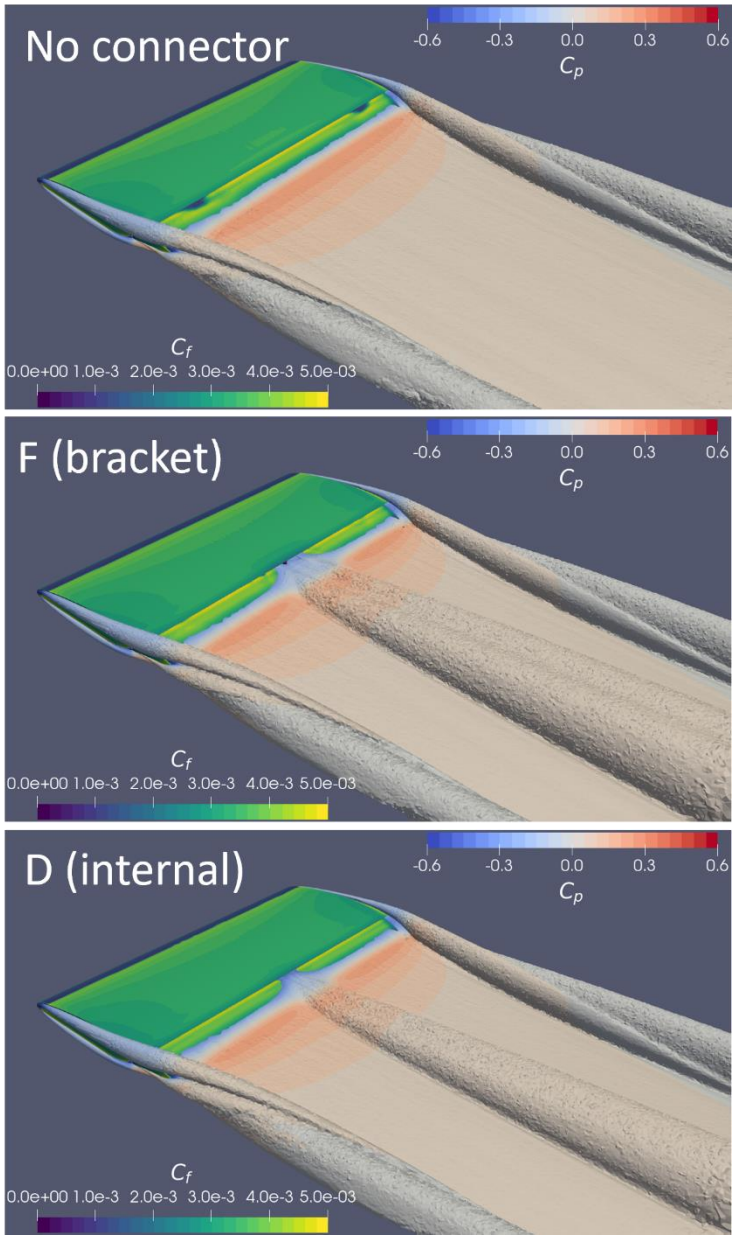


Figure 4-6: Eddy Viscosity ratio displaying the difference between a section with no connector, and external connector, and an internal connector.

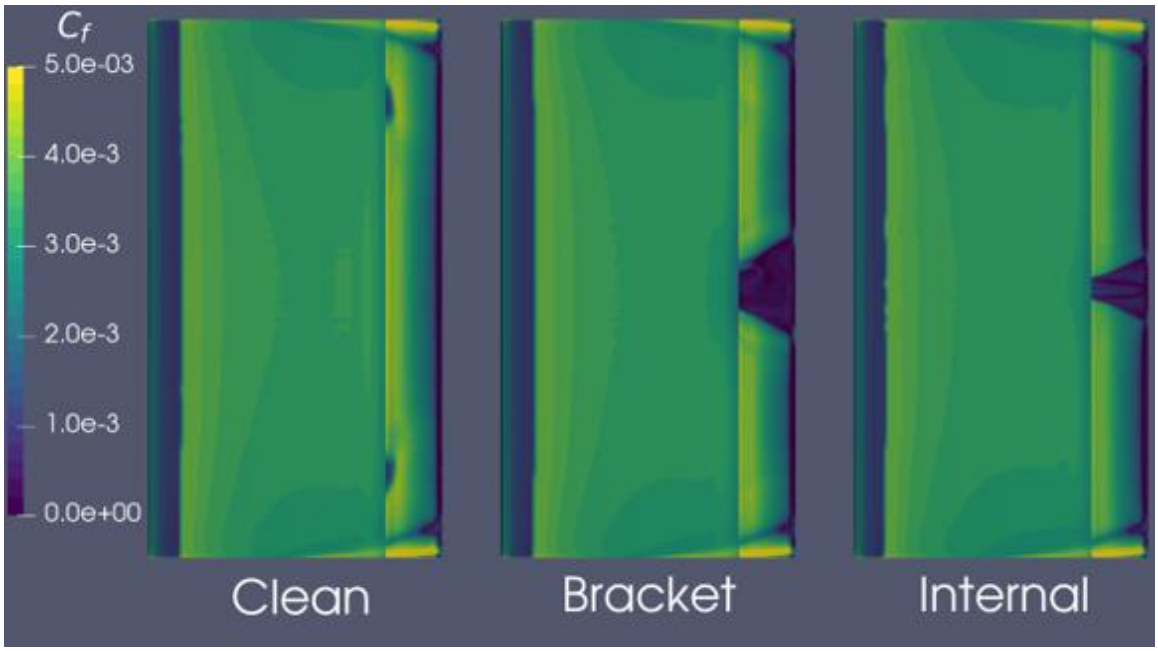


Figure 4-7: Separation of flow occurring around the connectors compared to a clean, no connector, section.

Table 4-5: Aerodynamic coefficient changes due to introduction of connectors D and F

Section Observed	**C_l**	**C_d**
Clean (no connector)	0.337000	0.031937
Internal Connector (D)	0.283450	0.032032
External Connector (F)	0.275730	0.033492

Technical Approach for Transonic Size and Location Study

The connector's shape was transformed to be more streamlined. This was chosen to alleviate the impedance to the local laminar flow. The initial outline of the connector was set to the NASA CRM.65 Blunt [89]. The CRM was adapted with XFOIL, an airfoil software, to remove the camber and mirror the upper surface to create a symmetric shape detailed in Figure 4-8 [90]. The adjusted symmetric shape provided a simplified structural design for analysis and production and ensures symmetry of flow effects caused by the connector.

An initial structural analysis informed that the slot connector required the use of Ti-6-Al-4V to minimize size and thus weight. Ti-6-Al-4V was chosen for its high strength and low density, it's properties can be seen in Table 4-6 [91]. As with Study I, Abaqus CAE was utilized for the FE solver and was used to investigate the connectors with the same 2D loading case on the 200-inch finite section. AutoCAD was utilized again to generate the models. This study was broken into two sets of analyses.
The first set of structural analyses placed the connector near the middle of the slot region. The slot connector was then scaled to evaluate the size of the connector required to transfer the 2D loading scenario. The scaling ranged from 5" to 7 ½" with increments of ¼". The fore and aft elements consisted of C3D8R elements and were set as rigid structures to isolate the slot connectors. The slot connectors were modeled with C3D10 elements and tied to the under surface of the trailing edge of the fore element and the upper surface of the leading edge of the aft element. Figure 4-9 shows the general mesh for the fore and aft element, while Figure 4-10 shows a general mesh for the different sizes of slot connectors.

The second set of structural analyses were utilized to investigate the slot connector's adjustment within the slot, and its effects on the structural stability. The setup was similar to the previous studies and modeled with AutoCAD utilizing Abaqus CAE as the FE solver. From the size study, the slot connector was detailed to 6", while the finite section of the wing remained the same at 200" and an η of 0.5766. The connector material consisted of the Ti-6Al-4V properties, Table 4-6. Figure 4-11 shows the three locations that the slot connectors were placed within the slot. For these analyses the fore and aft element remained the same as the size study with the exact mesh detailed in Figure 4-9 consisting of C3D8R elements and were set as rigid bodies. The slot connectors were modeled with C3D10 elements with a similar structure as seen in Figure 4-10. Table 4-7 lists the element count for each of the three slot connectors.

Results for Transonic Size and Location Study

The first set of FE analyses informed that the slot connectors located near the middle of the slot behaved similarly to each other after a certain size. Slot connectors smaller than 6" failed to transfer the load to the fore element. Slot connectors at 6" or above successfully transferred the loading scenario. The results illustrated a similar pattern of yielded elements and deflection of the aft element. As the slot connectors increased in size, the percentage of yielded elements decreased. This was also observed with the max deflection of the aft element.



Figure 4-8: Adjusted CRM.65 blunt shape. Camber removed and mirrored to upper surface.

Table 4-6: Material Properties for Ti-6Al-4V

Variable	Value
ρ	0.16 lb/in^3
E	16500 ksi
ν	0.342
σ_y	128000 psi

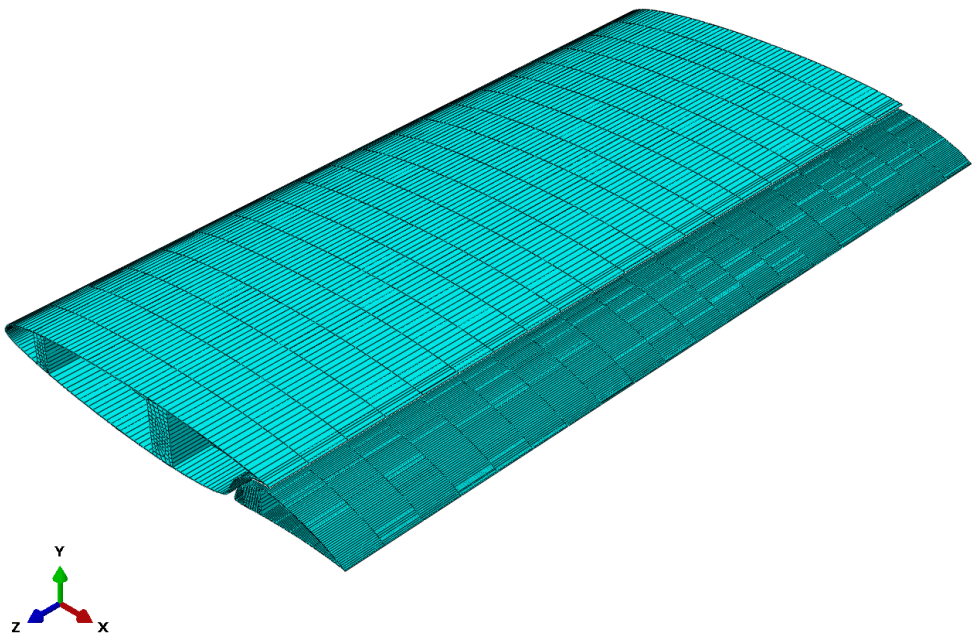


Figure 4-9: General Mesh for the Fore and Aft element finite sections utilized for several of the studies in Ch. 4.

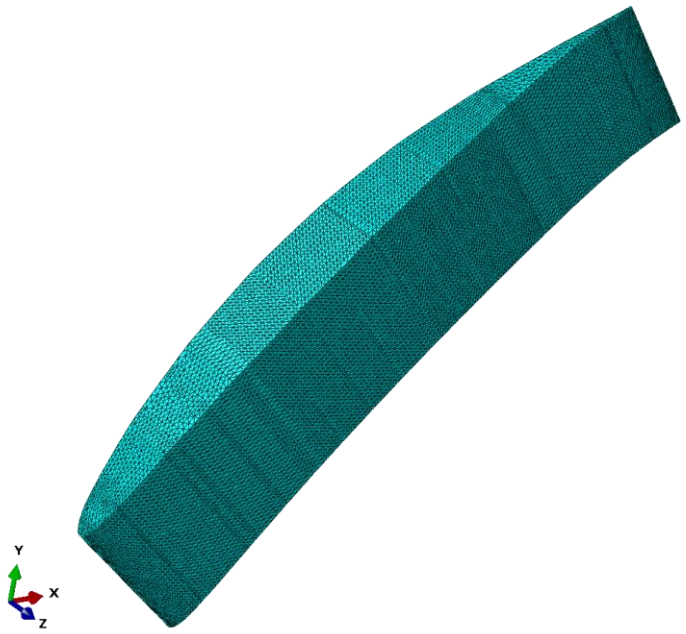


Figure 4-10: General Mesh generation for slot connector utilized for size and locations studies.

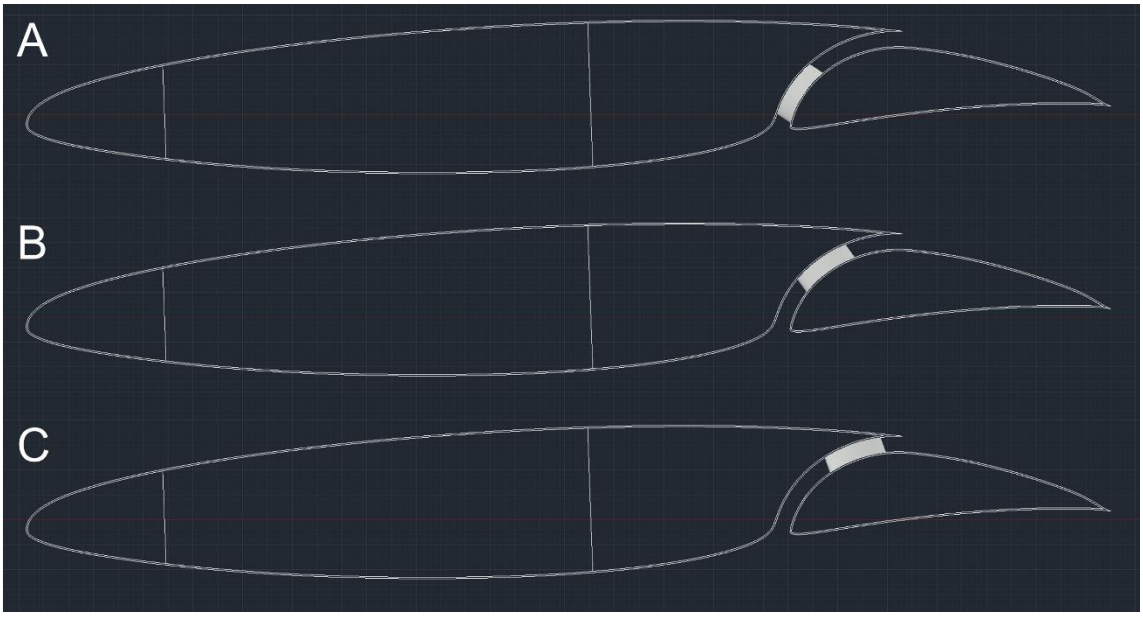


Figure 4-11: A) Slot connector placed in the lower region of the slot. B) Slot connector placed in the middle region of the slot. C) Slot connector placed in the upper region of the slot.

Table 4-7: Number of C3D10 elements comprising the slot connectors.

Location	Number of Elements
Lower	194451
Middle	201433
Upper	199474

The second set of FE analyses for this study informed of the effects of adjusting the slot connector within the slot region of the S207 SNLF airfoil. Again, the amount of yielded elements, indicating failure, and the deflection of the aft element were considered during these analyses. The lower slot connector, Figure 4-11.a, resulted in a collapse of the slot region and yielding of the connector itself. The collapse of the slot is shown in Figure 4-12. The middle and upper slot connectors displayed similar behavior in both the stress transfer and deflection of the aft element. Figure 4-14 compares the yielded elements between the middle and upper analyses. The yielded elements occurred on the surface of the slot connector on the fore element side and the author determined that they would be alleviated with more refined connection details. Similarly, Figure 4-13 details the max deflection of the aft element for both the middle and upper slot connectors. The upper slot connector observes a higher number of yielded elements in compression compared to the middle slot connector. The max deflection of the aft element is swapped with the upper region slot connector performing better. The max deflection for the upper region slot connector was 0.1269" while the middle region slot connector was 0.2402".

The slot connectors should be placed in the upper region of the slot to assist in reducing the max deflection of the aft element. As one of the main goals is to keep the aft element from deflecting, placing the slot connector in this region will assist the aft element wing structure in reducing the deflection. This will result in a slightly larger slot connector but will assist in mitigating the slot collapse and potentially reduce the weight of the wingbox of the aft element. Therefore, the connectors studied in Study III of this investigation utilize this location.

Study III: Investigation of Slot Connector Number and Size

The final study of this investigation was an investigation of the slot connector number and size for a half-span geometry required to transfer the induced aft element loading. The constraints placed on this investigation included the overall weight of the slot connectors and the aerodynamic disturbance caused by them. An analytical approach was selected for this optimization, including both the structural and aerodynamic considerations. Another consideration during the process was the study performed by Bottai et al. [45]. Bottai investigated the flutter stability of the SNLF airfoil including the connection stiffness and their effects on the modes.

Technical Approach for Slot Connector Number and Size Study

The analytical approach for this study was performed with two main constraints. These included the weight of the slot connectors and their impedance to the local laminar flow. The ability to transfer the load was checked with structural mechanics while the aerodynamic disturbance was checked with a simple drag equation on the surface of the slot connector. The weight of the slot connectors was analyzed with density and volume. The slot connectors were evenly distributed along the span of the wing.

First, a loading scenario was placed on the half-span of the wing. This was achieved by using a lifting line based on the take-off conditions for the S207 SNLF

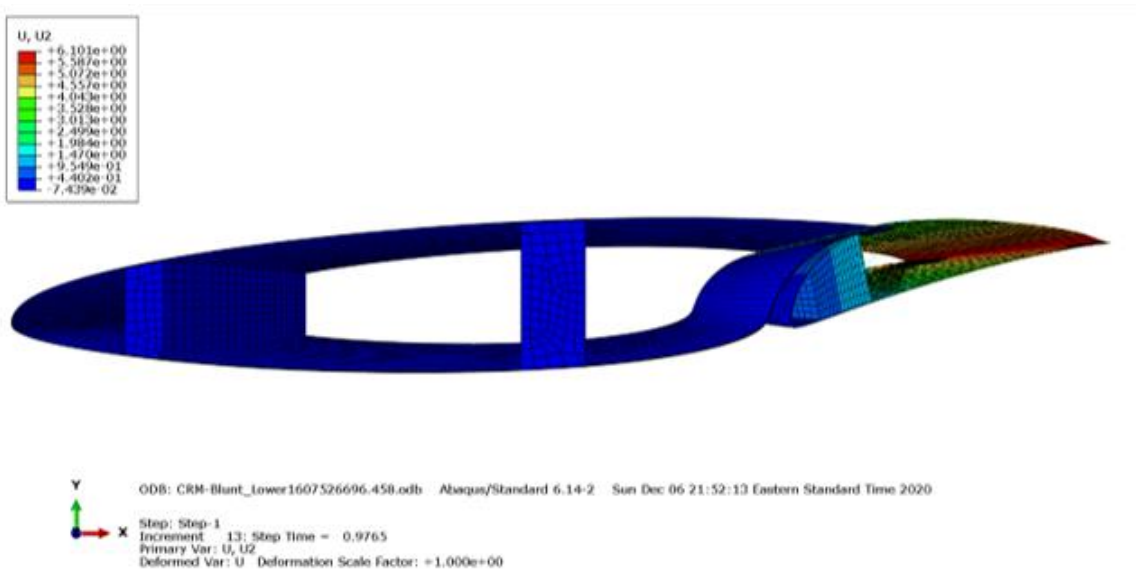


Figure 4-12: FE results detailing the collapse of the slot region when the slot connector was placed in the lower region of the slot.

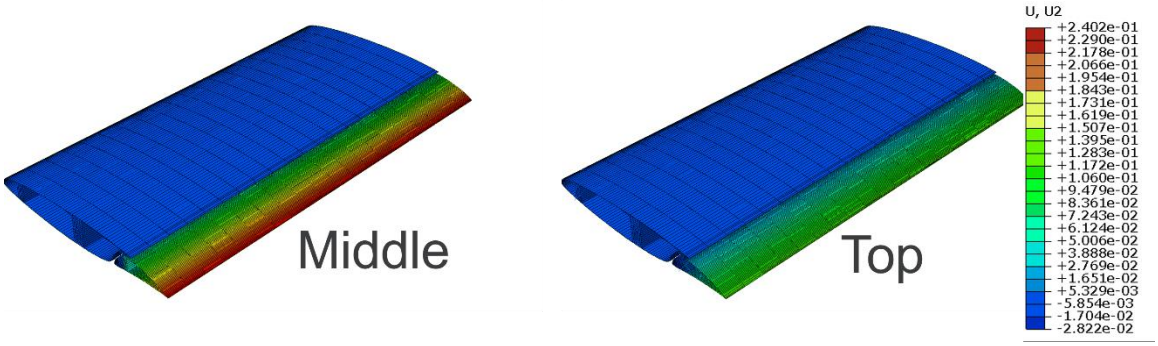


Figure 4-13: FE results for the max deflection of the aft element for the middle and upper region slot connectors.

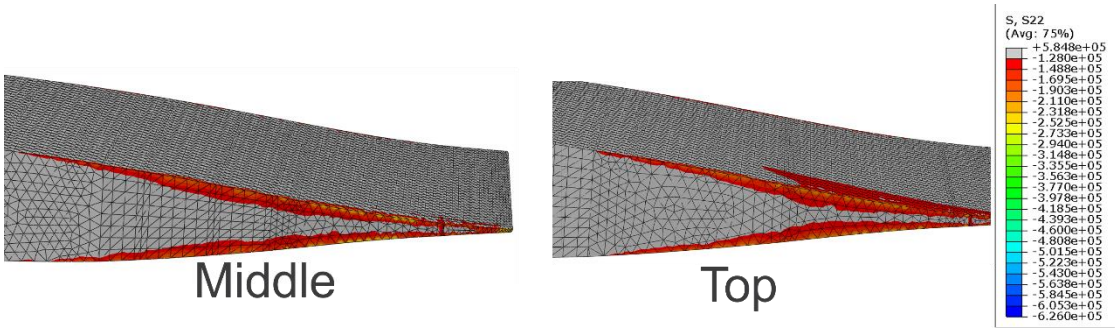


Figure 4-14: FE results comparing yielded elements in middle and upper region slot connectors.

airfoil. Table 4-1 details the flight conditions. In this case, the wing was divided into tributary areas based on the location of each slot connector with each area producing no effect on the adjacent areas. As the number of slot connectors increases the area of load they transfer decreases. As before the loading equation is:

$$L_{conn} = C_{l,max} q_{\infty} c S_{eff} \qquad \textit{Equation 4-3}$$

Where L_{conn} is the lift force applied from the aft element to an individual connector, $C_{l,max}$ is maximum section lift coefficient based on the mean chord and min speed, q_{∞} is the dynamic pressure as detailed in Equation 4-2, c is the chord of the η where the connector is placed, and S_{eff} is the effective span carried by the connector. The slot connectors were checked for their ability to carry this loading using basic structural mechanics. The below equations were utilized:

$$\sigma_y = {L_{conn}}/{A_{conn}} \qquad \textit{Equation 4-4}$$

Where σ_y is the yield limit of the material and A_{conn} is the cross-sectional area of the slot connector.

$$M_n = \sigma_y S_{conn} \qquad \textit{Equation 4-5}$$

Where M_n is the moment acting on the slot connector and S_{min} is the section modulus of the slot connector.

Many of the variables detailed above were known. The variables influenced by the slot connector's size left several unknowns. To simplify the complex shape of the slot connectors, several equations were set up to assist in scaling the shape.

The stress calculations were reworked to calculate the length and width of the connectors transonic shape. This was done with the equations below:

$$l_{conn} = \sqrt{{A_{conn}}/{0.0765}} \qquad \textit{Equation 4-6}$$

Where l_{conn} is the length of the slot connector. This equation was calculated based off a unit scale evaluation to relate the length to the area.

$$b_{conn} = 0.1133 l_{conn} \qquad \textit{Equation 4-7}$$

Where b_{conn} is the width of the slot connector. Again, this was a function determined by a unit scale evaluation. These equations were utilized to determine the connector's size due to stress requirements.

The moment acting on the slot connectors were scaled by the S_{min} required to support the moment. An equation for retrieving the l_{conn} from S_{min} was developed by scaling the connector from a unit scale, 1", up to 10" and fitting an equation. This allowed for a more simplified evaluation of the connector sizing required for any given moment.

$$l_{conn} = 2.4993 S_{conn}^{0.2717} \qquad \textit{Equation 4-8}$$

From these two approaches a maximum length and width was determined to support the load acting on the aft element during the loading scenario. Then the calculation of the weight of each connector can be determined and investigated for the first constraint.

The second constraint is the aerodynamic disturbance caused by the slot connectors. A very simple approach using the drag equation below was utilized:

$$D_{conn} = C_D q_\infty A_{frontal} \qquad \textit{Equation 4-9}$$

Where D_{conn} is the drag acting on the slot connector, C_D is the drag coefficient, and $A_{frontal}$ is the frontal area of the slot connector. C_D was set to 0.045 and was set to match the airfoil detailed by NASA [92].

Three materials were investigated during the investigation. This included Al 6061, A36 steel, and Ti-6Al-4V. Al 6061 was selected for its common place in aerospace. A36 steel was selected due to the author's familiarity and to provide a contrast to common aerospace materials. Ti-6Al-4V was selected to provide a better option in regard to strength per density, albeit a more expensive option. Table 4-8 details the mechanical properties of these materials [84, 91, 93].

Results for Transonic Number and Size Study

The results of this investigation were categorized by two constraints. These included the weight of the connectors and the average drag of the connectors. The constraints were chosen to match the overall goals of the dissertation. For this study, the distance between the connectors were constant and the upper limit to the number of connectors was set to match findings from Bottai et al. at nine connectors needed for flutter stability [45].

Results for the weight versus the number of connectors is provided in Figure 4-15. It can be observed that as the number of connectors along the half-span increases the

Table 4-8: Material Properties for Al 6061, A36, and Ti-6Al-4V

Variable	Al 6061	A36	Ti-6Al-4V
ρ	0.0975 lb/in^3	0.284 lb/in^3	0.16 lb/in^3
E	10000 ksi	29000 ksi	16500 ksi
ν	0.33	0.26	0.342
σ_y	41000 psi	36000 psi	128000 psi

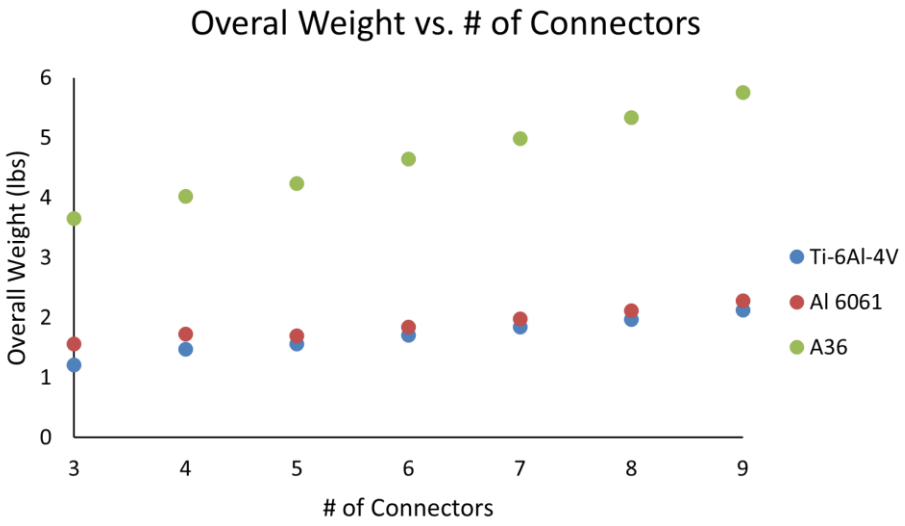


Figure 4-15: Weight of various connector numbers required to transfer flight loads from aft element to fore element.

overall weight of the connectors increases as well. No taper to the increase in weight is detailed as you increase the number of connectors. A36 steel proved to be the worst material type due to its increased density compared to Al 6061 and Ti-6Al-4V. While the general size of the connector would decrease, the density of A36 negated this benefit. There was a slight difference between Al 6061 and Ti-6Al-4V. The Ti-6Al-4V material would be a more expensive option but resulted in smaller connectors compared to the Al 6061. From the weight results, the Ti-6Al-4V was the preferred material for its decrease in overall connector sizes and lesser increase in the weight of the combined connectors.

The aerodynamics for the connectors was evaluated with drag as shown in Figure 4-16. Here it is observed that the average drag along the surface of an individual slot connector decreases as the number of connectors increases. This makes sense as the drag is a function of the frontal area, which decreases as the connectors become smaller. The benefits of adding connectors slow as the number increases as observed by the decay after seven connectors and the similarity between eight and nine connectors. Unlike the previous constraint, the A36 steel performed better than the Al 6061 due to the connectors being smaller. The Ti-6Al-4V outperforms the other two materials with this constraint as well as maintaining a gap between the average drag even as the number of connectors increases.

From these two constraints it is shown that the Ti-6Al-4V connectors are preferred with their lower increase in overall weight and decrease to the impedance of the local laminar flow inside the slot. While the material selection for the connectors was straight forward, the number of connectors remained a challenge. This simplistic approach to the aerodynamics showed that smaller connectors along the half-span would result in less drag on the surface of these connectors, this in turn will result in less local impedance. However, the overall weight of the connectors would suffer as more connectors are added. Another study performed by Bottai et al. investigated the number of connections along the half-span for flutter stability [45]. Bottai highlighted that nine connections between the fore and aft element connectors were required to support the flutter stability in different modes. Therefore, moving forward into the aft element topology, the number of connectors was defaulted to support this conclusion. This does produce an increased disturbance to the laminar flow and increases the overall weight of the connectors but ensures that the aft element spans are short enough to maintain control. The resulting length and locations of the Ti-Al-4V slot connectors are explained in Table 4-9.

Conclusions and Current Work

The previous studies included in this investigation along with the flutter stability by Bottai dictated the number of connectors to be utilized for the half-span topology optimization. The studies in this dissertation informed the topology optimization what the individual size and shape of the slot connectors should be. Bottai instructed the minimum number of slot connectors required. This investigation detailed internal slot connectors' performance compared to external slot connectors in both structural and aerodynamic

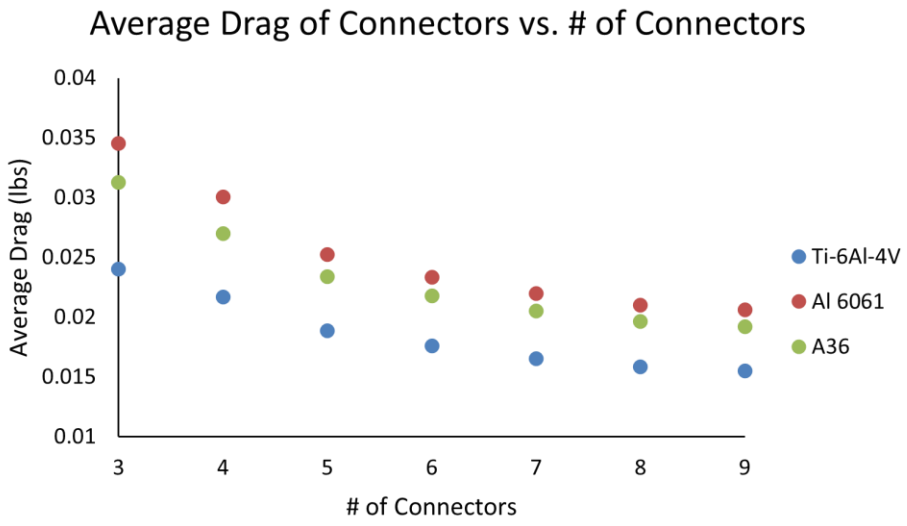


Figure 4-16: Drag acting on various connector numbers showing impedance of local laminar flow in the slot.

Table 4-9: Slot connector size and locations.

η	Length of Ti-6Al-4V Slot Connectors (in)
0.0180	4.43
0.1250	5.30
0.2500	5.22
0.3750	5.14
0.5000	5.06
0.6250	4.81
0.7500	4.29
0.8750	3.99
0.9750	2.58

aspects. It was also observed that the slot connector assisted the goal of maintaining the slot distance if it was placed near the upper region of the slot. The final aspect of this investigation showed that as the number of connectors along the half-span increased the impedance to local laminar flow decreases but the overall weight penalty increases. The following chapter investigates the aft element topology optimization for the S207 SNLF airfoil and utilizes the connectors from this investigation.

Chapter Five

Topology Optimization of the AFT Element

Introduction

The aft element of the S207 slotted, natural-laminar-flow (SNLF) airfoil is a crucial part of the design. This element produces a considerable amount of lift for the airfoil during cruise assisting in the aerodynamic performance. The aft element requires proper support to ensure the outer mold line (OML) does not change significantly during cruise allowing for the laminar flow to be achieved and to meet the aerodynamic goals of the project. The desired deflection of the aft element was expressed to be below a tenth of an inch. The aft element was detailed as a 'floating' element. Thus, no root support is provided by the fuselage. The resulting scenario is that the aft element wants to lift into the fore element which bends due to its rooted structure. The internal structure of the aft element is required to essentially fix the aft element in place relative to the fore element during cruise conditions maintaining the slot distance and providing the benefits.

The goal of this investigation is to produce an aft element structure that reliably transfers the load to the connectors that were determined by the previous investigation, while ensuring minimal deflection during cruise conditions. The overall weight of the structure was taken into consideration as well. Topology optimization was utilized to achieve this goal. Topology optimization, detailed in Ch. 3.3: Topology Optimization, is a mathematical method that optimizes material distribution within a given design space, for a given set of loads, boundary conditions, and constraints with the goal of maximizing the performance of the system [46]. Topology optimization is a continually evolving approach that can assist design processes. In this case, the use of topology optimization can help the overall goal of the S207 SNLF airfoil's performance goal by minimizing the weight penalty required to support the high-lift aft element.

Topology optimization results in an optimized distribution of material inside the design space but fails to incorporate manufacturability. As such, the final topology optimization needs to be evaluated for ease of production and cost. The overall goal of this investigation is to derive the optimized material distribution across the half-span of the S207 aircraft wing to support cruise flight conditions and minimize the weight and displacement of the aft element supported by fore-aft element connectors.

Technical Approach

AutoCAD was utilized to generate the half-span based on 2D unit-scale coordinates that were scaled, displaced, and rotated according to several η positions provided [85]. The resulting half-span was then lofted together and checked for appropriate fidelity before translating to the FE solver. Figure 5-1 provides a reference image of the half-span wing detailed with AutoCAD. The aft element is to be joined to the fore element by the nine evenly spaced slot connectors seen on upper surface of the aft element. The locations and sizes of the slot connectors are expressed in Table 4-9. The tip region, last 10% of the half-span wing, is subjected to increased twist. Table 5-1

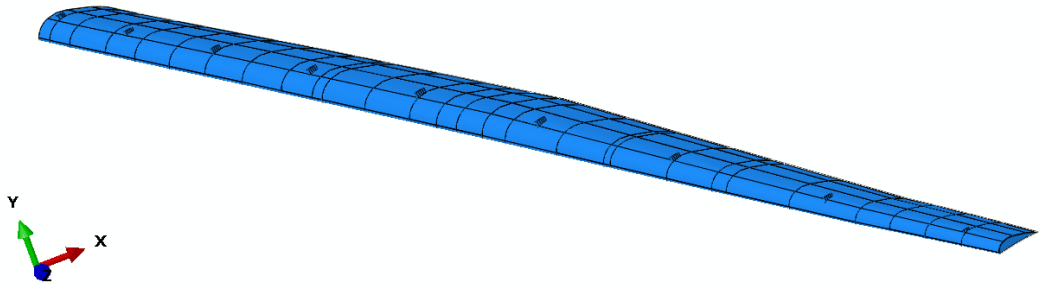


Figure 5-1: CAD model detailing the half-span wing utilized for aft element topology.

Table 5-1: Twist angle provided for various span locations for the S207 SNLF airfoil

Station	Span %	η	Chord (in)	Twist Angle (°)
0 (root)	0	0.0000	124.5800	0.0
1	5	0.0500	123.2572	0.0
2	15	0.1500	120.6115	-0.5
3	30	0.3000	116.6431	-1.3
4	45	0.4500	112.6746	-1.8
5	57.66	0.5776	109.3525	-2.1
6	70	0.7000	90.04085	-2.1
7	80	0.8000	74.40992	-2.2
8	90	0.9000	58.77898	-2.6
9 (tip)	100	1.0000	43.14804	-5.8

details the twist degrees of the half-span wing for varying η. It is expected that the twisted tip will be reduced in further adjustments of the half-span geometry. For this investigation the twist was kept as stated. Further information about the S207 η used to produce the model are detailed in Table 5-2. The detailing of the S207 SNLF airfoil was provided in three aspects. The first was a unit scale 2D geometry as shown in Figure 5-2 developed by Somers and Airfoil, Inc. [5]. The unit coordinates were adjusted based on η locations defined by a taper and twist. EI/GJ restraints and twist locations provided an initial amount of η, the author filled in the sections between these locations to provide more discretization along the half-span to assist in the CAD process.

Abaqus CAE was selected as the FE solver [44]. Abaqus allowed for an initial evaluation of the model's validity and supports topology optimization with a simple interface. The fore element was left absent from this model. The connectors were modeled with the sizing and location from the weight and drag study performed in Ch.4: Results for Transonic Number and Size Study with the number dictated by Bottai et al.'s flutter stability [45]. Nine connectors spaced evenly across the half-span wing were set to support the aft element. The connectors were placed near the upper slot region of the airfoil accounting for twist of the half-span wing. The nine connectors can be seen in Figure 5-1. The connectors were materialled with Ti-6Al-4V, properties shown in Table 4-6. C3D8R elements were used to model the connectors. The fore side of these connectors were fixed to simulate their connections to the fore element and consist of the model's boundary conditions. The goal was to fixate the aft element with respect to the fore element.

The aft element is modeled initially with Al 6061, Table 4-2. The aft element is modeled in two parts. The first of these is the skin of the element. This part was set by the OML generated by the 2D coordinates of the various η. The inside of the skin was set 0.15" perpendicular to any location along the OML. The skin thickness was determined by setting the gauge to match the minimum specified skin gauge for the Boeing SUGAR HIGH report [94]. The skin thickness was maintained across the half-span wing to allow for the topology optimization to inform where increased material is required. The skin part of the aft element is the loaded region and kept frozen during the optimization as the topology optimizer requires material for the pressure to be transmitted. Figure 5-3 details the mesh generation for the skin region and consist of 383,926 elements. The second part of the aft element was the interior region utilized for the design space of the topology optimization. This was modeled by using the IML of the skin part and creating a solid part. The part is shown in Figure 5-4 and consisted of 1,056,786 C3D8R elements. The OML of the skin part was constrained to the aft side of the slot connectors with tie constraints. The IML of the skin part was also constrained to the surface of the interior part with a tie constraint.

The loading scenario for the topology optimization was set to the cruise condition of the S207 SNLF airfoil. This was selected as the displacement control of the aft element was expressed to be crucial in this flight condition. The final material distribution will be required to be checked for other flight conditions but can be assisted by other control surfaces to meet requirements. The loading provided for cruise conditions consisted of 2D η cross-sectional C_p plots generated by Dr. Stefanski at ORNL. Figure 5-5 illustrates

Table 5-2: ETA information for the S207 SNLF Airfoil utilized for generation of aft element topology. It should be noted that the numbers below have been rounded for simplicity of showing.

η	Span (in)	Chord (in)	Twist Angle (°)
0.0000	0.0000	124.5800	0.00000
0.0180	17.5469	124.1038	0.00000
0.0500	48.7415	123.2572	0.00000
0.1060	103.3320	121.7756	-0.28000
0.1500	146.2245	120.6115	-0.50000
0.2000	194.9660	119.2887	-0.76667
0.2500	243.7075	117.9659	-1.03333
0.3000	292.4490	116.6431	-1.30000
0.3500	341.1905	115.3203	-1.46667
0.3880	378.2340	114.3149	-1.59333
0.4000	389.9320	113.9974	-1.63333
0.4500	438.6735	112.6746	-1.80000
0.5000	487.4150	111.3518	-1.91848
0.5290	515.6851	110.5846	-1.98720
0.5500	536.1565	110.0290	-2.03697
0.5766	562.0870	109.3252	-2.10000
0.6000	584.8980	105.6718	-2.10000
0.6500	633.6395	97.8563	-2.10000
0.6940	676.5320	90.9787	-2.10000
0.7000	682.3810	90.0409	-2.10000
0.7500	731.1225	82.2254	-2.15243
0.7880	768.1660	76.2856	-2.18800
0.8000	779.8640	74.4099	-2.20000
0.8500	828.6055	66.5945	-2.40000
0.9000	877.3470	58.7790	-2.60000
0.9250	901.7178	54.8713	-3.40000
0.9500	926.0885	50.9635	-4.20000
0.9750	950.4593	47.0558	-5.00000
1.0000	974.8300	43.1480	-5.80000

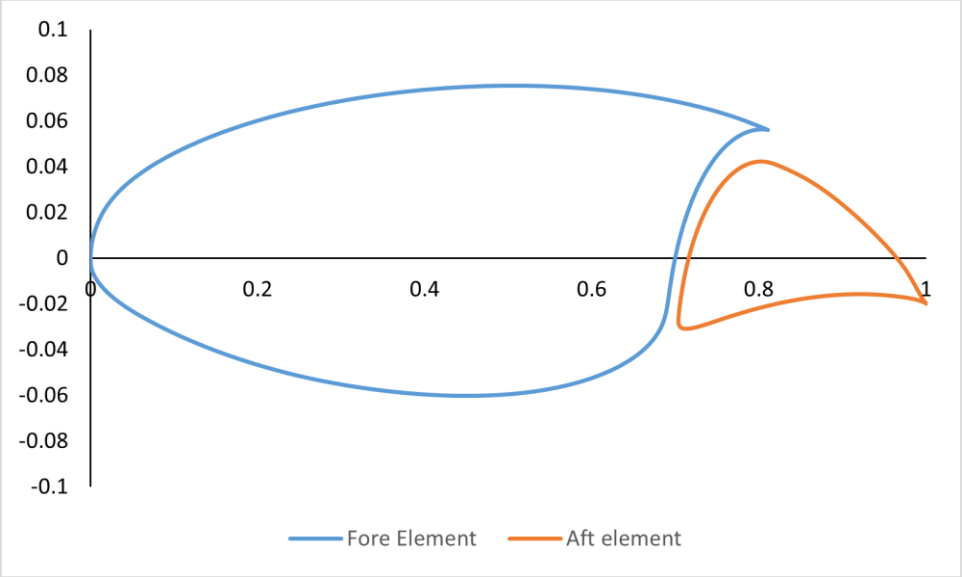


Figure 5-2: Unit shape of the S207 SNLF airfoil developed by Somers [5].

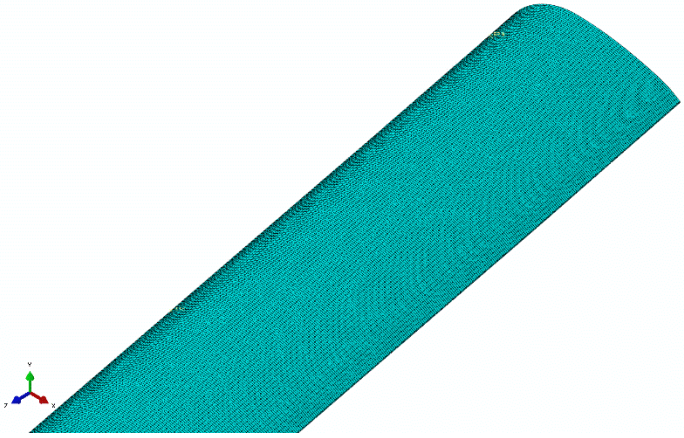


Figure 5-3: Mesh for aft element skin with C3D8R elements.

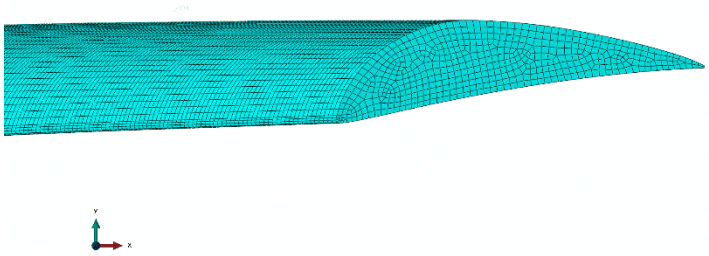


Figure 5-4: Mesh for design region of the aft element using C3D8R elements.

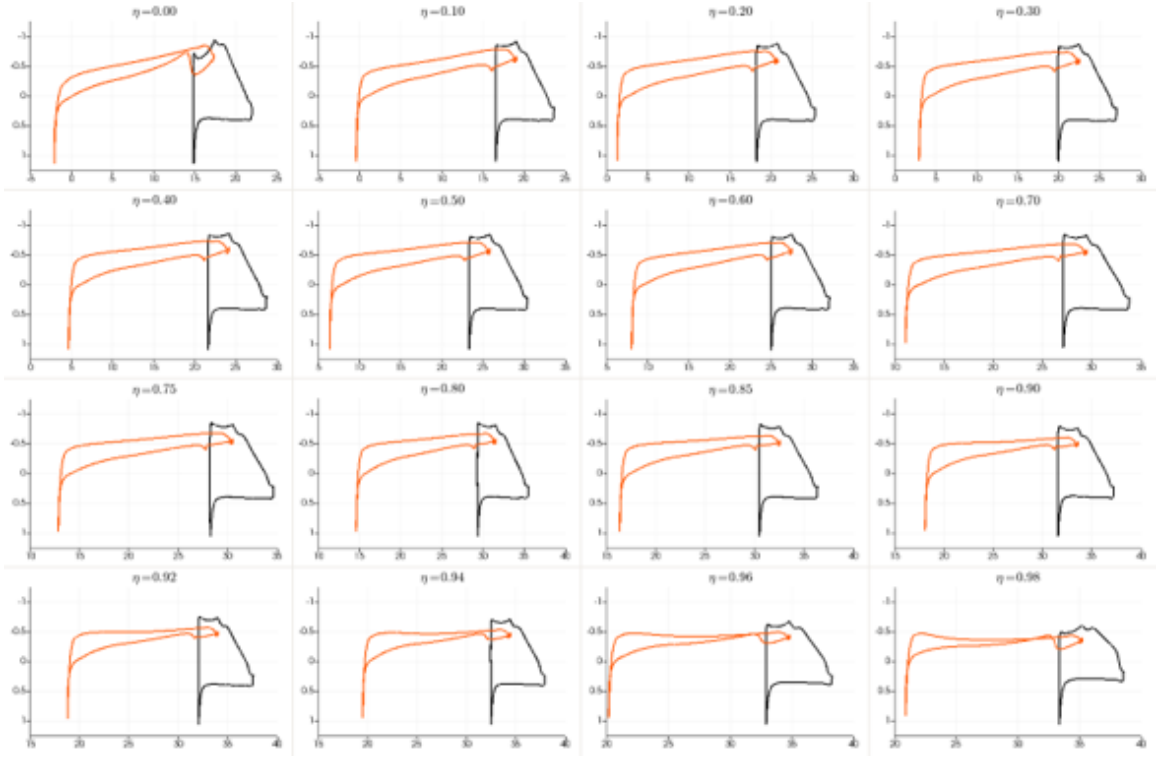


Figure 5-5: Cp plots for the S207 SNLF airfoil for various span locations.

the various η C_p plots utilized to load the aft element in the cruise condition. ImageJ was used to pull the C_p values along the upper and lower surface of the η [95]. The flight conditions for the cruise condition are listed in Table 5-3. The change in pressure on the surface of the aft element, Δp, was calculated with the equation below:

$$\Delta p = \frac{1}{2}\rho_\infty V_\infty^2 C_p \qquad \textit{Equation 5-1}$$

Where ρ_∞ is the free stream fluid density of air and V_∞ is the freestream velocity of air during the cruise condition. A factor of safety of 1.5 was applied to the loading scenario to meet FAA requirements. The pressure between η was set to the higher value on either side. The resulting pressure was applied to the OML of the aft element skin part as detailed in Figure 5-6.

Topology optimization of the interior part of the aft element was controlled by three aspects. The object function of the optimization was the strain energy of the design region, the interior part. Two constraints were placed on the topology optimization. The first constraint was a percentage of the overall material for the design region. This was set to ≤ 10% of the material amount. This value can be adjusted in future iterations. The second constraint was the displacement of the aft element's skin. Abaqus CAE limits the number of nodes that can be selected for displacement control. This required that less than 500 nodes be set for the constraint. Several nodes at each midspan between connectors were selected to make the node set for this constraint. Nodes along the leading edge and upper surface of the OML were included. Internal discussion indicated a desire for little to no displacement of the aft element during cruise to ensure the S207 SNLF airfoil maintains laminar flow. To meet this expectation the nodes were limited to 0.1" of displacement and will result in a significant amount of material being added.

Results and Discussion

The topology optimization of the aft element was evaluated for material distribution within the aft element. The results below are detailed with the provided loading scenario and displacement control of the slot region. Figure 5-7 demonstrates the half-span material distribution of the design region, the interior part. It should be noted that for the following figures, the skin part was removed from the graphic to allow adequate viewing of the design region. The material distribution along the half-span behaves in two distinct manners. The region near the root resulted in a distribution similar to ribs located underneath the slot connectors. Figure 5-8 illustrates a cut of the half-span detailing two of the connector regions. It can be observed that material is built-up underneath the connectors. This is expanded upon with Figure 5-9 where a trailing edge view is shown. The material is distributed underneath the connector and the skin is thickened along the span away from the connection point. The second region is the distribution near the tip. Figure 5-10 and Figure 5-11 illustrate the design region material

Table 5-3: Cruise flight conditions for the S207 SNLF airfoil

Variable	Cruise conditions
M_∞	0.7
Re	13.2 x 10^6
α	0.25°
Altitude	41,000 ft

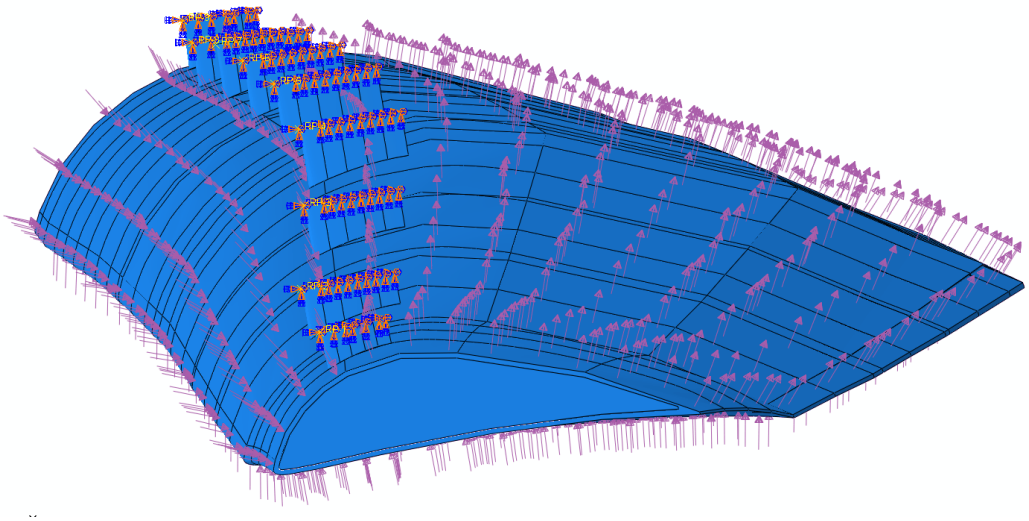


Figure 5-6: Pressure distribution on the aft element for utilized for the topology optimization.

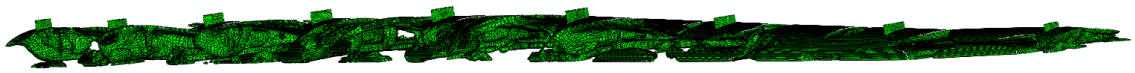


Figure 5-7: Half-span wing material distribution informed by topology optimization of the aft element with displacement control.

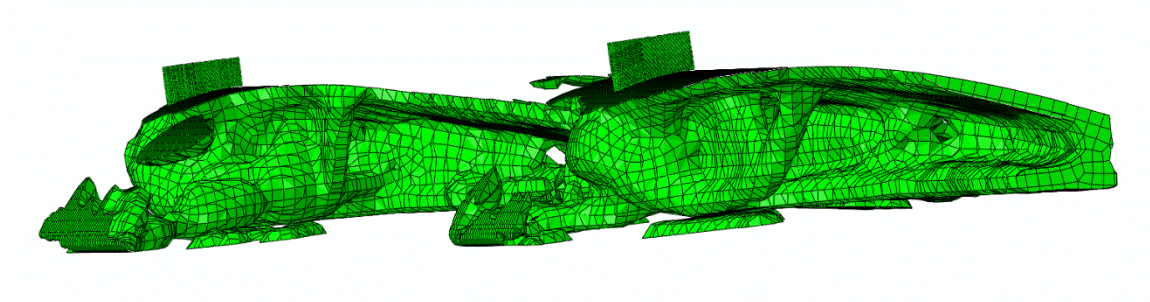


Figure 5-8: Material distribution underneath the connectors illustrating the ribs.

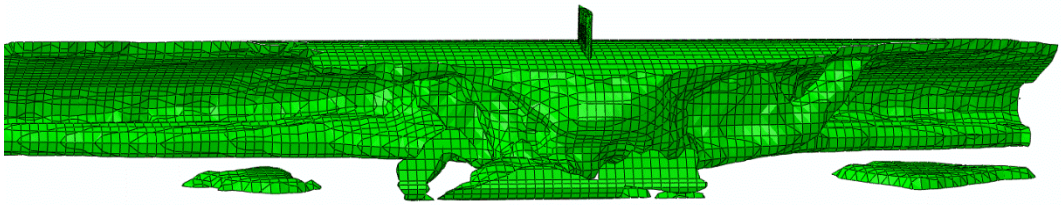


Figure 5-9: Trailing edge view of the material distribution underneath a connection and along the span between two connection points.

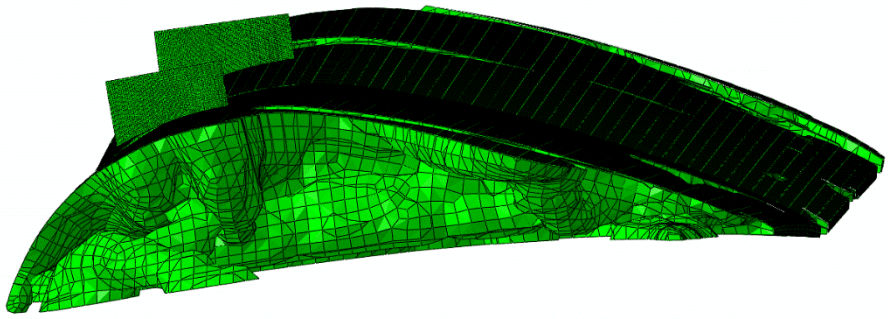


Figure 5-10: Material distribution of the tip region for the aft element under topology optimization.

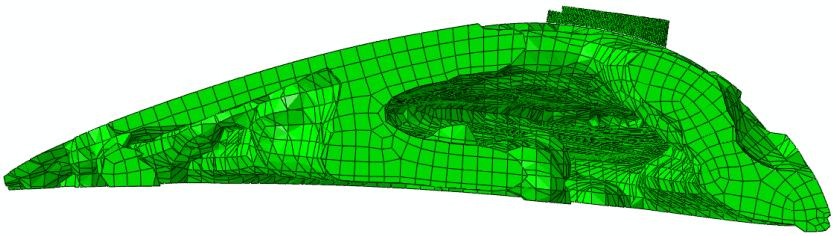


Figure 5-11: Interior view of tip region of the aft element demonstrating increased skin gauge across the span.

distribution for this region. As the span approaches the far tip, Figure 5-10, the skin isn't sufficient to transfer the load and a large distribution of material is required. Figure 5-11 shows the material distribution looking towards the tip and shows a hollow section indicating that the skin is being thickened to support and transfer the load. This topology optimization demonstrated that an optimal transfer of the load could be achieved with ribs at the connection points and stiffened material between those connections, i.e. stiffer skin or stringers. An important take away from this optimization is that no definitive spar was indicated from the material distribution. The removal of a spar inside the design region could potentially assist in reducing the overall weight contribution of the aft element and assist in reducing fuel consumption.

To further investigate the topology of the aft element an important comparison between the previous setup and a displacement-relaxed setup was performed. This allowed for an investigation on the effect of the deflection constraint on the aft wingbox structure. Figure 5-12 illustrates the material distribution for the half-span wing for this iteration. A much-reduced material distribution is observed with this iteration. A large concentration of material is observed underneath the connection points similar to the displacement-controlled iteration. The root spars can be seen in Figure 5-13 and show that the main distribution of material in the spars is distributed along the upper surface of the IML. There is no material distribution along the span locations between the connection points.

The comparison of these two iterations highlights two significant concepts. The first is that ribs are desired underneath each connection point to assist in transfer of the load to the connectors. Both iterations detailed an increased material distribution underneath each individual connector. The second concept corresponds to the displacement constraint required to maintain the slot distance. Comparing the material distribution between the connections for the two iterations demonstrates this concept. Figure 5-14 and Figure 5-15 show the deformation of the upper skin for the displacement control and non-displacement control iterations respectively. The max deflection of the upper surface with displacement-control is maintained to around ½" while the non-displacement controlled upper surface reaches over 2" of deformation. This informs that the increased material distribution in the form of skin thickness between the connections greatly assists in reducing the displacement of the aft element and is needed to meet deflection goals.

Conclusions and Manufacturability

The results from the topology optimization of the aft element indicated that the preferred material distribution requires the implementation of ribs underneath each connector location. The displacement-controlled iteration also highlighted the need to increase the stiffness between the connections to assist in maintaining the slot separation during cruise conditions. The traditional spar and rib design seen in aircraft can be reduced to a simpler design consisting of ribs and stringers for the aft element of this S207 SNLF airfoil.



Figure 5-12: Half-span wing material distribution informed by topology optimization of the aft element without displacement control.

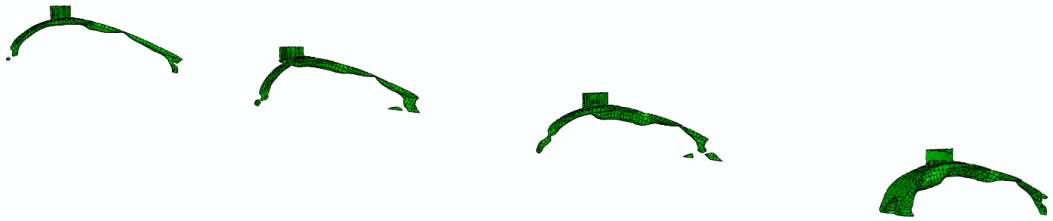


Figure 5-13: Material distribution underneath the connections without displacement control.

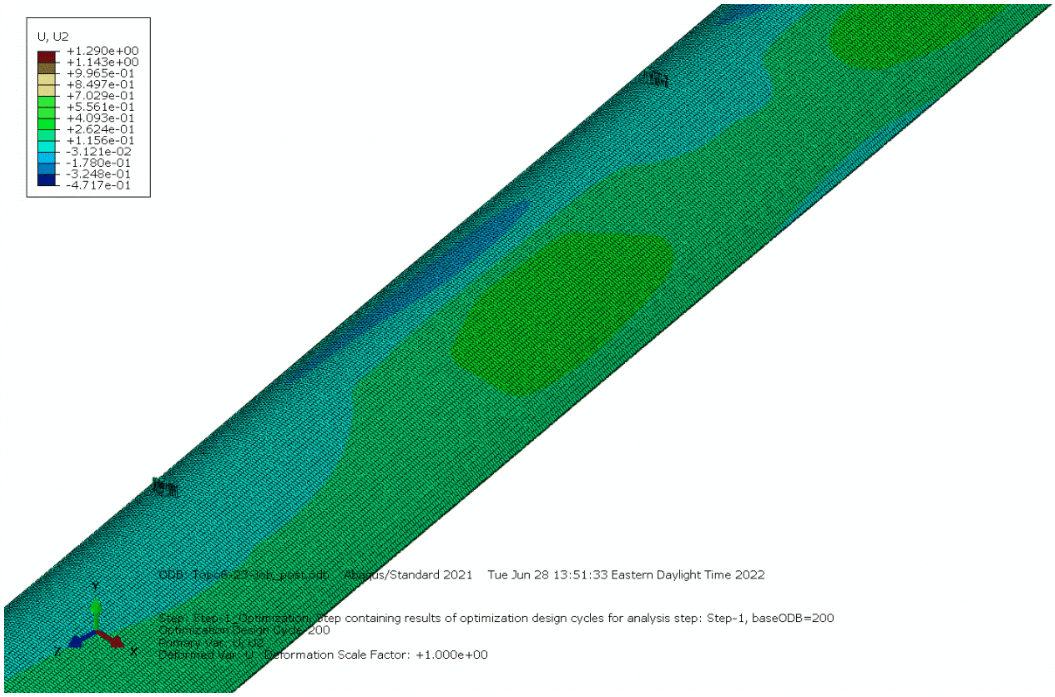


Figure 5-14: Deformation of the upper skin region between two connectors for the topology optimization with displacement control.

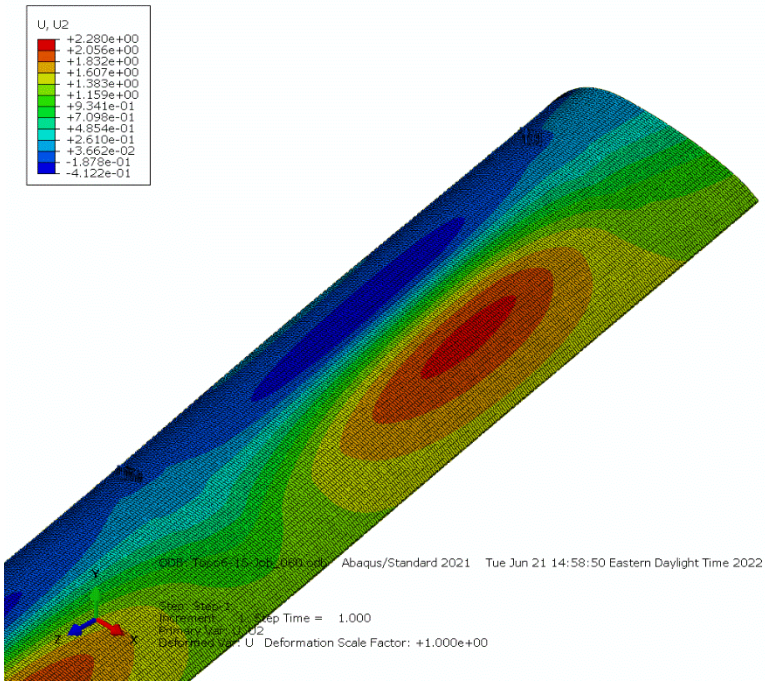


Figure 5-15: Deformation of the upper skin region between two connectors for the topology optimization without displacement control.

Chapter Six

Full Half-Span Wing Structural Demonstration

Introduction

This chapter focuses on combining the previous results to produce a demonstration of the half-span geometry including the fore and aft wingbox structure with the slot connectors. Chapter Four: Aero-structural Considerations of Fore-Aft Element Connectors for a Slotted, Natural-Laminar-Flow Airfoil resulted in nine slot connectors along the half-span with their sizes and locations shown in Table 4-9. Chapter Five: Topology Optimization of the AFT Element informed the half-span demonstration on the aft element structural components. The material distribution of the aft element led to the half-span aft element wingbox consisting of ribs, skin, and stringers without the use of a spar. This demonstration's purpose is to describe how the S207 slotted, natural-laminar-flow (SNLF) airfoil behaves with previous considerations on a global scale with cruise loading conditions. Initial sizing of the wing structural components was also performed.

Technical Approach

The demonstration geometry was modeled with AutoCAD with the same twist and η definitions that were used to setup the topology optimization in Chapter Five, see Table 5-2 [85]. This allowed for enough discretization along the span to reduce geometric errors from lofting. The resulting fore and aft elements were joined by nine slot connectors detailed in Table 4-9. These were sliced along the surface of the fore and aft element to produce flush faces. Geometric illustrations of the fore element, aft element, and slot connectors can be seen in Figure 6-1, Figure 6-2, and Figure 6-3 respectively.

The material selection for the half-span demonstration consisted of two materials. The first is the Ti-6Al-4V described in Table 4-8. Ti-6Al-4V was kept for the slot connector material definition. This is consistent with previous studies that indicated the Ti-6Al-4V slot connectors performed better than the other observed material selections, see Chapter Four: Aero-structural Considerations of Fore-Aft Element Connectors for a Slotted, Natural-Laminar-Flow Airfoil. Chapter Five: Topology Optimization of the AFT Element indicated that stiffer skin material was required in the aft element to assist in deflection goals for slot maintenance. The author investigated several composite materials and selected a high modulus carbon fiber M35J produced by Toray Composites [96]. The material properties for Toray M35J are shown in Table 6-1.

Sizing of the aft element structural components followed structural mechanics and procedures outlined in Niu [97]. The aft element consisted of ribs, stringers, and skin. No spar was provided in the aft element due to considerations taken from the previous study which were influenced by the aft elements 'floating' status. Take-off conditions, Table 4-1, were utilized for the sizing of these structural components. The ribs were sized to meet tributary area loading and were placed underneath each slot connector η. Following

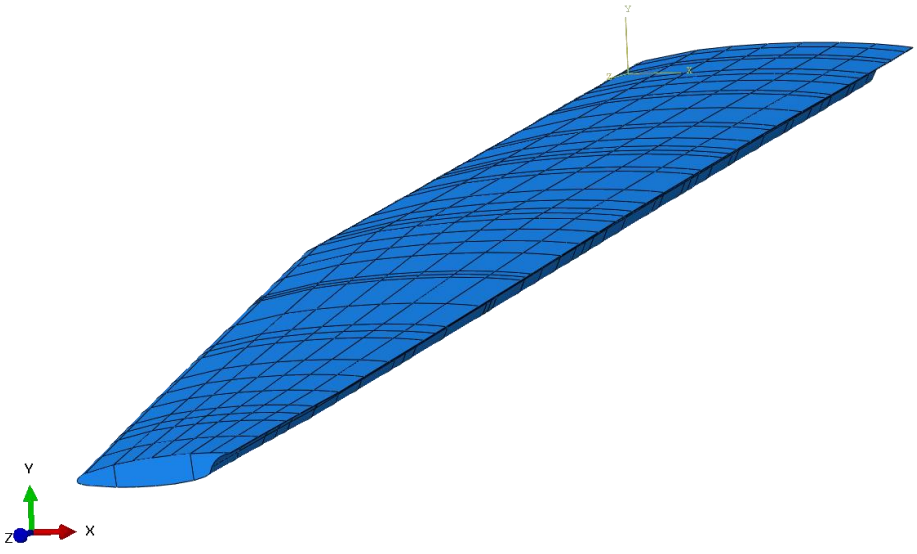


Figure 6-1: Fore element geometric illustration.

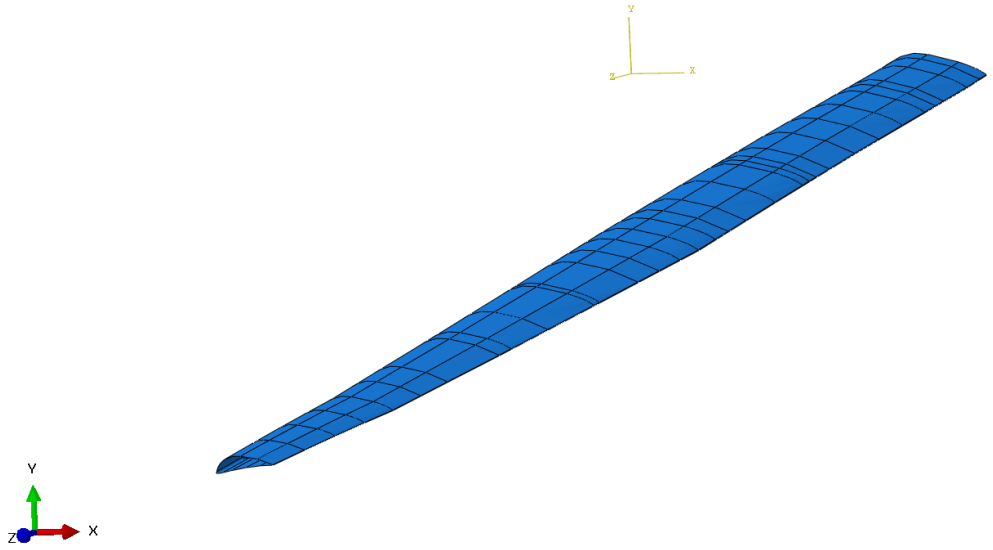


Figure 6-2: Aft element geometric illustration.

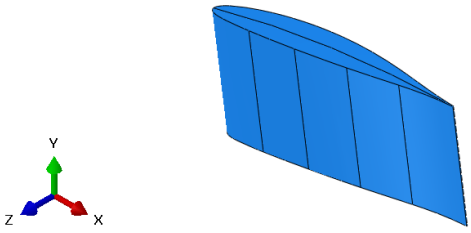


Figure 6-3: Generic slot connector geometric illustration.

Table 6-1: Material Properties for Toray M35J

Property	Value
σ_T	390 ksi
E_T	29 Msi
σ_C	203 ksi
σ_F	239 ksi
E_F	25 Msi

procedures outlined in Niu the panels were first checked for the thickness required to support the max bending stress with no stringers and is expressed as:

$$t_{pr} = \sqrt{\beta p w^2 / \sigma_y} \qquad \textit{Equation 6-1}$$

where t_{pr} is the thickness, β is a coefficient influenced by the panel's length/width ratio and boundary conditions, p is the max suction or pressure on the panel, w is the width of the panel, and σ_y is the yield stress.

The skin panels were also checked for panel buckling. The equation is expressed as:

$$t_b = \sqrt{12\sigma_y(1-v^2) / k\pi^2 E} * w_s \qquad \textit{Equation 6-2}$$

where t_b is the thickness required to meet the buckling requirement, v is the Poisson's ratio, k is the buckling coefficient, E is the Young's modulus, and w_s is the adjusted width of the panel due to the number of stringers. The resulting rib size and panel thickness are detailed in Table 6-2 and Table 6-3.

The fore element structural components also followed procedures outlined in Niu. The spars were the first component to be evaluated and utilized beam analysis to size. VisualAnalysis Edu was used to perform the necessary beam calculations [98]. The take-off conditions were used to produce lifting line loads on the spars. Several other loading considerations were used including fuel, structure weight, and engine weight. Table 6-4 outlines the loads placed on the spars, the loading listed as lb/in indicate the beginning or end of a distributed load. The fuel and engine weights were replicated from the Boeing SUGAR High, a similar aircraft wing structure, and consisted of 5,754 USG and 8,984 lbs respectively [99]. The spars were placed at 25% and 75% of the fore element to avoid icing issues and to provide support to the aft element. The setup using VisualAnalysis Edu is shown in Figure 6-4.

VisualAnalysis Edu provided the required thickness of the spars based on the outer mold line (OML) heights for the front and rear spar locations at various η. Before accepting these thicknesses, the flexural and torsional (EI/GJ) stiffness requirements needed to be addressed. Table 6-5 lists the EI/GJ stiffness requirements for the S207 SNLF Airfoil half-span wing. To ensure these requirements were met, AutoCAD was utilized to analyze the I and J of the wingbox at various η with initial spar thicknesses from the VisualAnalysis Edu process. The front and rear spar at each η was then adjusted to meet the stiffness required. The final fore element front and rear spar thicknesses are shown in Figure 6-5.

The fore element ribs and skin panels were sized similar to the aft element's following Niu procedures. It was observed that the panel buckling controlled the thickness of the skin panels as well. The number of ribs was increased from being

Table 6-2: Aft Element Rib Thickness

Aft rib η	**Aft rib thickness (in)**
0.0180	0.022
0.1250	0.038
0.2500	0.037
0.3750	0.036
0.5000	0.035
0.6250	0.034
0.7500	0.030
0.8750	0.025
0.9750	0.015

Table 6-3: Aft Element Skin Panel Thickness

Panel Between *η*s	**Aft Skin Thickness (in)**
0.0000-0.1250	0.412
0.1250-0.2500	0.401
0.2500-0.3750	0.390
0.3750-0.5000	0.379
0.5000-0.6250	0.368
0.6250-0.7500	0.336
0.7500-0.8750	0.272
0.8750-1.000	0.207

Table 6-4: Fore Element Individual Spar Loads

Load Variable	**Location (*η*)**	**Load Amount**
Lift 1	1.000	51.6937 lb/in
Lift 2	0.5766	130.9773 lb/in
Lift 3	0.0000	149.2468 lb/in
Weight 1	1.000	4.0836 lb/in
Weight 2	0.5766	10.3467 lb/in
Weight 3	0.0000	11.7904 lb/in
Fuel 1	1.000	0 lb/in
Fuel 2	0.5766	6.6725 lb/in
Fuel 3	0.0000	7.6035 lb/in
Engine	0.2	4492 lbs

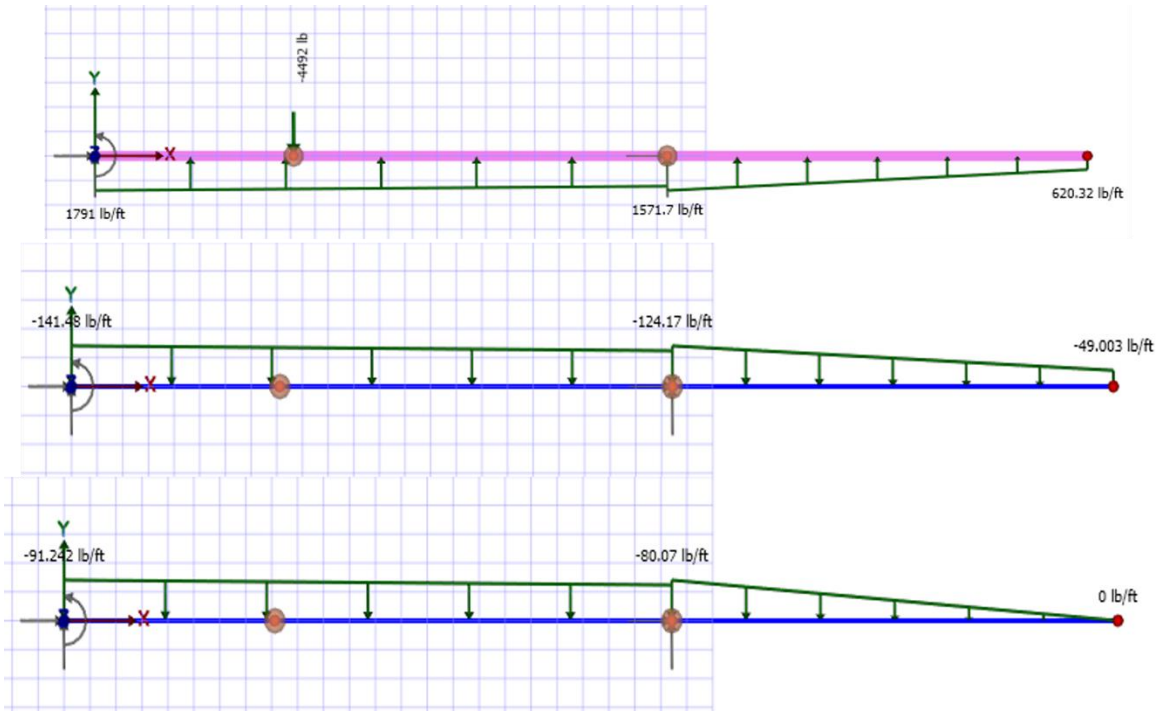


Figure 6-4: Representation of loading input into VisualAnalysis Edu for wing strut calculations.

Table 6-5: S207 SNLF Wing EI and GJ Requirements

η	EI (lb-in^2)	GJ (lb-in^2)
0.0000	5.950E+10	8.624E+10
0.0180	5.100E+10	6.160E+10
0.1060	3.250E+10	3.080E+10
0.3880	1.220E+10	2.676E+10
0.5290	2.175E+10	2.503E+10
0.5766	2.500E+10	3.003E+10
0.6940	8.000E+09	1.540E+10
0.7880	3.300E+09	6.545E+09
1.0000	1.300E+09	8.085E+08

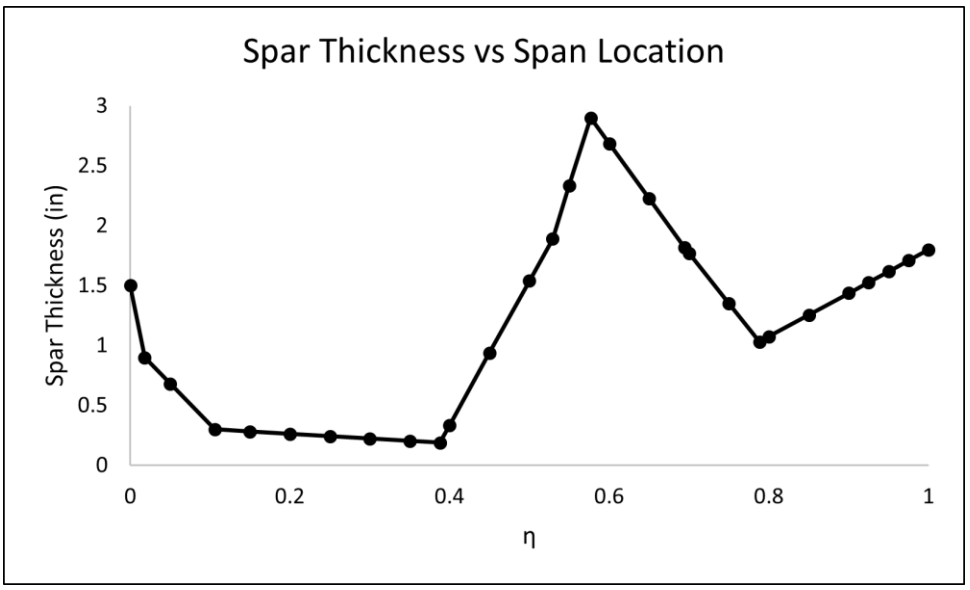


Figure 6-5: Fore element spar thickness at various spans.

underneath each connector to 18. This was chosen to reduce the individual rib thickness as well as the skin panel size between ribs. These resulting rib and skin panel thicknesses are listed in Table 6-6 and Table 6-7. It should be noted that no cap ribs were listed but were set to the closest η's thickness.

The resulting fore element spars, ribs, and skin panels were combined with the aft element ribs and skin panels along with the previously analyzed nine slot connectors to produce the half-span geometry for the demonstration. See Table 4-9 for the sizing and span locations of the slot connectors. AutoCAD was used to model the parts before translation to the finite element solver Abaqus CAE [44]. An overall illustration of fore element spars and ribs along with the aft element ribs can be seen in Figure 6-6. A representation of the fore element spar locations along the S207's chord and the slot connector's location within the slot is shown in Figure 6-7. The aft element's ribs and skin panels consisted of 246,710 S4R shell elements. The fore element's spars, ribs, and skin panels were comprised of 846,665 S4R shell elements. As the slot connectors were solid elements and not shells, they were modeled with C3D10 elements. The resulting element amount for each slot connector is listed in Table 6-8. The number of elements on the slot connectors was altered based on the size and the discretization of the face of the slot connector required to make the faces flush with the fore and aft element.

The loading was the same as the previous study in Chapter Five: Topology Optimization of the AFT Element. The loading was set to the cruise condition for the SNLF airfoil. As previously discussed, the loading conditions provided consisted of 2D η cross-sectional C_p plots and are shown in Figure 5-5. ImageJ was again utilized to pull the C_p values along the upper and lower surface of both the fore and aft element curves [95]. The flight conditions for the cruise configuration are listed in Table 5-3. Equation 5-1 equates the change in pressure, Δp, to the flight conditions and was used to produce the lift placed on the fore and aft element. The pressure was applied to the OML of the elements.

The slot connectors were tied to the fore and aft element OML skins using tie constraints. Boundary conditions were also placed on the fore element at the root connection, $\eta = 0.0000$, and the strut brace location, $\eta = 0.5766$. The root connection fixed the skin and spars while the strut brace pinned the bottom middle node of the fore element rib at that location. Besides the nine slot connectors, the aft element was left 'floating' and was not rooted or supported by a brace.

Results

The finite element results for the half-span demonstration highlighted expectations on how the S207 SNLF airfoil would behave with the slot connectors transferring the induced high-lift load from the aft element to the fore element and then dispersed to either the strut brace or the root connection.

The deflection in the y-direction (upward) of the entire model was of particular interest. The implementation of the strut brace allows the fore element to remain relatively stationary between the root connection and the strut location as observed in Figure 6-8. The fore element beyond the strut brace begins to lift due to its cantilever

Table 6-6: Fore Element Rib Thickness

η	Fore rib thickness (in)
0.0108	0.039
0.0625	0.008
0.1250	0.074
0.1875	0.007
0.2500	0.070
0.3125	0.007
0.3750	0.066
0.4375	0.007
0.5000	0.063
0.5625	0.006
0.6250	0.052
0.6875	0.005
0.7500	0.034
0.8125	0.003
0.8750	0.020
0.9375	0.002
0.9750	0.002

Table 6-7: Fore Element Skin Panel Thickness

η	Fore Skin Thickness (in)
0.0000-0.0625	0.549
0.0625-0.1250	0.541
0.1250-0.1875	0.534
0.1875-0.2500	0.527
0.2500-0.3125	0.520
0.3125-0.3750	0.512
0.3750-0.4375	0.505
0.4375-0.5000	0.498
0.5000-0.5625	0.490
0.5625-0.6250	0.483
0.6250-0.6875	0.448
0.6875-0.7500	0.405
0.7500-0.8125	0.362
0.8125-0.8750	0.319
0.8750-0.9375	0.276
0.9375-1.0000	0.233

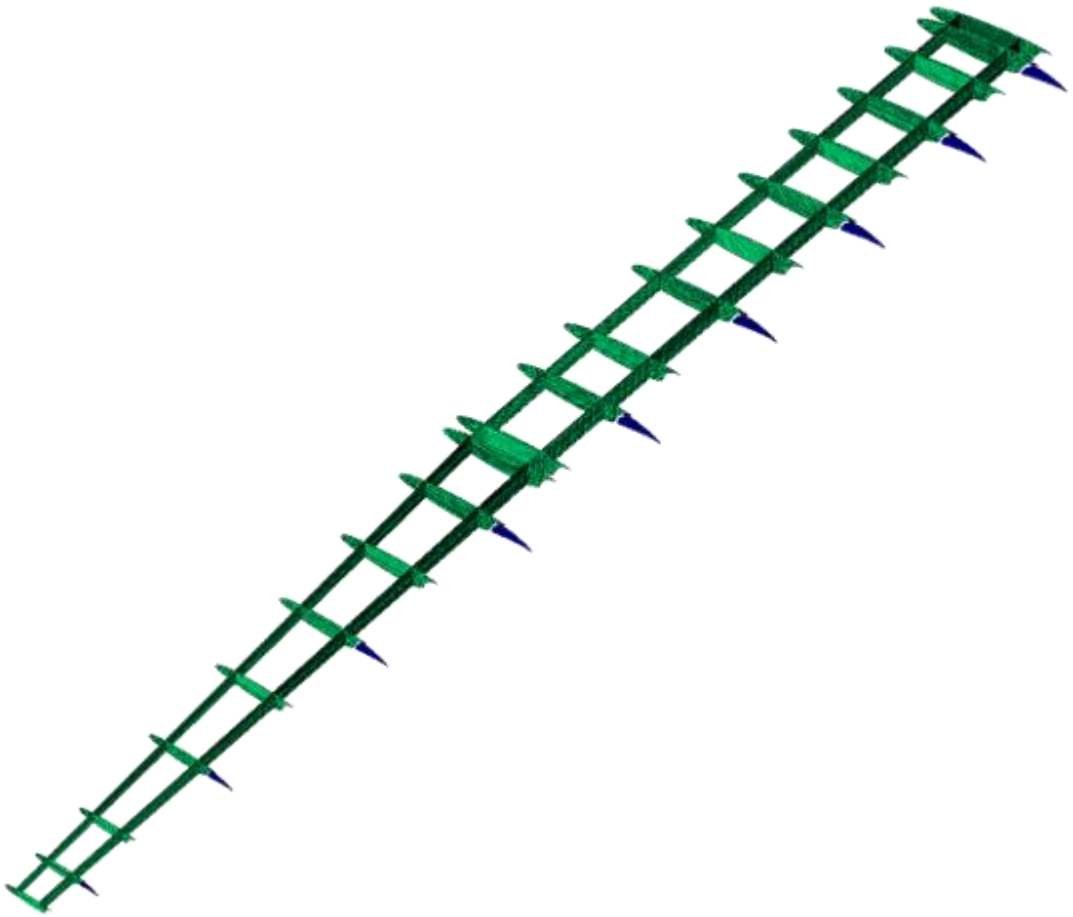


Figure 6-6: Overview of fore and aft element rib and spar placements. Green dictates fore element components and blue dictate aft element components.

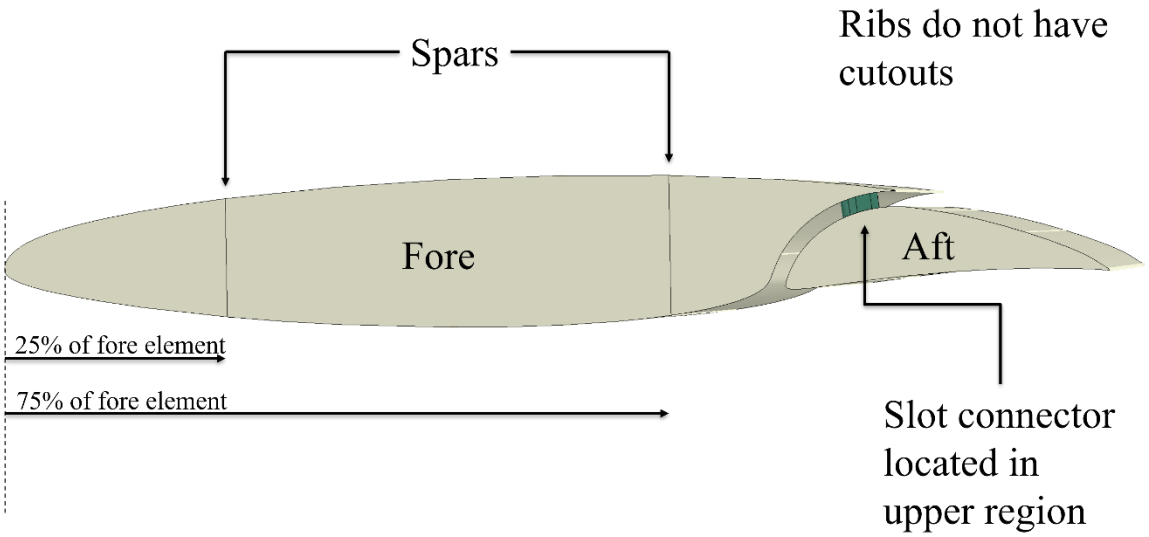


Figure 6-7: Representation of fore element spar locations and slot connector location within the slot.

Table 6-8: Number of C3D10 Elements for the Slot Connectors.

η	# of Elements
0.0180	127,348
0.1250	89,776
0.2500	124,978
0.3750	122,650
0.5000	103,400
0.6250	85,808
0.7500	56,621
0.8750	42,090
0.9750	11,092

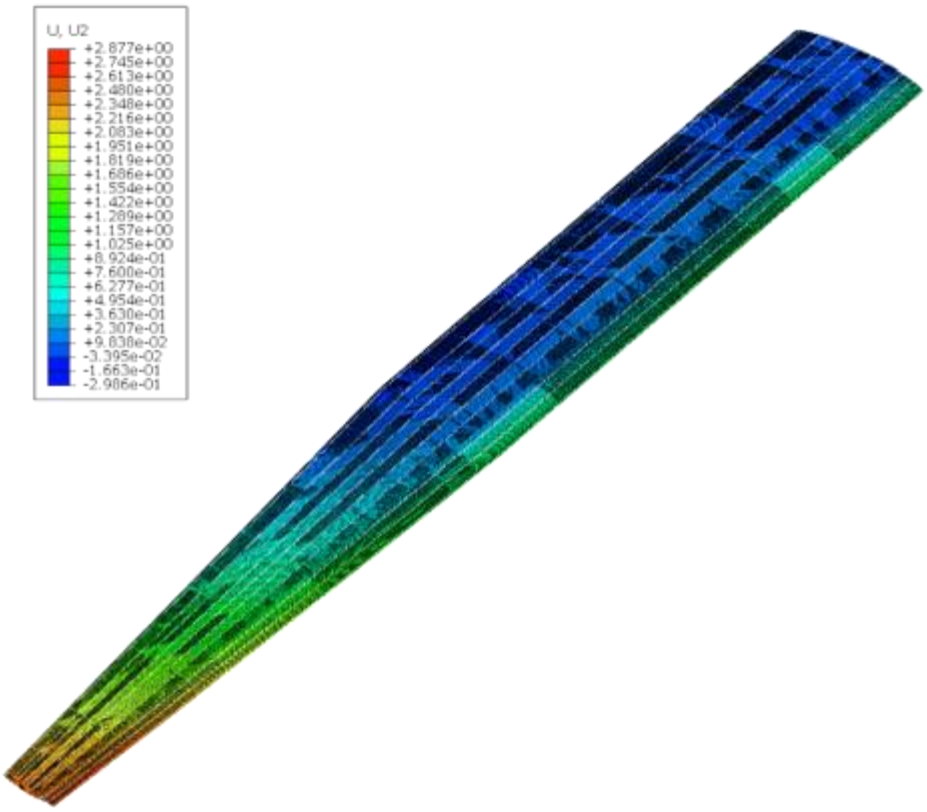


Figure 6-8: Y-direction (upwards) deflection of the entire FE model.

behavior. The tip of the fore element reaches a deflection around 2.48” with the provided cruise loading condition. The aft element is ‘floating’ and does not have the support of a root connection or the strut brace. But due to its particular support structure, i.e. the slot connectors, it largely follows the deflection of the fore element. The aft element between the root and strut location, η = 0.5766, shows deflection of the trailing edge that is consistent across the span. After the strut location, the aft element begins to lift to follow that section of the fore element. Due to the increased lift and lack of support structure the aft element tip observes a larger deflection of 2.88”.

While the magnitude of stress buildup on the aft element skin caused by the connection to the slot connectors varied based on location, the general behavior was the same. The general stress response can be observed in Figure 6-9 where two distinct regions occur. The transfer of the lift from the high-lift aft element through the slot connectors produces a tension and compression region on both the aft skin panels and subsequent aft ribs as the aft element rotates around the connection. The trailing edge of the aft element lifts higher than the leading edge. This causes the upper region of the slot connector to be compressed.

Another important aspect of consideration is how the transfer of the induced lift from the aft element affects the structural elements in the fore element. To highlight this, a comparison of two fore element ribs has been presented. The comparison is shown in Figure 6-10. The fore element rib at η = 0.8125 represents the typical stress state of fore element ribs that do not transfer lift from the aft element from the slot connectors. The fore element rib at η = 0.8750 represents fore element ribs that are attached to slot connectors. The fore element ribs without a slot connector display higher stress zones in the upper middle surface of the wing along with the leading and trailing edges of the bottom surface. The introduction of the slot connector induces a larger stress build-up near the trailing edge of the rib. This stress build-up mirrors the stress response on the aft element structure.

To assist in providing validity to the FE model, Figure 6-11 displays the fore element rib placed at η =0.5766, or where the strut brace is attached. The expectation of this strut brace was to reduce the overall displacement of the wing in the y-direction (upward) and allow for a longer span. As observed in the figure a large tension stress occurs at this connection.

Conclusion

This demonstration highlighted responses from the structural components of the S207 SNLF airfoil when implemented on a global scale with cruise conditions. The ‘floating’ aft element displaced in the y-direction in a co-dependent manner with the fore element. Even though the aft element provided a high-lift load to the wing, the slot connectors were able transfer the load to the fore element structural components and maintain the slot width during the cruise condition. Overall, the wing structure behaved as expected and showed that the slot connectors met their goal with respect to the maintenance of the slot.

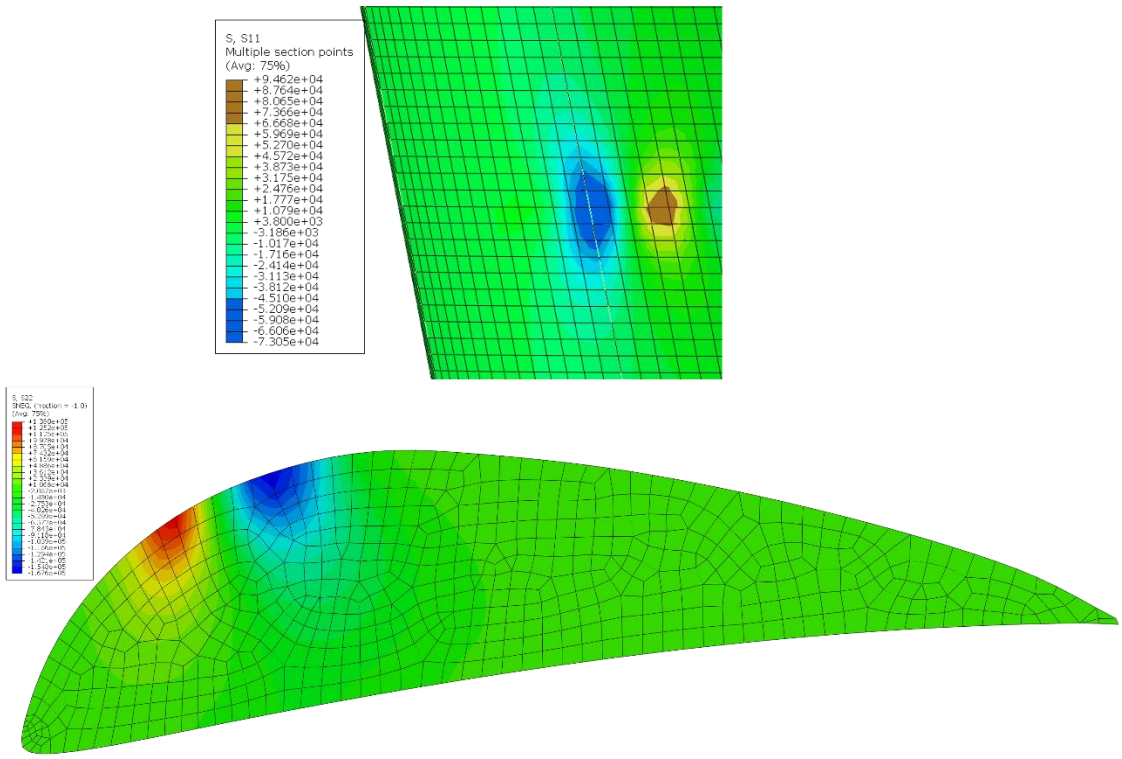


Figure 6-9: Stress build-up on the aft element skin and ribs underneath the slot connectors.

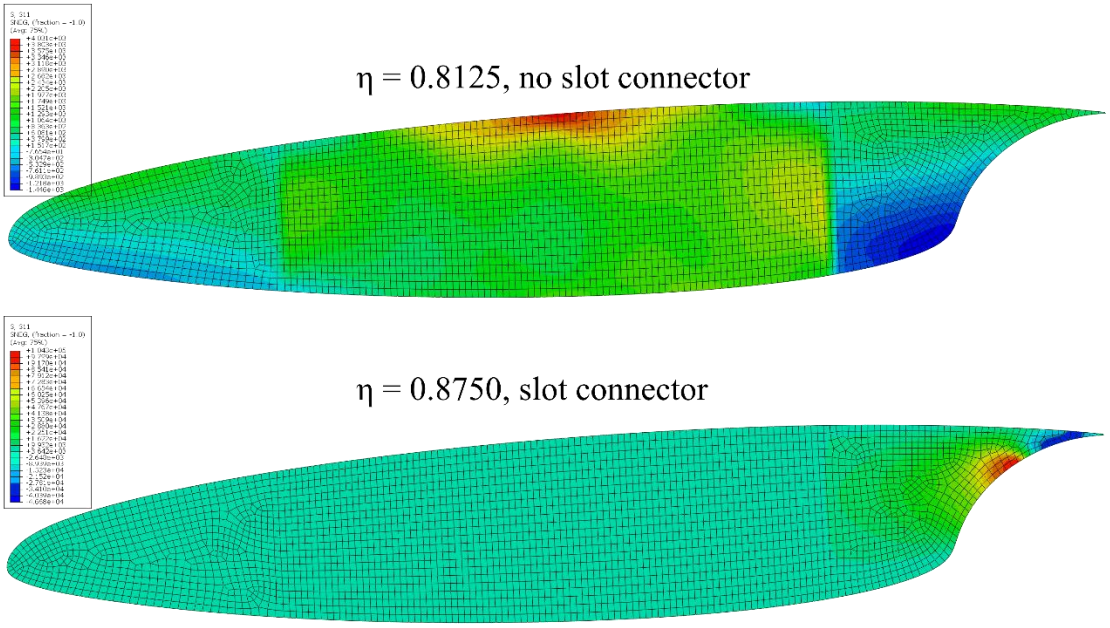


Figure 6-10: Comparison of fore element ribs with stress build-ups. Eta 0.8125 (upper) is representative of the fore element ribs without slot connectors attached. Eta 0.8750 (bottom) is representative of fore element ribs with a slot connector attached.

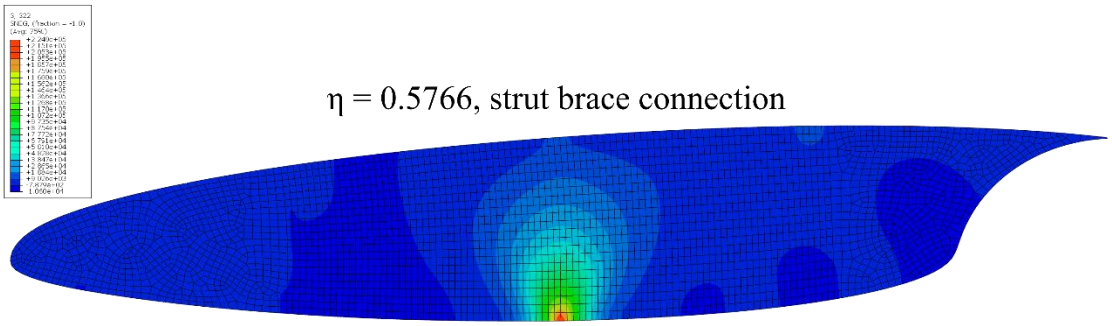


Figure 6-11: Fore element rib displaying tension stress caused by strut brace connection.

Chapter Seven

Nondeterministic Parameter Space Characterization of the Damage Tolerance of a Composite/Metal Structure

Preface

This paper is currently being prepared for publication by Arndt et al. [100]. The author of this dissertation contributed to this publication with conceptualization, data curation, formal analysis, investigation, methodology, resources, software, visualization, writing, and editing.

The use of adhesive bonding could potentially assist in reducing the overall weight of the S207 slotted, natural-laminar-flow (SNLF) airfoil by eliminating bolted or riveted connections between the slot connectors and the skin of the fore and aft element. However, adhesive bonding introduces several complex damage mechanisms that need to be understood and evaluated for proper implementation. This chapter focuses on creating a comprehensive understanding of the damage tolerance of the adhesive joining of a composite to a metallic and creating a method to assist in the design of the implementation.

Introduction

Hybrid materials (optimized combinations of two or more materials with unique properties [101]) can be designed and customized to provide global attributes not offered by each of the component materials individually. One subset of hybrid materials is layered fiber reinforced composite overlays (patches) co-cured to a metal substrate (composite/metal hybrid). Application of composites has been demonstrated to reinforce or repair metallic structures in engineering fields such as aerospace [102-108]. The use of composites in aerospace has increased in an attempt to reduce weight and reduce design time [109]. Composite overlays, bonded to metallic substrates by co-cured bonding methods or adhesive [104, 110], effectively restore the load carrying capacity to fatigue-cracked or corrosion-damaged parts and reinforce under-designed regions. Bonded composite overlays are a desired alternative to traditional repair methods, mechanically fastened metallic patches or complete structural replacement, due to their adaptability to complex substrates, corrosion resistance, customized stiffness, easy installation, high specific strength, and uniform stress transfer [104].

Composite/metal hybrids offer many advantages but have a complex progressive damage that makes it difficult to optimize the design. The progressive damage occurs internally during designed loads or overloads from bending [105, 111, 112] and low-velocity impact [113, 114]. This damage progresses as matrix cracking, fiber breakage (fracture or buckling), delamination within the composite, or disbond at the composite/metal interface. Prior research of the damage analysis of composite overlays is plenty, and focuses on disbond of the adhesives [115-119] and fracture behavior of the bonded metallic substrates [120-124]. Progressive damage in composites has been widely investigated [for example, [125-131]]. Previous studies have demonstrated that the

damage within the composite patch can substantially reduce the performance of the repair or reinforcement [132, 133]. Jones [132] indicated multiple failure modes, including cracking in the adhesive, fiber fracture, and delamination, should be assessed for damage tolerance. Therefore, it is necessary to observe the multiple damage mechanisms to predict damage initiation and propagation in these hybrid structures. This includes the complex progressive failure of the composite overlay and the interactions between the multiple damage mechanisms. This complex progressive failure of composite/metal hybrid structures has been investigated in its entirety, a necessary consideration when evaluating the structural performance of the hybrid structure [134-140]. An aerospace application of composite/metal hybrid structures occurs at stiffener to skin bonding, i.e. Pi and T joints. Action et al. investigated the fail-safe crack arrestment in a T-joint bonded to the aircraft skin [139]. In their research they studied crack arrestment for a multi-loaded bonded T-joint looking at strain energy to predict the delamination and crack propagation. Finlay et al. analyzed composite Pi joints for pull-off and side-bend loading. Their research expanded upon 3D joint models developed by Novak and Selvarathinam who utilized XFEM to study both inter-laminar cohesive zone delamination and intra-laminar damage [141]. Finlay et al. adjusted to the use of cohesive zone model to investigate the progressive failure of the composite Pi joints [140]. While these studies investigated the progressive damage of the composite/metal hybrid structures, they do not quantify the interaction or dominance of the parameters controlling the damage mechanisms.

This study addresses three main challenges in the design analysis and evaluation of composite/metal hybrid structure with respect to damage tolerance. First, given the complexity of the progressive damage with many choices of potential materials and the myriad of uncertainties involved it is infeasible to physically test every potential design to evaluate damage tolerance for even a small subspace of potential configurations. Therefore, a validated computational simulation that enables the exploration of the high dimensional material parameter design space in an economical amount of time and resources was developed. Second, the curse of dimensionality must be overcome. The large number of model inputs encompassing material selection significantly increases the difficulty in identifying the most influential inputs on the damage tolerance of the hybrid structure, as developing a validated surrogate model, and performing sensitivity analysis becomes prohibitive for non-linear, highly dimensional parameter spaces. This challenge is compounded by the likelihood that, during preliminary design and evaluation, many of the parameters may be defined by sparse data, average values, or estimates based on the behavior of similar materials. A systematic, non-deterministic approach was applied to investigate the damage tolerance characterization, sensitivity analysis, and uncertainty quantification to evaluate the effects on damage prediction. Lastly, the parameter space for the individual damage mechanisms that comprise the overall damage tolerance of the hybrid structure were investigated with the use of reduced order modeling (ROM). ROM of the subsectional energies allowed for a deeper understanding of the damage mechanisms. A comprehensive understanding of the damage tolerance informs customized design to minimize failure by difficult to observe damage mechanisms. The

overall goal of this research is to characterize damage tolerance and enable rapid exploration and design of a large material property parameter space.

Materials and Methods

To overcome these challenges, an approach integrating experimental testing, computational modeling, and non-deterministic evaluation using commonly available tools and methods was developed to map the parameter space. This approach is detailed in Figure 7-1. This method was demonstrated on the particular hybrid configuration of an E-glass/epoxy composite patch co-cured to an aluminum 5456 substrate. This work utilizes the high-fidelity 3D finite element (FE) model previously developed by Heng et al. and Arndt et al. [142, 143], which explicitly models each layer of the composite overlay, the metallic substrate, and the interface to predict interacting damage mechanisms including matrix cracking, fiber breakage, delamination within the composite, disbond at the composite/metal interface, and yielding in the metal. The model was evaluated under four-point bending using global sensitivity analysis (GSA), uncertainty quantification (UQ), and data visualization to identify the most influential design parameters, quantify their uncertainty on patch reliability, and guide potential design requirements. This systemic evaluation provides essential knowledge critical to efficient damage tolerant patch design.

Hybrid Structure Configuration

The composite/metal hybrid was fabricated by installing an E-glass/epoxy composite overlay onto a 0.25-inch-thick aluminum 5456 plate employing a hand lay-up procedure with vacuum infusion. The bonded side of the aluminum plate is prepared following the application guide for AC-130, provided by Advanced Chemistry & Technology. A quasi-isotropic laminate is obtained by using ±45° (Vectorply E-BX 1200) and 0°/90° (Vectorply E-LT 1800) stitched fabrics as the main fabric plies. A 0°/90° plain weave ply (Hexcel 7500) ply was selected for the resin rich open bonded side. While a 0°/90° fine harness stain weave ply (Hexcel 7781) was selected as the open side to obtain a quality surface. The ply stacking sequence can be seen in Figure 7-2 and resulted in a 0.16-inch-thick overlay. The adhesive includes an epoxy resin (M1002) mixed with a curing agent (M2046 hardener) and was spread on each fabric during the lay-up procedure. The resulting composite overlay was covered by a P3 perforated film to control the bleed and then had the vacuum bag placed on top. For this composite overlay, the vacuum level was set to 20 inHg for 3 hours and then cured in the oven at 140°F for 4 hours.

Experimental Testing

Physical testing was conducted by Heng et al. [142] and was used to investigate damage initiation and propagation as well as validation of the computational model. The hybrid structure fabricated with the aforementioned method was cut into four-point bending specimens using an Omax 2626 JetMachining Center. The hybrid structure was

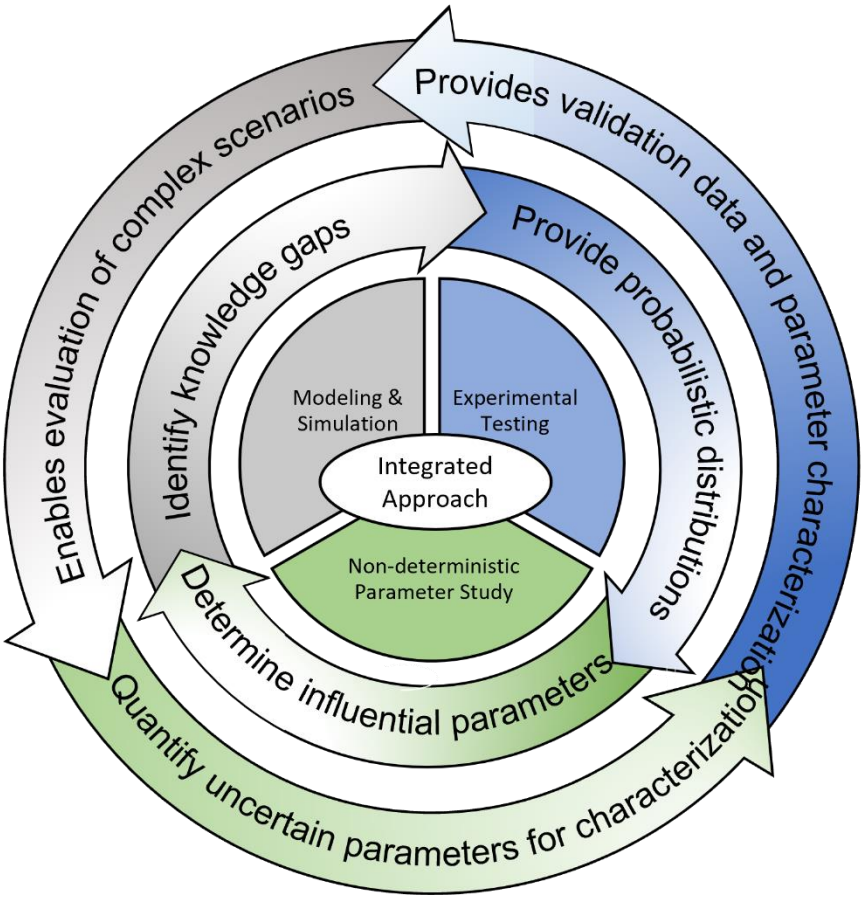
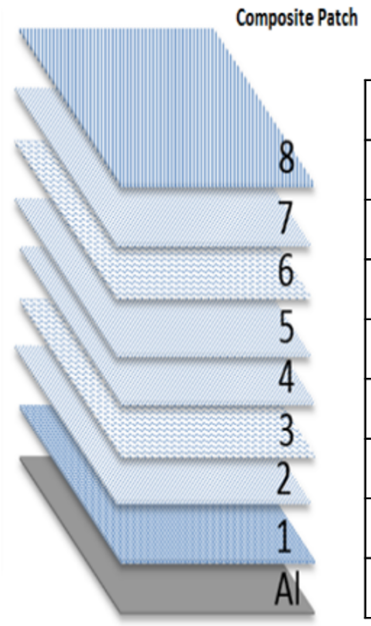


Figure 7-1: Integrated approach to characterize the parameter space.



Layer	E-glass Fabric	Fiber Orientation
1	Hexcel 7500	0°/90° Plain Weave
2	Vectorply E-BX 1200	±45° Stitch
3	Vectorply E-LT 1800	0°/90° Stitch
4	Vectorply E-BX 1200	±45° Stitch
5	Vectorply E-BX 1200	±45° Stitch
6	Vectorply E-LT 1800	0°/90° Stitch
7	Vectorply E-BX 1200	±45° Stitch
8	Hexcel 7781	0°/90° Satin Weave

Figure 7-2: Stacking sequence of composite/metal hybrid structure.

subjected to four different loading scenarios as detailed in Heng et al. This study focuses on the composite overlay placed in tension by having the aluminum 5456 substrate on the top. To help validate the model and investigate the damage propagation and strain field, each of the specimens' front face were sprayed with a flat white paint and then speckled with flat black paint to create a speckle pattern for use with Digital Image Correlation (DIC).

The four-point bending tests were conducted with the use of a MTS Criterion 45 load frame that collected the loading force and displacement of the pins while the DIC system measured the strain field of each specimen. Figure 7-3.a shows the loading configuration where the loading pins are placed at one-third of that of the support pins. A physical representation of the loading scenario and speckling pattern can be observed in Figure 7-3.b. The MTS flexure grips had pins with a 0.2-inch diameter. The loading rate of the MTS load frame was set to 0.05 inch/min following ASTM standards. Both the MTS load frame and the DIC system collected data with the same frequency and were started at the same time to correlate the data.

Computational Simulation

Damage Modeling

Damage modeling in the composite/metal hybrid structure requires the interaction of different methodologies for the metallic substrate, composite laminae, and composite matrix. The only damage for the aluminum 5456 substrate was plasticity. No damage was observed in the metal during experimental testing other than plastic deformation. Additionally, a preliminary FE investigation using the Johnson-Cook damage model yielded zero change in the results [142]. Therefore, damage modeling in the metal was not included and the Johnson-Cook Plasticity Model was kept. To model the intralaminar damage, matrix cracking and fiber fracture, the Continuum Damage Mechanics (CDM) was incorporated. The last damage model used was to model the interlaminar damage, delamination within the composite and disbond at the composite/metal interface, which was modeled with the Cohesive Zone Method (CZM).

CDM for Intralaminar Damage

The CDM approach has been extensively studied to predict composite failure modes, especially in investigations of impact damage modeling [142], and easily integrates stress and strain failure and fracture mechanics. Damage initiation is predicted by the stress and strain failure criteria, while the damage evolution is captured by the fracture mechanics with the use of damage variables.

Micro fiber/matrix cracks and plasticity of the matrix gradually degrade the load carrying capacity of the composite prior to complete failure. The micro cracks are quantified at the macro scale by the CDM which degrades material properties. Damage variables progressively reduce the material stiffness to perform this degradation. Each laminae is modeled as a homogeneous orthotropic material. The fiber dominated tensile or compressive damage is modeled by the elastic damage model. The matrix-controlled shear failure is modeled by the elastic-plastic damage.

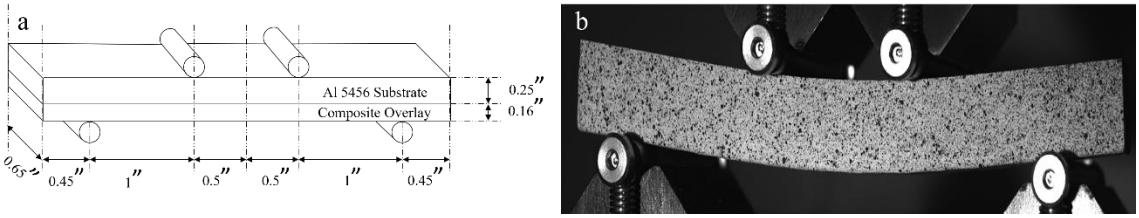


Figure 7-3: a) Representation of Experimental Configuration. b) DIC image captured to display speckling pattern [142].

The constitutive equations for laminae with damage variables in the elastic domain are considered in plane-stress and take the form:

$$\begin{bmatrix}\varepsilon_{11}\\ \varepsilon_{22}\\ \varepsilon_{12}^{e}\end{bmatrix} = \begin{bmatrix}\frac{1}{(1-d_{11})E_{11}} & \frac{-\nu_{12}}{E_{11}} & 0\\ \frac{-\nu_{21}}{E_{22}} & \frac{1}{(1-d_{22})E_{22}} & 0\\ 0 & 0 & \frac{1}{(1-d_{12})2G_{12}}\end{bmatrix}\begin{bmatrix}\sigma_{11}\\ \sigma_{22}\\ \sigma_{12}\end{bmatrix}, \quad d_{11}, d_{22}, d_{12} \in [0, \quad 1] \qquad \textit{Equation 7-1}$$

where d_{11} and d_{22} are damage variables responding to fiber fracture along the 11 and 22 directions and d_{12} is the damage variable associated with matrix deterioration in shear deformation. Tensile and compressive fiber failures are defined with the Eq. 2.

$$d_{11} = d_{11}^{t}\frac{\langle\sigma_{11}\rangle}{|\sigma_{11}|} + d_{11}^{c}\frac{\langle-\sigma_{11}\rangle}{|\sigma_{11}|}, \qquad d_{22} = d_{22}^{t}\frac{\langle\sigma_{22}\rangle}{|\sigma_{22}|} + d_{22}^{c}\frac{\langle-\sigma_{22}\rangle}{|\sigma_{22}|} \qquad \textit{Equation 7-2}$$

$$\langle x\rangle = \begin{cases}0, & x < 0\\ x, & x > 0\end{cases}$$

where fiber fracture under tensile or compressive loading is detailed by d_{11}^{t} and d_{22}^{t}, respectively, and are components of d_{11}. The constitutive equations based on stiffness decay model (Eq. 1) is a simple method to detail the material degradation. However, it is normally accepted to apply the theory of effective stress from the strain equivalence theory:

$$\begin{bmatrix}\varepsilon_{11}\\ \varepsilon_{22}\\ \varepsilon_{12}^{e}\end{bmatrix} = \begin{bmatrix}\frac{1}{E_{11}} & \frac{-\nu_{12}}{E_{11}} & 0\\ \frac{-\nu_{21}}{E_{22}} & \frac{1}{E_{22}} & 0\\ 0 & 0 & \frac{1}{2G_{12}}\end{bmatrix}\begin{bmatrix}\bar{\sigma}_{11}\\ \bar{\sigma}_{22}\\ \bar{\sigma}_{12}\end{bmatrix}, \qquad \textit{Equation 7-3}$$

$$\begin{bmatrix}\bar{\sigma}_{11}\\ \bar{\sigma}_{22}\\ \bar{\sigma}_{12}\end{bmatrix} = \begin{bmatrix}\frac{\sigma_{11}}{(1-d_{11})}\\ \frac{\sigma_{22}}{(1-d_{11})}\\ \frac{\sigma_{12}}{(1-d_{12})}\end{bmatrix} K_i(x) \le 0$$

The nominal stress, σ, causes strain on the damaged material and defines the stress on the undamaged material known as effective stress, $\bar{\sigma}$. This effective stress is a direct approach in defining the damage initiation and damage evolution. Once the effective stress reaches the material strength damage is initiated:

$$\frac{\bar{\sigma}_{ij}}{X_{ij}} = 1, \qquad i,j = 1,2 \qquad \textit{Equation 7-4}$$

where tensile and compressive strength for the uniaxial loading along the fiber is defined with X_{11} and X_{22}. X_{12} is the shear strength. Initiation of the damage dictates the change in the evolution of d_{11} and d_{22} described by exponential equations:

$$d_{ii} = 1 - \frac{1}{k_{ii}} \exp\left\{ -\frac{2U_0^{ii} L_c}{G_{ii}^f - U_0^{ii} L_c} (k_{ii} - 1) \right\}, \qquad i = 1,2 \qquad \textit{Equation 7-5}$$

$$k_{ii} = \frac{\bar{\sigma}_{ii}}{X_{ii}}, \quad U_0^{ii} = \frac{X_{ii}^2}{2E_{ii}}$$

where G_{ii}^f is the fracture energy of laminates in the ii direction, U_0^{ii} is the elastic energy density when damage is initiated and L_c is the characteristic length of the element. Nondecreasing behavior of d_{11} and d_{22} are ensured by having L_c satisfy the following requirement:

$$G_{ii}^f - U_0^{ii} L_c > 0 \qquad \textit{Equation 7-6}$$

Therefore, the element size needs to be small enough to meet this requirement when implementing the damage evolution (Eq. 5) in finite element analysis.
The evolution of d_{12} is described using linear in $ln(k_{12})$:

$$d_{12} = \alpha_{12} \ln(k_{12}), \quad k_{12} = \frac{\bar{\sigma}_{12}}{X_{12}} \qquad \textit{Equation 7-7}$$

where α is a material constant measured by experimental testing.
In addition to the elastic response above, plasticity behavior appears in fabric laminates under shear loading, which is described by the Ludwik-Hollomon [144]:

$$\bar{\sigma}_{12} = \tilde{\sigma}_y + C(\varepsilon_{12}^p)^P, \qquad \varepsilon_{12}^p = \varepsilon_{12} - \varepsilon_{12}^e \qquad \textit{Equation 7-8}$$

where $\tilde{\sigma}_y$ is the effective stress corresponding to the normal stress at the yield point. ε_{12}^p is the plastic part of the total strain ε_{12}. *C* and *P* are material properties of the matrix. When the plastic strain reaches a maximum value, ε_{max}^p, the laminates fail.
The CDM described above details the in-plane damages predicting damage within individual plies of the composite overlay including matrix cracking and fiber fracture.

CZM for Interlaminar Damage

For out-of-plane damages, CZM is applied to model the delamination between plies and the disbond at the interface. The triangular traction-separation law Figure 7-4 is selected for its simple constitutive equations (Eq. 9) and widespread use [145].

$$\begin{cases} t = K\delta, & t \le t^0 \\ t = \dfrac{t^0(\delta - \delta^f)}{\delta^0 - \delta^f}, & t > t^0 \end{cases} \qquad \textit{Equation 7-9}$$

where *t* is the traction, *K* is the interface stiffness relating the traction and corresponding separation before the damage initiation, δ is the separation, t^0 is the damage initiation stress, δ^f is the maximum separation where the element totally fails, and δ^0 is the separation at damage initiation. G_c is the critical fracture energy and has the same value as the shaded area under the triangle in Figure 7-4. G_c can be directly measured from experiments while *K*, t^0, and δ^f are obtained by empirically fitting the experiment data.

Delamination in the composite resulting from mixed mode fracture is predicted by the quadratic stress criterion, which determines damage initiation and evolution:

$$\left\{\frac{\langle t_I \rangle}{t_I^0}\right\}^2 + \left\{\frac{t_{II}}{t_{II}^0}\right\}^2 + \left\{\frac{t_{III}}{t_{III}^0}\right\}^2 = 1 \qquad \textit{Equation 7-10}$$

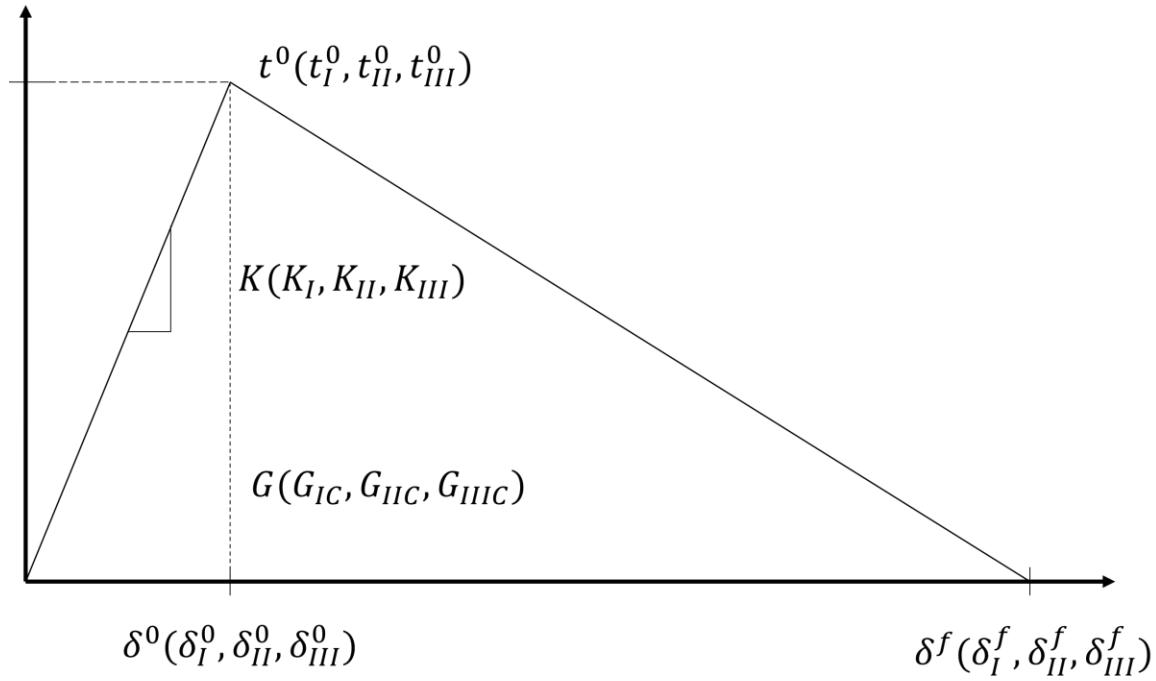


Figure 7-4: CZM triangular traction-separation law.

where t_I, t_{II}, and t_{III} are tractions for Mode I, Mode II, and Mode III fracture. t_I^0, t_{II}^0, t_{III}^0 are the damage initiation stresses for the three modes of fracture. When the left side of Eq. 10 equals unity damage is initiated.
The mixed mode fracture criterion is defined by one of the most widely used expressions for the critical release rate of mixed-mode loading, and was proposed by Benzeggagh and Kenane [146]:

$$G_c = G_{Ic} + (G_{IIc} - G_{Ic})\left(\frac{G_{II} + G_{III}}{G_I + G_{II} + G_{III}}\right)^n \qquad \textit{Equation 7-11}$$

where G_c is the critical energy release rate for mixed-mode fracture. G_{IC} and G_{IIC} are the critical energy release rates for Mode I and Mode II fracture. G_I, G_{II}, and G_{III} are energy release rate for the three modes of fracture. n is a material property measured by experimental testing.

Data Acquisition and Quality

Before beginning computational simulation or non-deterministic analysis, an essential first step was to quantify the current design parameters, material properties, and investigate the data quality of the complex parameter space. The material properties were acquired from several sources and have varying quality. Some data was obtained from comprehensive test programs performed by the Naval Surface Warfare Center Carderock Division while other parameter data was approximated using literature values for similar materials [147]. In some cases, data was sparse for a given parameter, and data may have been collected from disparate sources. Rather than unnecessarily performing comprehensive and potentially costly and time-consuming experimental testing for every parameter, the results of the non-deterministic parameter study inform the focused characterization of the most influential parameters. If a parameter is highly influential and based on low quality data, it should be fully characterized and specified with tight tolerances. Figure 7-5 classifies the data quality into subsections depending on the varying sources including experimental data with sufficient samples, sparse experimental data or manufacturer's data, values estimated based on similar materials, and empirically fitting data. The parameters defined using data classified with low quality are candidates for more rigorous characterization if the non-deterministic parameter study identifies the parameter as highly influential. A detailed description of the material models and parameter definitions are discussed below with parameter values listed in each table.

Table 7-1 lists the elastic-plastic properties of the aluminum 5456 as determined by a cylindrical tensile testing experiment [147]. The Johnson-Cook equation (Eq. 12) is used to describe the strain hardening phenomenon,

$$\bar{\sigma} = A + B\bar{\varepsilon}^n \qquad \textit{Equation 7-12}$$

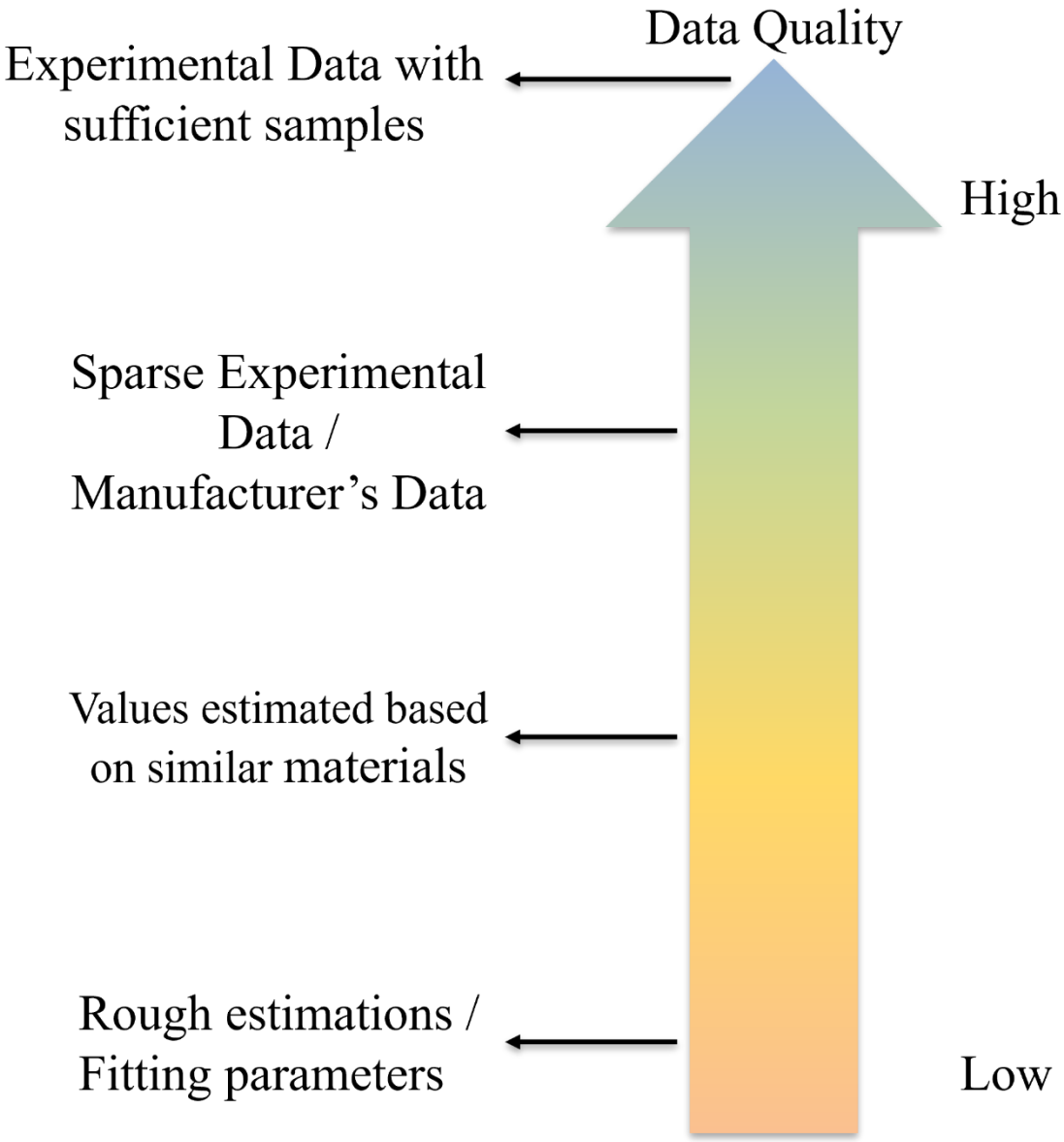


Figure 7-5: Color gradation for data quality.

Table 7-1: Elastic and plastic properties for aluminum 5456-H116

Meaning	Written Symbol	Abaqus Symbol	Material Property
Young's Modulus	$E_{11} = E_{22}$	E	10.10 msi
Poisson's Ratio	ν_{12}	ν	0.29
Yield Stress	σ_y	A	29.8 ksi
Strength Coefficient	B	B	103.6 ksi
Strain Hardening Exponent	n	Aln	0.607

where $\bar{\sigma}$ is the equivalent plastic stress, $\bar{\varepsilon}$ is the equivalent plastic strain, and *A*, *B*, and *n* are material constants.

The properties of the resin between the laminate plies and composite/metal interface are displayed in Table 7-2 and Table 7-3 respectively. ENF and DCB tests on the Hexcel 7500 were used to determine these and were performed as detailed by ASTM D5528 and D7905

The properties for the laminae were obtained from various sources including experimental testing, manufacturers or literature data, or empirical fitting. These properties are detailed in Table 7-4, Table 7-5, and Table 7-6. Lack of shear property data caused each of the four laminae to be assigned the same shear properties. This was considered acceptable as each of the four laminae have the same matrix that dominates the shear properties. The intralaminar fracture toughness of Hexcel laminae were estimated from similar E-glass/Epoxy weave fabric from Mandell et al. [148] while the intralaminar fracture toughness of the E-BX/E-LT laminae were estimated from Hallet et al. [149]. The Young's modulus and tensile strength of the E-BX/E-LT laminates were acquired by the manufacturer's data. The shear properties were derived using a technique detailed by Johnson et. al [150].

Computational Modeling

Carrying out all the experimental testing required for a comprehensive study including all variations of the design parameters of the complex space is computational exhaustive. Computational simulation is an alternative method to efficiently explore the complex design space of the composite/metal hybrid structure after validation of a baseline model is generated through experimental testing. A high-fidelity 3D FE model, as shown in Figure 7-6, was developed using ABAQUS CAE [44] to investigate the varying damage mechanisms under a four-point bending configuration and was validated with the experimental data. Figure 7-6.A. displays the full model with the pins, while Figure 7-6.B details each material and the damage model employed for them. The aluminum 5456 substrate was modeled using solid elements (C3D8R). Each of the fabric layers were modeled explicitly and modeled with continuum shell elements (SC8R). The CDM damage model of each laminae is incorporated with an built-in ABAQUS VUMAT user subroutine [150, 151]. Cohesive elements (COH3D8) were included between each laminae and at the composite/metal interface to capture delamination and disbond respectively. These elements utilized the triangular traction-separation law integrated in ABAQUS as detailed with CZM. The parameters for these cohesive elements; element size, stiffness, and strength, were selected according to guidelines from Turon et al. [152]. Rigid bodies were used to model the support and loading pins to recreate the experimental boundary and loading conditions. The resulting model consisted of a total of 111,291 elements.

For computing efficiency and automation, damage evaluation was interpreted as five output energies representing the damage mechanisms under consideration: plastic deformation in the aluminum (*PDf_m*), shear plasticity in the composite (*PDf_l*), interlaminar fracture in the composite (*DMDf_l*), delamination in the composite (*DMDf_c*), and disbond at the composite/metal interface (*DMDf_i*). The damage

Table 7-2: Mechanical properties of resin between laminate plies

Meaning	Written Symbol	Abaqus Symbol	Material Property
Elastic Modulus	E / E_n	*EC*	10 msi
Nominal Stress Normal-only Mode	σ_{nn}	*XT*	7.614 ksi
Nominal Stress First/Second Direction	$\sigma_{ss} = \sigma_{tt}$	*XS*	4.8786 ksi
Normal Mode Fracture Energy	$G_{c,nn}$	*GI*	7.6 lb-in/in^2
Shear Mode Fracture Energy First/Second Direction	$G_{c,ss} = G_{c,tt}$	*GII*	16.588 lb-in/in^2
Mixed Mode Behavior for Benzeggagh-Kenane	*B-K*	*BK*	2.6

Table 7-3: Mechanical properties of resin between composite/metal interface

Meaning	Written Symbol	Abaqus Symbol	Material Property
Elastic Modulus	E / E_n	*ECi*	10 msi
Nominal Stress Normal-only Mode	σ_{nn}	*XiT*	15.288 ksi
Nominal Stress First/Second Direction	$\sigma_{ss} = \sigma_{tt}$	*XiS*	9.7572 ksi
Normal Mode Fracture Energy	$G_{c,nn}$	*GiI*	7.6 lb-in/in^2
Shear Mode Fracture Energy First/Second Direction	$G_{c,ss} = G_{c,tt}$	*GiII*	16.588 lb-in/in^2
Mixed Mode Behavior for Benzeggagh-Kenane	*B-K*	*BKi*	2.6

Table 7-4: Mechanical Properties of Laminates I

Meaning	Written Symbol	Abaqus Symbol	Material Property	Abaqus Symbol	Material Property
		E-BX 1200		***E-LT 1800***	
Young's Modulus	$E_{11}+$ / $E_{11}-$ = $E_{22}+$ / $E_{22}-$	*E1200*	2.8 msi	E1800	2.8 msi
Tensile Strength	$X_{11}+$ / $X_{11}-$ = $X_{22}+$ / $X_{22}-$	*X1200*	53 ksi	X1800	53 ksi
Poisson's Ratio	$v_{11}+$ / $v_{11}-$	*v1200*	0.15	v1800	0.15
Intralaminar Fracture Toughness	$G_I^f = G_{II}^f$	*G1200*	150 lbs/in	G1800	150 lbs/in

Table 7-5: Mechanical Properties of Laminates II

Meaning	Written Symbol	Abaqus Symbol	Material Property	Abaqus Symbol	Material Property
		Hexcel 7500		***Hexcel 7781***	
Young's Modulus	$E_{11}+$ / $E_{11}-$ = $E_{22}+$ / $E_{22}-$	E7500	2.83 msi	E7781	4.4 msi
Tensile Strength	$X_{11}+$ / $X_{11}-$ = $X_{22}+$ / $X_{22}-$	X7500	46.7 ksi	X7781	70 ksi
Poisson's Ratio	$v_{11}+$ / $v_{11}-$	v7500	0.15	v7781	0.15
Intralaminar Fracture Toughness	$G_I^f = G_{II}^f$	G7500	100 lbs/in	G7781	100 lbs/in

Table 7-6: Mechanical Properties of Laminates (Laminar Shear)

Meaning	Written Symbol	Abaqus Symbol	Material Property
Shear Modulus of Laminate	G_{12}	*GS*	0.8 msi
Shear Strength of Laminate	X_{12}	*SS*	5.16 ksi
Shear Damage Parameter	α_{12}	*alpha12*	0.2767
Maximum Shear Damage	d_{12}^{max}	*d12*	0.714
Maximum Shear Plastic Strain	ε_{max}^{pl}	*epsilon*	0.02
Effective Shear Yield Stress	σ_{12}	*sigmaY*	5.16 ksi
Coefficient in Shear Hardening Equation	*C*	*C*	0.65 msi
Power Term in Shear Hardening Equation	*P*	*P*	0.729

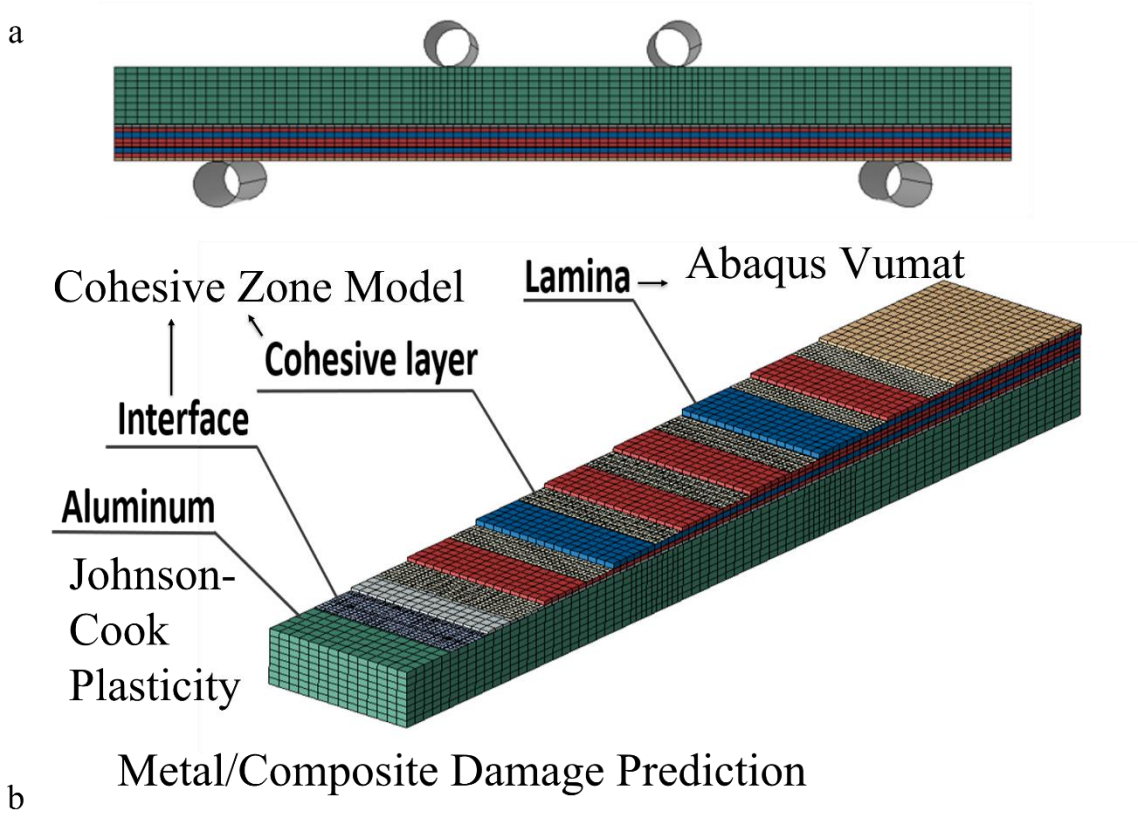


Figure 7-6: a) FE model illustrating the different layers. b) Breakdown of FE model illustrating the damage models for each aspect.

evaluation was also interpreted using the total energy output (*Df_T*) as a combination of these five output energies. The *Df_T* absorbed is initially used to investigate the complex parameter space in its entirety, while the subsections of output energies are investigated using a simplified approach to highlight potential trends and design considerations.

Non-deterministic Parameter Study

Data Sampling

Prior to performing the non-deterministic parameter study the complex parameter space needed to be sampled to produce viable output for the generation of the surrogate model, GSA, UQ, and visualization. This was done with the use of a software Distribution-based Input for Computational Evaluations (DICE), which samples the input parameters as probabilistic parameters [153]. DICE is a general use tool that takes raw input files and parameter definitions and returns ready-to-execute input files and sampling lists. Due to lack of experimental testing, the sampling was performed using either a ±20% of the mean values with a uniform distribution for surrogate modeling and GSA or a normal distribution with the standard deviation set to 10% of the mean value for UQ. The parameter space was sampled using Monte Carlo sampling. The surrogate models and GSAs were sampled with Latin Hypercube Sampling (LHS) [154], one of the most common sampling methods, while the UQ space was sampled with Latin Stratified Sampling (LSS) [155].

Surrogate Modeling

A full parameter space sampling using a high-fidelity FE model would have been computational exhausting, especially with large number of parameters and uncertainty in the linearity of their response. Therefore, a surrogate model was developed to meet the sampling requirements for the GSAs and UQ analyses. Surrogate models are analytical approximations that can predict the behavior of high-fidelity FE models with a limited number of data sets. One of the most widely used surrogate modeling techniques Artificial Neural Network (ANN) [156] was selected to generate the surrogate model. The principle of this surrogate model is summarized as an approximation function $\hat{f}$ of the true model *f*. With careful construction, these models can replicate the behavior of complex high-fidelity FE models accurately with a fraction of the computational cost. With ANN the approximation function $\hat{f}$ describes a set of features organized with a hierarchy. Each layer starts by taking the previous layer's inputs and generates the output for the next layer. Each layer consists of nodes, or neurons, that represent a unit of computation in the approximation. The nodes perform a linear transformation of one or more inputs (Eq. 13) followed by a nonlinear transformation applied by the activator *(σ(·))*.

$$\sum_{i}^{H} w_i \cdot x_i + b \qquad \textit{Equation 7-13}$$

where w_i is the weight coefficient for the linear transformation. These weight coefficients are tunable and are adjusted to minimize the error between each layer. The general process for surrogate model generation is detailed in Figure 7-7.
The surrogate models for this study were generated using Google TensorFlow [157], an open-source software library, and predicted the *Df_T* absorbed for the composite/metal hybrid structure as well as four of the subsectional energies (*PDf_m*, *PDf_l*, *DMDf_l*, and *DMDf_c)*. The input for these surrogate models were generated using DICE with a uniform distribution and consisted of 1,555 data points for each of the 41 input parameters and output energies acquired by the FE model. The ANN consisted of a Sequential Keras model implementing a Scikit-Learn KerasRegressor interface with a normal initializer and a relu activator. The number of hidden layers and nodes per layer were swept until an adequate fit was established while making sure to keep the overall structure of the ANN to a reasonable number of layers and node structure to avoid overfitting of the output parameter being investigated.

Global Sensitivity Analysis

To access the influence of the input parameters on the resulting predicted *Df_T* absorption of the composite/metal hybrid structure, GSA was performed by employing Sobol indices [158]. Sobol indices is a commonly used variable-based approach to GSA which measures each parameter's influence by delineating its contribution to the total variance of the output. The first-order effects are the influence of an individual input parameters caused by themselves. The use of Sobol indices also allows for the investigation of higher-order effects, the contributions of several variables together, which can prove useful to investigate interaction between highly influential parameters. A large total-order index identifies a parameter as influential on the output. A comparison of the first-order and total-order indices indicates the impact of interaction. Similar indices indicate little interaction with other input parameters. While a large difference informs that the parameter is impactful with its interactions to others.

The calculation of Sobol indices is modeled with the following form:

$$Y = f(X),\ X = \{X_1, X_2, X_3, \dots X_m \qquad \textit{Equation 7-14}$$

where *X* is the vector of *m* inputs, *Y* is the model output, and *f* is a square integrable function. The Sobol indices considers an expansion of the function:

$$f(X) = f_0 + \sum_{i=1}^{m} f_i(X_i) + \sum_{i<j}^{m} f_{ij}(X_i, X_j) + \cdots + f_{1,2,\dots,m}(X_1, X_2, \dots, X_m) \qquad \textit{Equation 7-15}$$

in which f_0 is a constant, and the other terms are functions of corresponding inputs with a zero mean. Squaring both sides of Eq. 15 results in:

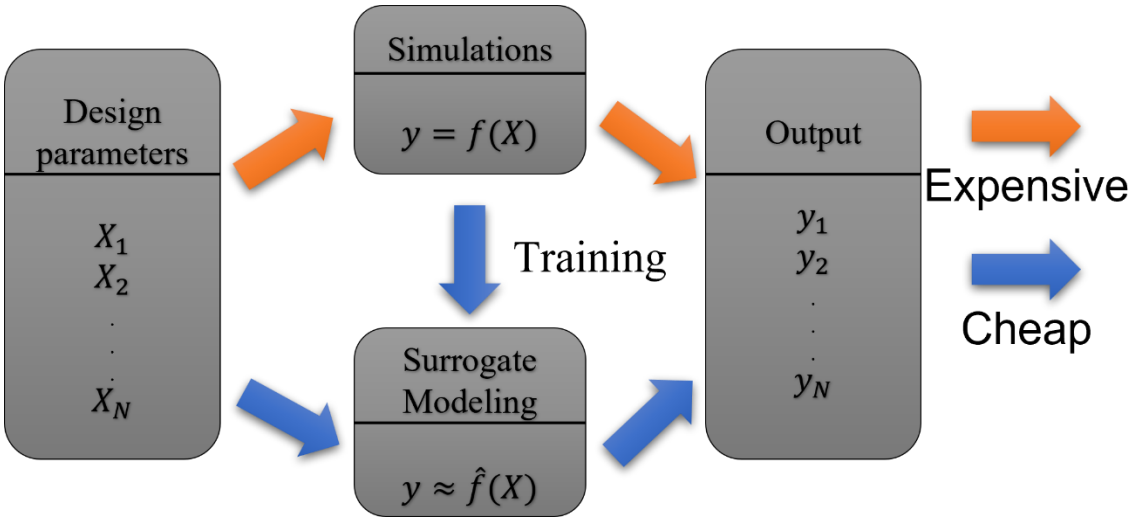


Figure 7-7: Visualization of surrogate model generation and use.

$$V(Y) = \sum_{i=1}^{m} V_i + \sum_{i<j}^{m} V_{ij} + \cdots + V_{1,2,\ldots,m} \qquad \textit{Equation 7-16}$$

where $V(Y)$ is the variance of Y, V_i is the variance of $f_i(X_i)$ and so on. Dividing both sides of Eq. 9 by $V(Y)$ yields:

$$\sum_{i=1}^{m} S_i + \sum_{i<j}^{m} S_{ij} + \cdots + S_{1,2,\ldots,m} = 1 \qquad \textit{Equation 7-17}$$

where S_i is the first-order index, S_{ij} is the second-order index and so on. S_i shows the influence of X_i on the variance of the output and S_{ij} shows the influence of interactions between X_i and X_j on the variance of the output. It can be computational intense to compute all indices, as such only the first-order and total-order indices were calculated unless required.

S_i for single parameter is the ratio of two variance computations, Eq. 18. Where the numerator is calculated as the variance of the mean of the output parameter conditioned on a single, fixed input parameter. The mean of this numerator is evaluated multiple times across the sample space, thus incorporating the impact across the entire space of that parameters range. The denominator normalizes the index with respect to the variance across the sample space, allowing for comparison across various input parameters for the same output parameter.

$$S_1^i = \frac{V_{x^i}\left(E_{X^{\sim i}}\left(Y\middle|X^i\right)\right)}{V(Y)} \qquad \textit{Equation 7-18}$$

The total-order index is the total contribution of one input to the output variance. An example is seen with Eq. 19 showing the total index of X_i on a model with only three inputs.

$$S_{T1} = S_1 + S_{12} + S_{13} + S_{123} \qquad \textit{Equation 7-19}$$

The total-order effect of a parameter identifies not only the independent parameter effects, but its effects due to all the interactions under investigation. Eq. 13 shows the commonly used analog evaluation the total effects as unity minus the effects of all parameters except the evaluated input. This alternative approach provides significant computational efficiency.

$$S_{Ti} = 1 - \frac{V[E(Y|X_{\sim i})]}{V(Y)} \qquad \textit{Equation 7-20}$$

Where $E(Y|X_{\sim i})$ is the conditional expectations of the output Y when input X_i is not considered.

Sobol indices provides an efficient and effect method to explore the influence of the complex parameter space presented by the composite/metal hybrid structure. However, it requires a heavily populated data set to converge which is implausible for the complex parameter space without the use of the generated surrogate models. The parameter space was investigated using Monte Carlo LHS with a unified distribution to generate an efficient sampling. The surrogate model was utilized to investigate this sample space to reduce the computational time.

FDR LogWorth

In an attempt to efficiently investigate the subsections of energies a secondary analysis was employed with the use of False Discovery Rate (FDR) LogWorth [159, 160]. This secondary analysis significantly reduces the manual intensive aspects of performing GSA for the additional subsections of energies.
The FDR LogWorth is calculated with Eq 21.

$$FDR(LogWorth) = -log_{10}(FDR\ p - value) \qquad \textit{Equation 7-21}$$

A p-value < 0.05 signifies a parameter is significant. With FDR LogWorth the higher the value the more significant the parameter is on the energy absorption. For this study FDR LogWorth was compared to the Sobol indices for the *Df_T* absorption as a comparison to find a significance cutoff. Then FDR LogWorth was utilized to select the parameters being explored by the reduced order surrogate models for the subsections of energies.

Uncertainty Quantification

UQ was performed using the traditional Monte Carlo sampling method with LSS to evaluate the uncertainty in the output relative to our non-deterministic input. To reduce the expense of investigating the complex parameter space only the most influential parameters indicated by the GSA were investigated for uncertainty. DICE was used to sample a large number of input sets using a normal distribution. Convergence was determined by investigating three data quantities including 2,500, 5,000, and 10,000 data points. To fully study the parameter space the surrogate model was utilized to investigate a sweep in the uncertainty by adjusting the number of parameters investigated until the percent change in the predicted *Df_T* absorbed was small.

Results and Discussion

Computational Validation and Results

Validation for the FE model was assessed in two folds. The first was a comparison of force-displacement curves measured by the MTS load frame and the FE model's output. The resulting graph is shown in Figure 7-8. It can be stated that the FE results reasonably align with that of the experimental and captures the progressive damage of the overlay. The first peak, P_1, corresponds to the intralaminar fracture delamination of the first ply (Hexcel 7781). By observing the FE results it was determined that the shear failure of the fourth and fifth plies (E-BX 1200) caused the dip after the second peak, P_2. This conclusion indicates that the distance between the first two peak loads is controlled by the shear properties of the laminates.

The second aspect of our validation is the comparison of the DIC strain-fields to those observed with the FE model. Figure 7-9 shows these results, the comparison illustrates that the FE model is recording similar strain-fields and location of damage initiation and progression. With the FE model validated we pulled five output energies to represent our varying damage mechanisms: plastic deformation in the aluminum, shear plasticity in the composite, interlaminar fracture in the composite, delamination in the composite, and disbond at the composite/metal interface. Figure 7-10 displays the energy distribution recorded by the FE model. It is understandable that majority of the energy was absorbed by the aluminum 5456 substrate since it is a larger thickness than the composite overlay and placed on top. The plastic deformation accounted for an average 66.9% of the energy absorbed. Inherently, the material parameters linked to this energy absorption will be highlighted as the most influential to the *Df_T* absorption of the composite/metal hybrid structure. The next two highest energy contributors were shear plasticity of laminates and the delamination with 13.2% and 14.3% respectively. The properties of the matrix control these damage mechanisms. As such, the damage tolerance of this composite/metal hybrid structure is controlled by the plasticity in the aluminum 5456 substrate and the composite matrix and the non-deterministic analyses should highlight this.

Surrogate Modeling of Total Energy Absorption

The first surrogate model generated consisted of the full 41 parameter space with respect to the *Df_T* absorption. The resulting surrogate model consisted of a KerasRegressor with two hidden layers with 60 and 80 nodes respectively. The KerasRegressor required a normal initializer and a relu activator. The surrogate model was analyzed using mean absolute error against 25 randomly pulled data sets that were not used for training or testing. Figure 7-11 shows the 45° plot of the randomly selected data points with the predicted *Df_T* absorption vs the actual *Df_T* absorption, measured by the FE model. Majority of the predictions fall within 5% error of the actual with only three data points falling outside. It is also observed that the three outliers all were within the 10% error bars. With the complex parameter space and limited data sampling, this was considered an adequate fit to avoid overfitting the model with excessive training.

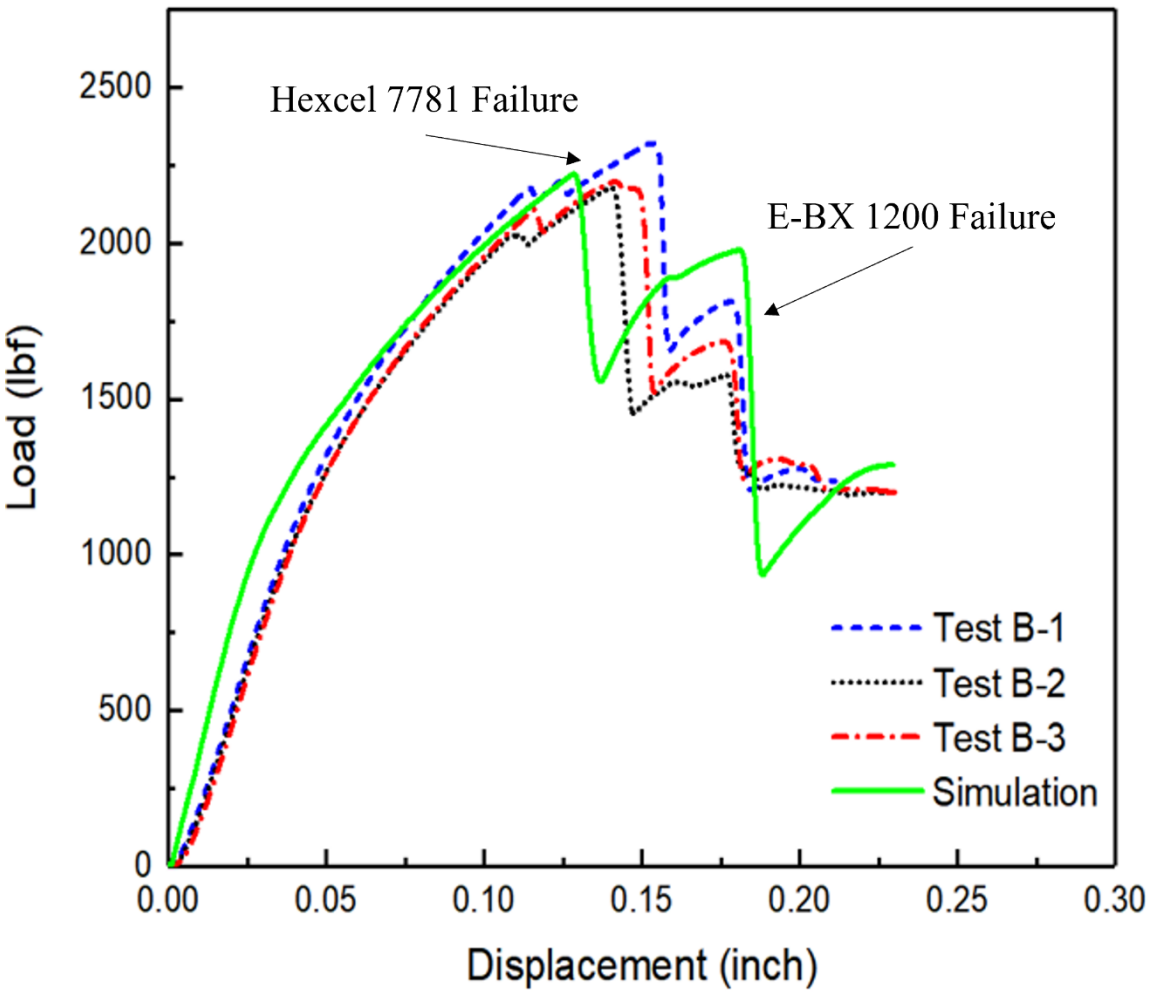


Figure 7-8: Validation of FE model illustrated by the comparison of experimental force-displacement curves vs the simulation. Original graph provided courtesy of Heng et al. [142].

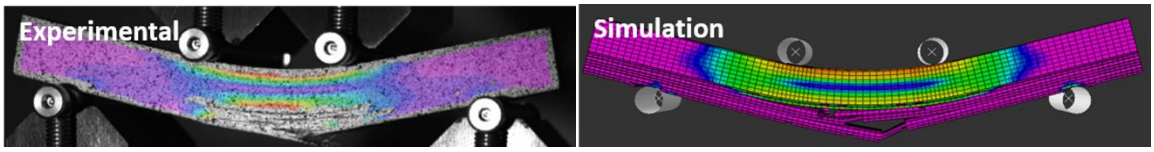


Figure 7-9: DIC results compared to the simulation for further validation. Original images provided courtesy of Heng et al. [142].

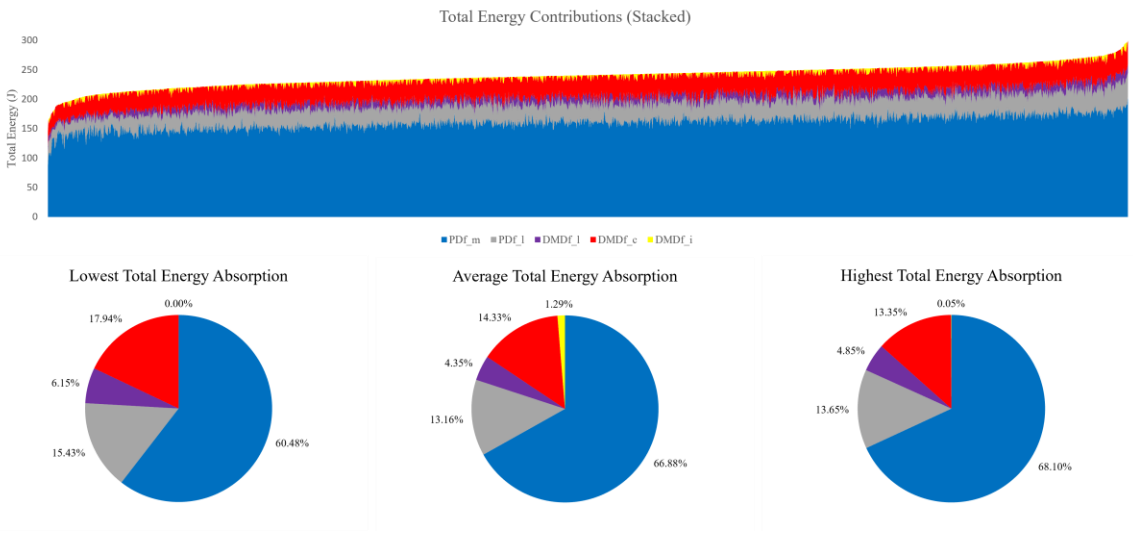


Figure 7-10: Distribution of energies absorbed by the FE model.

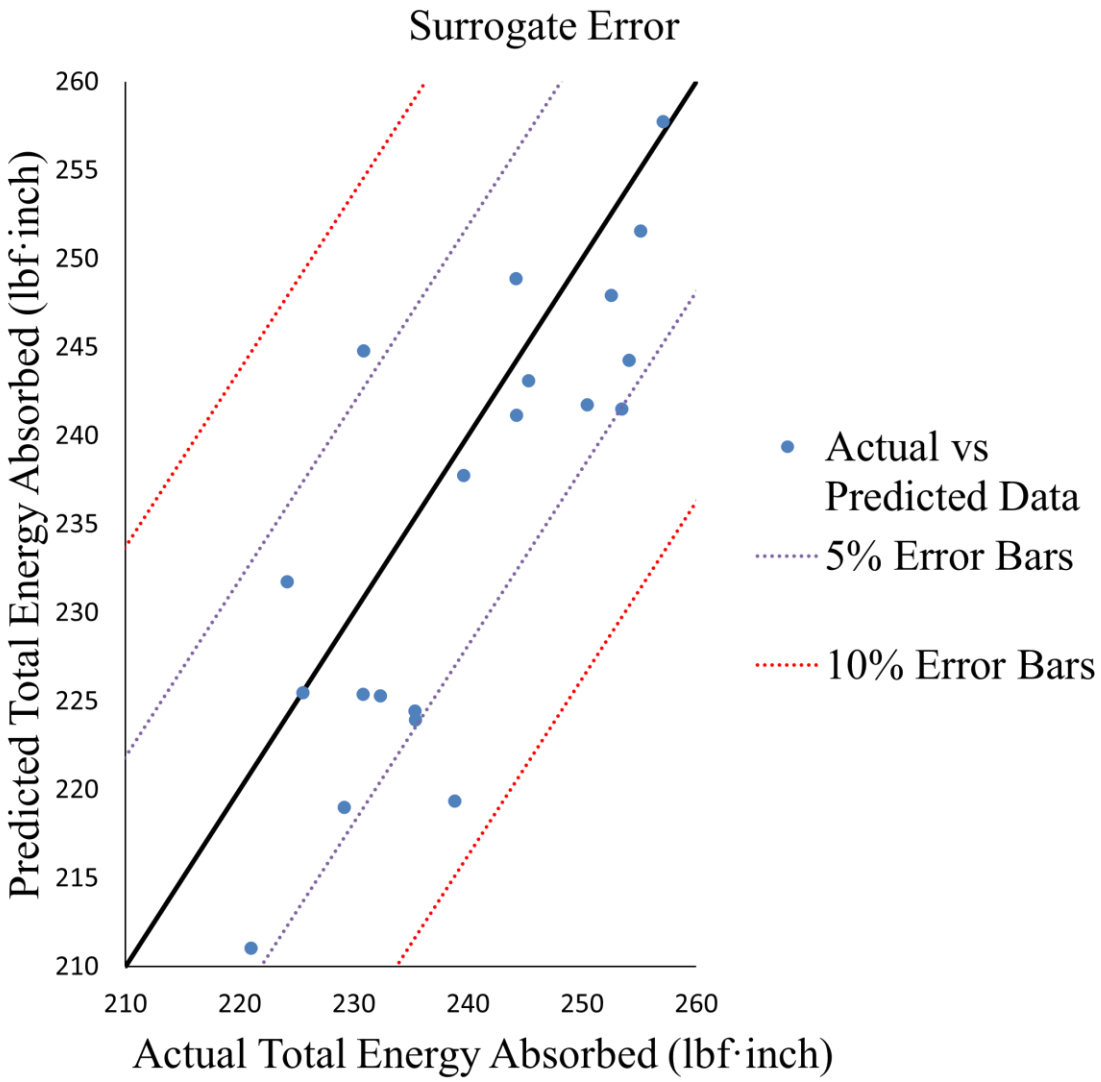


Figure 7-11: Error of 25 randomly selected data points generated by the surrogate model.

GSA of Total Energy Absorption

The generated surrogate model was employed to calculate the first-order and total-order Sobol indices of 41 input parameters with regards to the *Df_T* absorbed. Figure 7-12 displays the first-order vs the total-order indices resulting from this analysis. The Sobol indices showed influence convergence with 10,000 samples.

As previously expected, the properties contributing to the plastic deformation of the aluminum 5456 substrate were some of the most influential. Three of the top four most influential included *A*, *E*, and *Aln* which contribute to the Johnson-Cook plasticity model. Even the remaining parameter *B* is within the eight most influential parameters. Another assumption was the matrix properties would also be influential due to the second and third highest contributing damage mechanisms being controlled by them. This was also confirmed with *XS*, *P*, and *GII* being in the top six most influential parameters. The Sobol indices also showed that there is little to no interaction occurring between the dominant parameters. The results also indicate a large drop of influence between the top four and the remaining parameter space.

The quality of data also needs to be considered. The aluminum 5456 properties that dominate the parameter space, while considered of decent quality, stem from a single cylindrical tensile test specimen. While the properties pertaining to the matrix, *XS* and *P*, where either obtained from sparse experimental data or estimated with similar material properties. The uncertainty in these input parameters need to be gauged to fully explore this parameter space. For the UQ analysis the top five most influential parameters (*A*, *E*, *XS*, *Aln*, and *P*) were evaluated.

The generation of these Sobol indices was manually intensive. As such a more simplistic assessment was approached using the FDR LogWorth and was employed for use with subsections of energies. The FDR LogWorth and the total-order indices highlighted the same parameters as the most influential, and both displayed a drop after the fourth dominant parameter. Table 7-7 illustrates the comparison of these two methods for the *Df_T* absorption of the hybrid configuration.

UQ of Total Energy Absorption

UQ was conducted with the use of a normal distribution Monte Carlo LSS for the five top influential parameters identified by Sobol indices for the *Df_T* absorbed. This included *A*, *E*, *XS*, *Aln*, and *P*. The remaining parameters were kept at a mean value while investigating the space with the surrogate model. To begin only the most dominant parameter, *A*, was altered, followed by the top two and so on until minimal change was predicted with the inclusion of the next parameter. Table 7-8 details the convergence study used to show that 5,000 data points was adequately converged. The highlighted cells show the largest percent difference between the sample sizes. The largest percent difference between 2,5000 samples and 5,000 samples occurred when three parameters are considered and is only 2.04%. The largest percent difference between 5,000 samples and 10,000 samples is observed when five parameters are considered and is 1.01%. It was concluded that the UQ analysis showed convergence with 5,000 samples. Table 7-9 shows the results of the UQ with the introduction of each additional parameter. Similar to the results from the Sobol indices the top four parameters are dominant and have

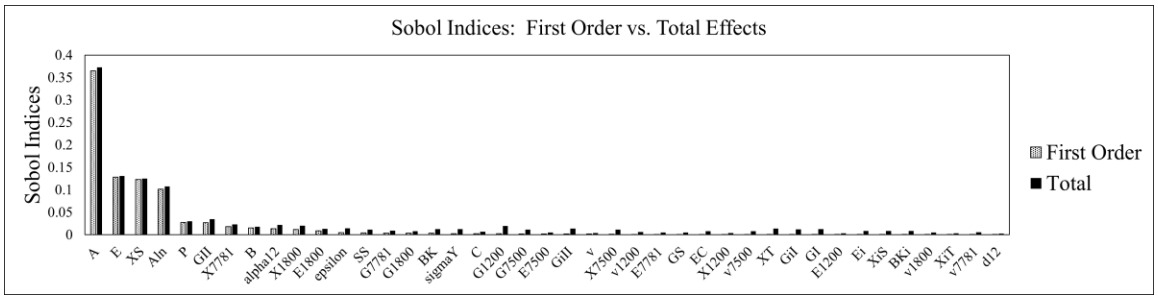


Figure 7-12: Sobol indices for the 41 parameter space.

Table 7-7: Total index vs. FDR LogWorth

Variable	Total Index	FDR LogWorth
A	0.37	59.38
E	0.13	18.67
XS	0.13	12.99
Aln	0.11	12.54
GII	0.03	3.96
P	0.03	3.90

Table 7-8: Convergence study for UQ

Parameters	Total Energy Absorbed (lbf-inch)	2500	% Difference	5000	% Difference	1000
A	mean	234.806	0.001%	234.807	0.000%	234.807
	std	5.849	0.092%	5.843	0.029%	5.845
A, E	mean	234.829	0.000%	234.829	0.000%	234.828
	std	6.846	0.912%	6.784	0.186%	6.771
A, E, XS	mean	234.833	0.001%	234.832	0.080%	234.019
	std	7.504	2.040%	7.353	0.815%	7.413
A, E, XS, Aln	mean	234.912	0.001%	234.914	0.000%	234.914
	std	7.882	1.430%	7.770	0.338%	7.796
A, E, XS, Aln, P	mean	234.921	0.000%	234.921	0.002%	234.925
	std	8.042	1.791%	7.900	1.011%	7.980

Table 7-9: UQ analysis results with 5,000 data points

Variable	Total Energy Absorbed (lbf-inch)	
	Mean	***Std***
A	234.807	5.843
% Difference	0.009%	14.901%
A, E	234.829	6.784
% Difference	0.001%	8.044%
A, E, XS	234.832	7.353
% Difference	0.035%	5.521%
A, E, XS, Aln	234.914	7.770
% Difference	0.003%	1.654%
A, E, XS, Aln, P	234.921	7.900

considerable effects on the predicted *Df_T* absorbed. The mean and standard deviation of the *Df_T* absorbed changes vastly with the introduction of each new variable until the top four have been included. The addition of the fifth parameter, *P*, shows minute changes in the mean and only 1.65% difference in the standard deviation.

Reduced Order Surrogate Modeling with FDR LogWorth

With the *Df_T* absorption characterized it was then possible to evaluate the subsectional energies (*PDf_m*, *PDf_l*, *DMDf_l*, *DMDf_c*, and *DMDf_i*). The subsectional energies were evaluated with FDR LogWorth to determine cutoff points for parameter mapping of their spaces. Table 7-10 and Table 7-11 shows the FDR LogWorth values for each of the five subsectional energies for values considered significant with a p-value of 0.05, FDR LogWorth of 1.3. The objective of FDR LogWorth was to reduce the complexity of our surrogate models for the subsectional energies by allowing for a cutoff threshold of the parameter space. As seen in Table 7-10 and Table 7-11 there are considerable drop offs in the significance after the first few parameters for each of the subsectional energies. For this investigation a FDR LogWorth of 10 was utilized as the cutoff. This resulted in at most three parameters being selected for the parameter mapping of the subsectional energies.

Once the selected parameters were determined for each subsection energy were determined reduced order surrogate models were generated in similar fashion to that of the *Df_T* absorption. Each of the five reduced order surrogate models are detailed in Table 7-10 and Table 7-11.

No surrogate model was generated for the interface disbond (DMDf_i) which showed to be dominated by the parameter P and showed a large drop off before the second parameter. As such, the parameter space used for the mapping of this subsectional energy was performed using 1,220 samples of the initial 1,555 data samples collected.

Due to the lack of data runs and the varying quality of data input, each surrogate model experienced a higher level of error than the *Df_T* surrogate model. The only exception is that of the *PDf_m* which was defined by decent quality data that controlled the overall parameter space. Table 7-12 details the architecture and mean absolute error of 25 saved data samples. As stated, the *PDf_m* was the most consistent model followed by the *DMDf_c*, *PDf_l*, and *DMDf_l* with 2.29%, 4.99%, 6.60%, and 14.45% mean absolute error respectively. While majority of our models fell below 7% error the *DMDf_l* resulted in a significant amount of error, which could be improved with the inclusion of more of the parameter space or reinforcement of the parameters in question. These reduced order surrogate models were then utilized to map their corresponding parameter space.

Parameter Mapping of Total Energy Absorption and Subsectional Energies

To better understand the complex parameter space of the hybrid configuration and highlight potential parameter interactions to assist in composite patch overlay damage tolerance, parameter mapping was achieved with the use 2-dimensional (2D) array

Table 7-10: FDR LogWorth for the three subsection energies

Plastic Deformation in the Al (PDf_m)		**Shear Plasticity in Laminate (PDf_l)**		**Intralaminar Fracture (DMDf_l)**	
Variable	***FDR LogWorth***	***Variable***	***FDR LogWorth***	***Variable***	***FDR LogWorth***
A	100.56	X1800	42.18	XS	25.97
E	45.35	XS	38.01	X7781	18.08
Aln	18.08	E1800	24.83	E1800	11.00
P	6.30	P	8.12	alpha12	7.79
B	3.34	GII	5.14	P	4.74
epsilon	1.86	epsilon	2.74	GII	2.40
C	1.73	G7781	2.57	E7781	1.75
SS	1.33	C	2.43	SS	1.43
		sigmaY	2.11	G1800	1.43
		E1200	1.94		
		X7500	1.37		

Table 7-11: FDR LogWorth for two subsection energies

Interlaminar Delamination (DMDf_c)		**Interface Disbond (DMDf_i)**	
Variable	***FDR LogWorth***	***Variable***	***FDR LogWorth***
E1800	34.86	P	42.18
X1800	14.12	X7500	9.04
P	6.68	epsilon	8.25
alpha12	5.36	XiS	6.83
G1800	4.55	GS	5.93
X7781	4.49	GiII	3.35
X1200		C	2.91
SS	3.91	XS	2.67
E1200	2.20	E7500	2.60
XS	2.18	GII	2.18
A	1.96	E1200	1.80

Table 7-12: Reduced order surrogate results for the five subsection energies

Plastic Deformation in the Al (PDf_m)		**Shear Plasticity in Laminate (PDf_l)**		**Intralaminar Fracture (DMDf_l)**		**Interlaminar Delamination (DMDf_c)**	
Layers / Nodes	***MAE***	***Layers / Nodes***	***MAE***	***Layers / Nodes***	***MAE***	***Layers / Nodes***	***MAE***
2 / 60-80	2.29	2 / 65-70	6.60	2 / 55-55	14.45	1 / 50	4.99

graphing and 3-dimensional (3D) contour graphing. The 2D arrays were generated with 25,000 random uniform data sets acquired through DICE. The 3D contour graphs were generated with the use of a 3D mesh grid consisting of 9,261 data sets to cover the design space in a uniform systematic fashion. When inspecting the 3-D contour plots the third parameters is always at its minimum value. It's effect on the parameter space can still be induced by the maximum energy of the plots. The *Df_T* surrogate and subsectional energy surrogate models were utilized to predict the outputs. The following parameter maps detail the influential parameters within this complex parameter space for each energy being explored. It should be noted that the error from each previous step of the nondeterministic process has propagated to this analysis. No smoothing was performed for these graphs.

Df_T Absorption Parameter Mapping

The *Df_T* absorption of the hybrid configuration was dominated by four parameters (*A*, *E*, *XS*, and *Aln*) as previously shown. To investigate their relationships a 4-dimensional parameter space visualization was graphed with the use of 2D contour plots contoured with the *Df_T* absorbed. Figure 7-13 shows the 2D array for two input parameters. The 2D plots along the diagonal illustrate each of the selected input parameters against the *Df_T* absorbed. As detailed with Sobol indices there is minimal interaction between the four dominant parameters. This is detailed by the near linear gradation in the *Df_T* absorbed.

PDf_m Absorption Parameter Mapping

The first subsectional energy to be explored was the *PDf_m*. Figure 7-14 illustrates the 3D mesh contour for the controlling parameters (*A*, *E*, and *Aln*). The results agree with the FDR_Logworth with *A* being the dominant parameter in *PDf_m*. No interactions between the parameters can be inferred by the plots. The metal substrate absorbs more energy when it's a stiffer less formable metal. Increasing the yield stress and stiffness prior to the onset of plastic deformation and decreasing the metals formability (Aln), will result in less deformation in the plastic region. This allows the metal to absorb more of the energy before the outer composite overlay plies fail due to stress build up.

PDf_l Absorption Parameter Mapping

PDf_l highlights the shear plasticity of the composite overlay. As seen in Figure 7-15 there are two distinct regions in regard to the energy absorbed. The lower region is dominated by low values of *E1800* and *XS* and high values of *X1800*. The higher energy region corresponds to high values of *E1800* and *XS* and low values of *X1800*. As the mesh grid is swept interaction between the three parameters can be observed, with more interaction between *E1800* and *XS*.

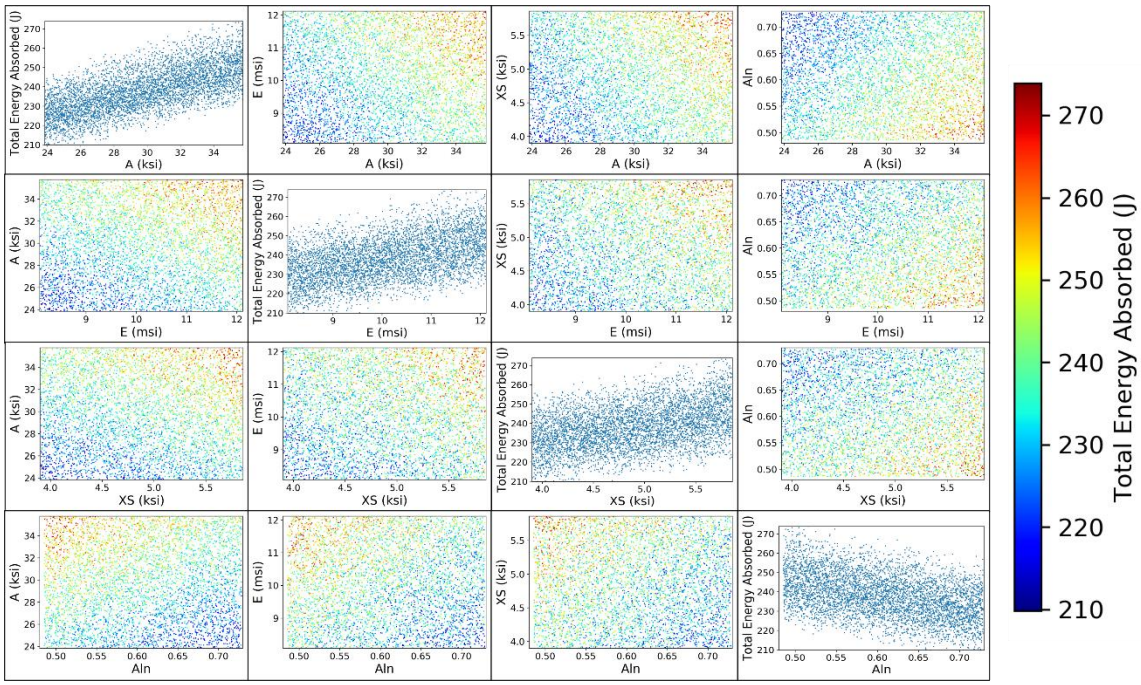


Figure 7-13: 4-dimensional parameter space visualization contoured with the total energy absorbed.

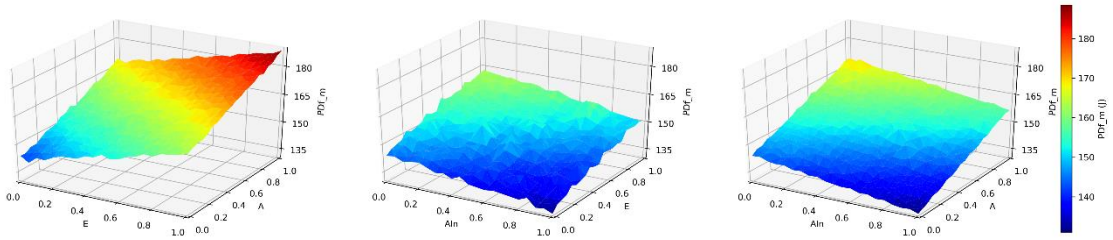


Figure 7-14: 3-D mesh contours for plastic deformation in the aluminum substrate.

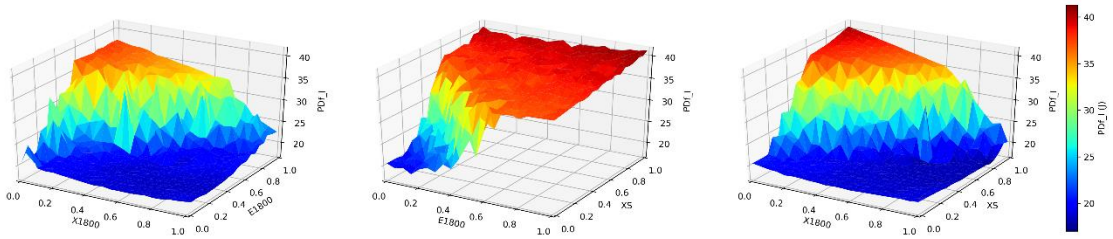


Figure 7-15: 3-D mesh contours for shear plasticity in the composite overlay.

DMDf_l Absorption Parameter Mapping

Figure 7-16 highlights the dominant parameters for the subsection energy *DMDf_l*. The interlaminar fracture of the composite overlay is controlled by shear stress of the resin matrix, *XS*. This is noted by the large change in energy along its axis compared to the other two parameters, *X7781* and *E1800*. A higher *XS* requires a larger amount of energy for the damage to propagate through the laminae layers. This is mirrored with the tensile strength of the Hexcel 7781 layer, the outside ply, and *E1800* corresponding to the interior layers left carrying the stress after the outer plies fail. Interacting parameters are observed yet again with *XS* and *E1800* showing more interaction than *X7781* does with either.

DMDf_c Absorption Parameter Mapping

Figure 7-17 shows the two dominant parameters with respect to the *DMDf_c*. The delamination between the plies is controlled by the interior ELT-1800 plies. As the stiffness of the plies is decreased more deformation occurs leading to the resin needing to carry a larger stress. Large amounts of delamination occurs with low *E1800* and high X*1800*.

DMDf_i Absorption Parameter Mapping

The final subsectional energy is the disbond between the metal and composite interface. Even without the use of a surrogate model it was vital to investigate the relationship between the most influential parameters regarding the disbond. This particular subsectional energy was difficult to quantify and this approach lent detail to the case. Figure 7-18 shows one set of parameters, *P* and *epsilon*, mapped from the original 1,555 data samples compared to the *DMDf_i*. This pattern prevailed throughout the space. Further investigation of the FDR_Logworth of the *DMDf_i* was deemed necessary to assist in quantifying this subsectional energy.

GSA for Subsectional Energies with Reduced Order Models

The parameter mapping of the subsectional energies performed with the 3-D contour graphs informed that majority of the subsectional energies had interacting parameters. To further investigate these interactions, GSA was performed with the use of Sobol indices. The reduced order surrogate models previously generated were employed again to generate the necessary data.

GSA for PDf_m

Figure 7-19 details the Sobol indices for the *PDf_m*. As observed with the 3-D contour plots there is no notable interaction between the three dominant parameters. This figure also agrees with the FDR_Logworth values with *A* being the dominant parameter followed by *E* and *Aln* respectively.

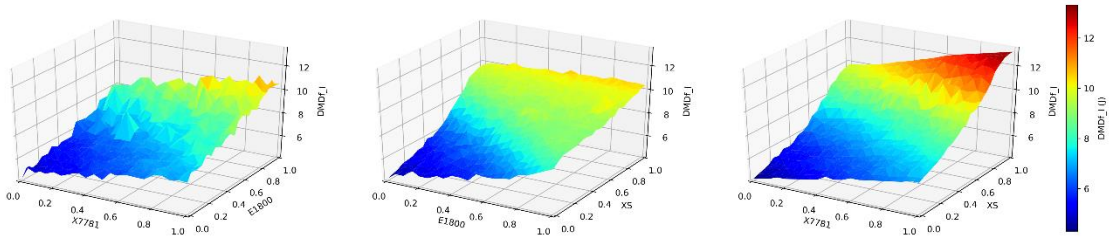


Figure 7-16: 3-D mesh contours for interlaminar fracture in the composite overlay.

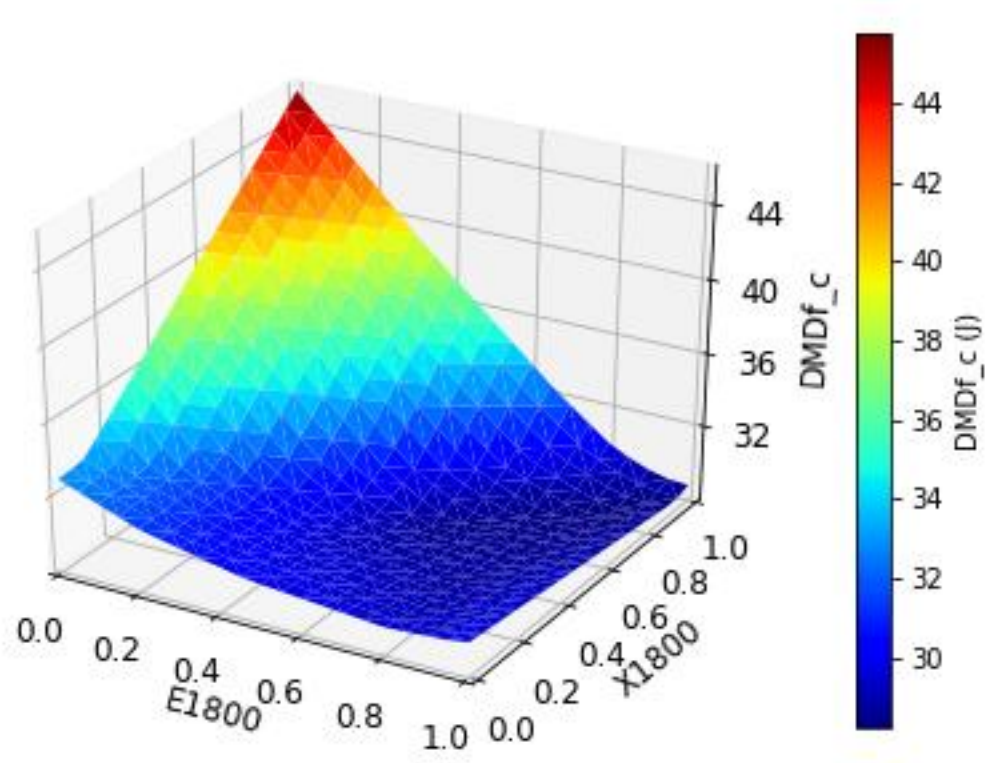


Figure 7-17: 3-D mesh contours for intralaminar delamination in the composite overlay.

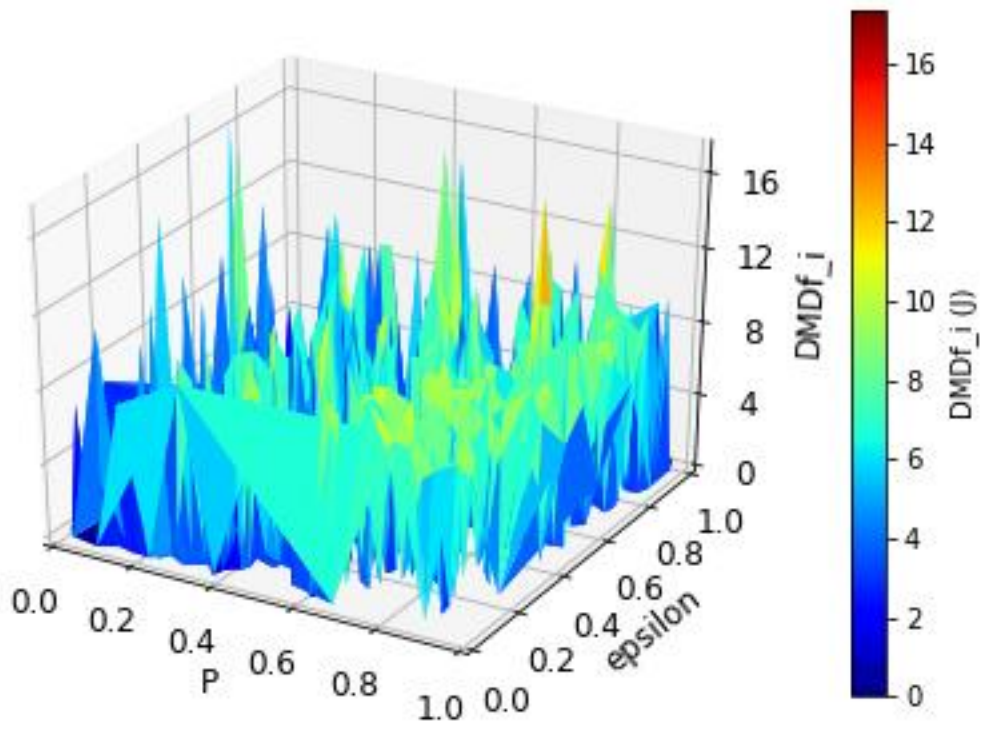


Figure 7-18: 3-D mesh contours for interface disbond between the metal substrate and the composite overlay.

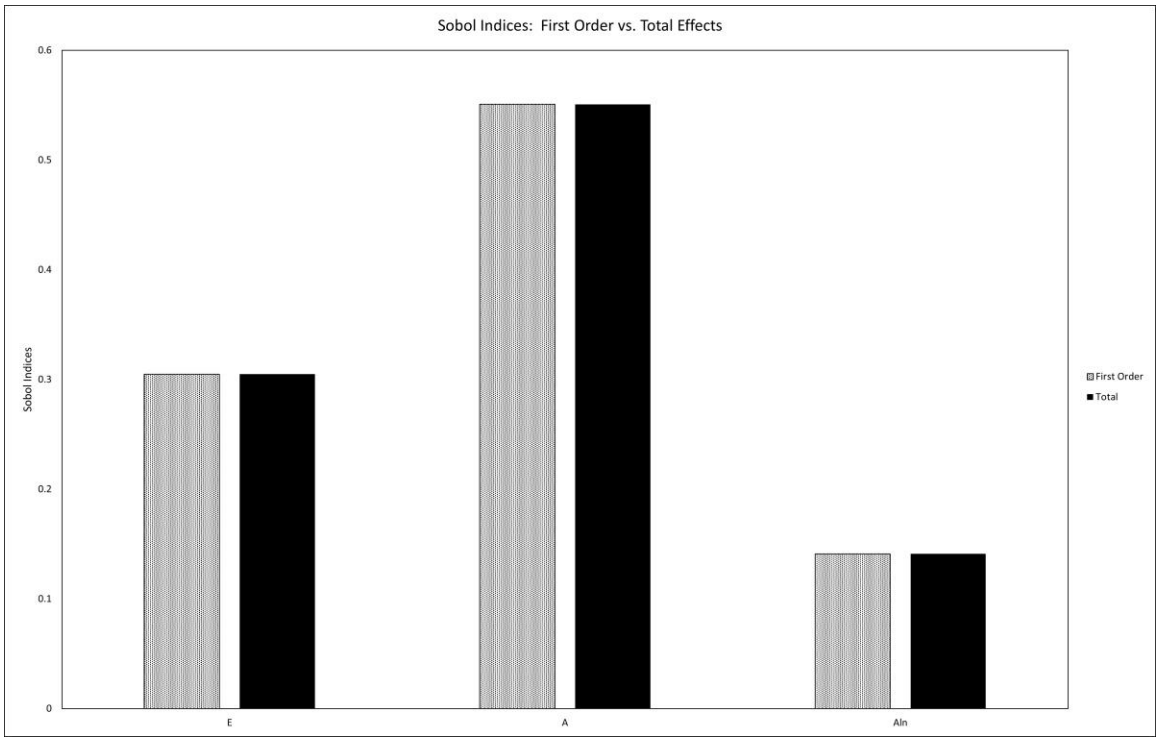


Figure 7-19: Sobol indices for plastic deformation in the aluminum substrate.

GSA for PDf_l

PDf_l's Sobol indices are seen in Figure 7-20 where the expected interactions between it's dominant parameters are confirmed as well. While all three parameters show interaction, *E1800* and *XS* detail higher total order effects than *X1800*. These values also confirm with the FDR_Logworth and 3-D contour when investigating the most influential.

GSA for DMDf_l

Figure 7-21 highlights the Sobol indices for *DMDf_**l***. Again the results agree with both those of the parameter mapping and the FDR_Logworth. Agreement with both the level of interaction and influence of the three parameters is noted. *XS* has the most influence and interacts with *E1800* on a higher degree than that of *X7781*.

GSA for DMDf_c

The Sobol indices for *DMDf_c* are shown in Figure 7-22. Figure 7-22 informs that the two dominant parameters, *E1800* and X*1800*, interact. The Sobol indices also reinforce the FDR_Logworth with low *E1800* controlling with a significantly higher first and total index.

Equational Comparison of the Total Energy Absorption to the Reduced Order Subsectional Energies

The final facet of this investigation was to compare the *Df_T* absorption of the full parameter space to that of a combination of the reduced order subsectional energies. To accomplish this the initial FE predictions of the saved 25 samples used to observe the surrogate models' error and the *Df_T* surrogate's prediction were compared to the summation of the reduced order subsectional energy surrogates predictions. Since the *DMDf_i* was not able to be represented with a surrogate model, two comparisons were made. The first is detailed in Table 7-13 and shows the percent error of the summation with the interface contribution added from the FE model results. While Table 7-14 shows the percent error of the summation without the interface contribution factored in. The difference between the results with and without the interface contribution is to an acceptable degree with the max difference in percent error of the mean being 0.67%. Thus, for this configuration of loading the interface reduced order surrogate model is not required. Regardless of the inclusion of the interface contribution, the percent error of the reduced order approach was less than 3.5% and 2.3% for the mean and standard deviation when looking at both the FE or the *Df_T* surrogate. This highlights that the reduced order surrogate models generated by the investigation of the FDR_Logworth was a valid approach to exploring the complex 41 parameters space in more efficient manner.

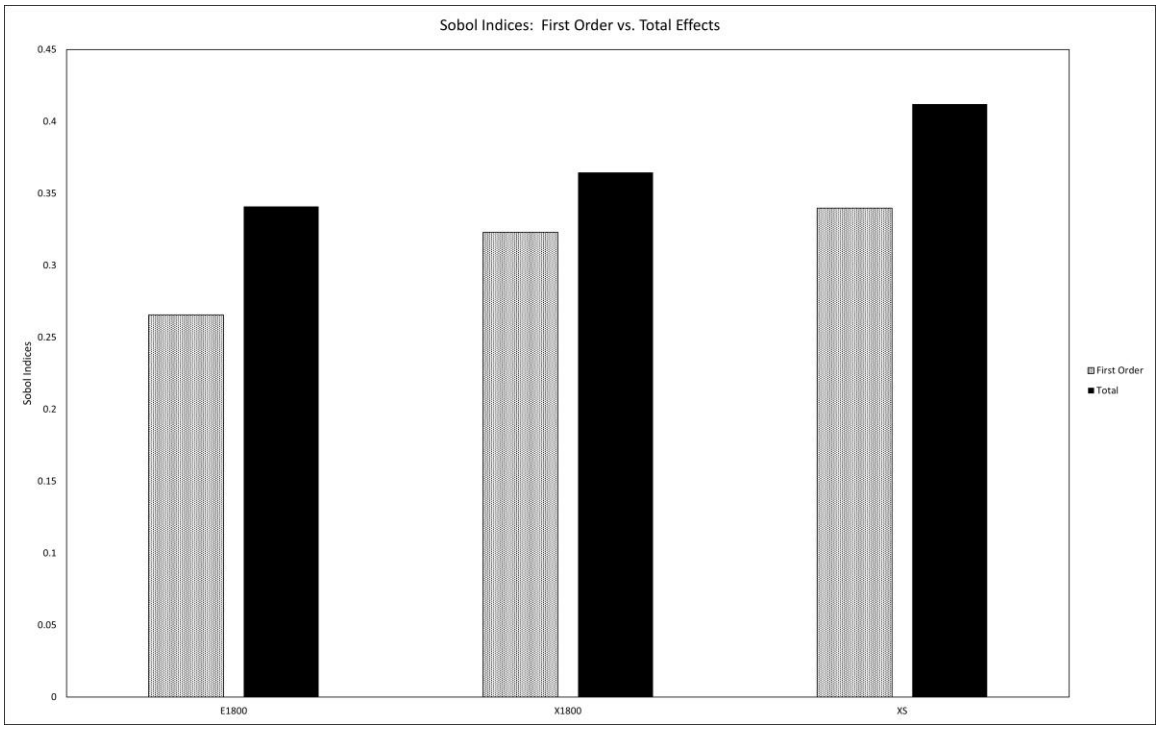


Figure 7-20: Sobol indices for shear plasticity in the composite overlay.

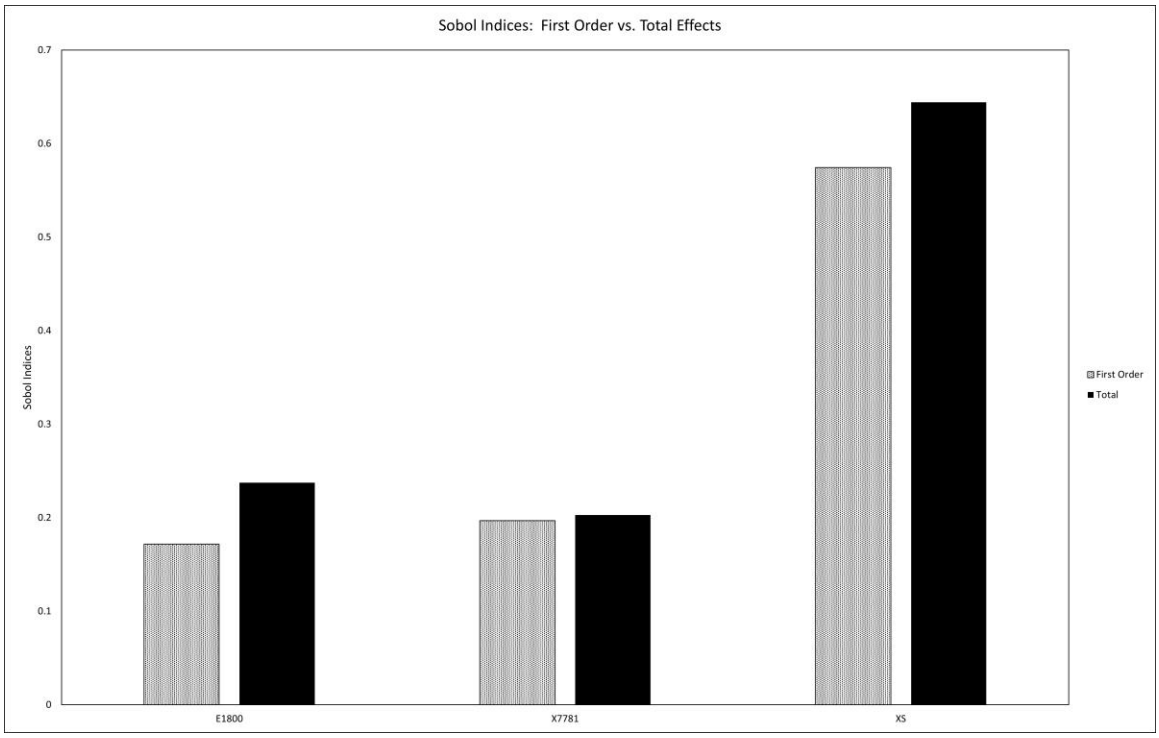


Figure 7-21: Sobol indices for interlaminar fracture in the composite overlay.

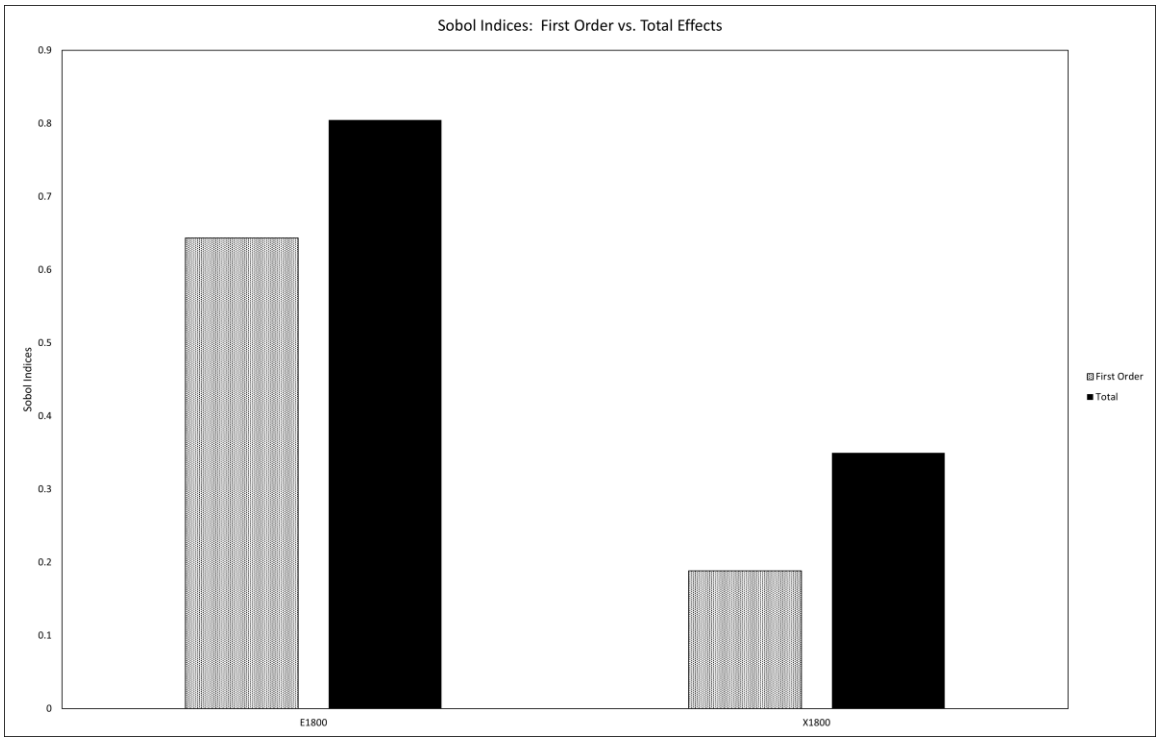


Figure 7-22: Sobol indices for intralaminar delamination in the composite overlay.

Table 7-13: Reduced Order Modeling Error with Interface Contribution

	Total Energy Absorbed (lbf-inch)		**Reduced Surrogates with Interface Contribution**		
	FE	***Total Surrogate***	***ROM Surrogate***	***% Error FE***	***% Error Total Surrogate***
Mean	245.79	244.38	243.78	2.43%	2.74%
Stdv	15.92	14.93	11.55	1.31%	2.21%

Table 7-14: Reduced Order Modeling Error without Interface Contribution

	Total Energy Absorbed (lbf-inch)		**Reduced Surrogates without Interface Contribution**		
	FE	***Total Surrogate***	***ROM Surrogate***	***% Error FE***	***% Error Total Surrogate***
Mean	245.79	244.38	239.38	3.10%	2.62%
Stdv	15.92	14.93	12.33	1.91%	2.17%

Conclusion

This study integrated experimental testing, computational modeling, and a non-deterministic approach with parameter mapping to investigate and characterize the complex parameter space required to define the damage tolerance of a composite/metal hybrid structure under four-point bending. The validated high-fidelity FE model sufficiently sampled the parameter space allowing the generation of adequate surrogate models for further exploration of the parameter space to investigate the many damage mechanisms including; matrix cracking, fiber breakage, delamination within the composite, disbond at the composite/metal interface, and yielding in the metal. The non-deterministic approaches including GSA, UQ, and data visualization illustrated the most influential parameters were inherently known for the *Df_T* absorption. FDR LogWorth helped highlight the subsectional energy spaces with more efficiency and allowed for the investigation of these important aspects of the hybrid's interacting damage mechanisms. Reduced order modeling also proved to be an effect approach to investigation the subsectional energies to further understand the complex parameter spaces.

Chapter Eight

Conclusions and Recommendations

The environmental impact humanity imposes on the Earth is of great concern and is ever expanding. Each sector of civilization needs to address this concern and can do so with innovation in greener technology. Somers and his collaborators have demonstrated that the introduction of natural-laminar-flow (NLF) can assist in meeting fuel reduction goals and reduce the aerospace contribution to global carbon emissions. Somers has developed the slotted, natural-laminar-flow (SNLF) airfoil to further expand the benefits of NLF and predicts a 90% envelopment of the airfoil with NLF. As discussed, the introduction of this slot creates several challenging aspects that need to be considered for future implementation onto commercial aircraft. This dissertation focused on the connectors required to transfer the high-lift load from the aft element to the fore element. It addressed the slot connectors placement and number within the slot, their size and shape, the material choices, and their effects on the remaining structural components. Topology optimization of the aft element was utilized to investigate the structural elements required to transfer the lift through the slot connectors to the fore element. A half-span demonstration provided insight into how the global model would behave with the high-lift 'floating' aft element and the slot connectors. Finally, a study was performed to access potential adhesive bonding with composites with the goal of reducing the weight contribution needed to support this developing SNLF technology.

Chapter Four utilized structural mechanics, finite element (FE) modeling, and computational fluid dynamics (CFD) to investigate the shape, location, and number of connectors with the half-span of the S207 SNLF airfoil. The results from this chapter from this came from multiple studies and informed the preferred slot connector aspects with regards to structural and aerodynamic factors. The resulting slot connectors were internally placed near the upper region of the slot and were materialized with Ti-6Al-4V to provide high strength with low density. However, no determining benefit was observed as the number of connectors across the half-span was increased. The remaining studies combined flutter results from Bottai et al. to set the minimum number of slot connectors with the location and size from the studies performed in this dissertation.

Topology optimization was performed in Chapter Five to determine material distribution with the 'floating' aft element. The goal was to reduce the overall weight of the aft element while ensuring the transfer of the lift induced to the slot connectors. Another constraint was to maintain the slot during cruise loading conditions. This was achieved by placing volume and displacement controls on the aft element design area. A comparison between the displacement-controlled topology optimization with a displacement-relaxed topology optimization highlighted confirmed that ribs were formed underneath the slot connectors with stiffened material between these spans being required to control the collapse of the slot.

Chapter Six demonstrated the global response of the fore and aft element of the S207 SNLF airfoil for a half-span model. Previous considerations from the slot connectors and topology optimization of the aft influenced the initial structural sizing of the fore element spars, ribs, and skin panels along with the aft element ribs and skin

panels. Overall, the global response was as predicted and showed that the slot connectors could transfer the lift induced by the aft element while maintaining the slot width during cruise loading.

Chapter 7 provided insight into the damage mechanisms that can be expected from adhesive joining. Reduced order modeling of the hybrid structure demonstrated that the complex parameter space could be simplified to better understand what damage mechanism would control for a giving loading scenario and how best to approach the design of the composite to reflect this. With this evaluation the adhesive joining of the connectors to the aft element skin could provide weight reduction when compared to traditional connections. It was noted that the controlling material properties related to the substrate and the resin shear properties.

From this dissertation the author has highlighted the importance of these slot connectors and provided methods to design them for future implementation of future iterations of the SNLF airfoil. Suggested methods include multi-disciplinary optimization of the slot connectors with respect to structural and aerodynamic considerations. This will ensure to minimize the weight of the connectors while ensuring to reduce their global impedance on the laminar flow through the slot. As with aerospace designs, the iteration process of the internal structures will continue throughout the design process as adjustments are made to the number and location of slot connectors or geometry of the wing itself. This includes the analysis of multiple critical loading scenarios that need to be investigated to design the internal structures.

List of References

1. *FAA Aerospace Forecast Fiscal Years 2019-2039*. 2019, Federal Aviation Administration.
2. *FAA Aerospace Forecast Fiscal Years 2020-2040*. 2020, Federal Aviation Administration.
3. *FAA Aerospace Forecast Fiscal Years 2021-2041*. 2021, Federal Aviation Administration.
4. *FAA Aerospace Forecast Fiscal Years 2022-2042*. 2022, Federal Aviation Administration.
5. Somers, D.M., *Design of a Slotted, Natural-laminar-flow Airfoil for a Transport Aircraft*. 2019.
6. Somers, D.M., *Laminar-flow airfoil*. 2005: US.
7. Maughmer, M.D., J.G. Coder, and D.M. Somers. *Exploration of a slotted, natural-laminar-flow airfoil concept*. in *2018 Applied Aerodynamics Conference*. 2018.
8. Kumpatla, S.K., C.M. Arndt, and S.C. Termaath, *Slotted, Natural-Laminar-Flow Airfoil: A Revolutionary Technology for Fuel Efficiency.* In Preparation, 2022.
9. Bradley, M. and C. Droney, *Subsonic ultra green aircraft research: phase I final report. Report.* National Aeronautics and Space Administration, USA, 2011.
10. Greitzer, E.M., et al., *N+ 3 aircraft concept designs and trade studies, final report.* Nasa cr-2010-216794/vol2, NASA Glenn Research Center, Cleveland, Ohio, 2010. **44135**.
11. Somers, D.M., *Design and experimental results for a flapped natural-laminar-flow airfoil for general aviation applications*. 1981.
12. Whitcomb, R.T. and L.R. Clark, *An airfoil shape for efficient flight at supercritical Mach numbers*. 1965.
13. Bertelrud, A. *Transition on a three-element high lift configuration at high Reynolds numbers*. in *36th AIAA Aerospace Sciences Meeting and Exhibit*. 1998.
14. Smith, A.M., *High-lift aerodynamics.* Journal of Aircraft, 1975. **12**(6): p. 501-530.
15. Somers, D.M., *An exploratory investigation of a slotted, natural-laminar-flow airfoil*. 2012.
16. *Boundary Layer*. Available from: https://www.grc.nasa.gov/WWW/BGH/boundlay.html.
17. Saric, W.S. and H.L. Reed, *STABILITY AND TRANSITION OF TIIREE-DIMENSIONAL BOUNDARY LAYERS.* Fluid Dynamics of Three-Dimensional Turbulent Shear Flows and Transition, 1989: p. 11.
18. *Wings and Configurations for High-Speed Flight*. Quest for Performance: The Evolution of Modern Aircraft; Available from: https://history.nasa.gov/SP-468/ch10-4.htm.

19. Coder, J.G. and D.M. Somers, *Design of a slotted, natural-laminar-flow airfoil for commercial transport applications.* Aerospace Science and Technology, 2020. **106**: p. 106217.
20. Rivers, M.B., et al. *Experimental investigation of the nasa common research model with a natural laminar flow wing in the nasa langley national transonic facility*. in *AIAA Scitech 2019 Forum*. 2019.
21. Coder, J.G., M.D. Maughmer, and D.M. Somers, *Theoretical and experimental results for the S414, slotted, natural-laminar-flow airfoil.* Journal of Aircraft, 2014. **51**(6): p. 1883-1890.
22. Jacobs, E.N. and W.C. Clay, *Characteristics of the NACA 23012 airfoil from tests in the full-scale and variable-density tunnels*. 1936.
23. Jacobs, E.N., *Preliminary report on laminar-flow airfoils and new methods adopted for airfoil and boundary-layer investigations*. 1949, NATIONAL AERONAUTICS AND SPACE ADMIN LANGLEY RESEARCH CENTER HAMPTON VA.
24. Wenzinger, C.J., *Pressure distribution over an NACA 23012 airfoil with an NACA 23012 external-airfoil flap*. 1938, US Government Printing Office.
25. Abbott, I.H., A.E. Von Doenhoff, and L. Stivers Jr, *Summary of airfoil data*. 1945.
26. Theodorsen, T., *Theory of wing section of arbitrary shape, National Advisory Committee for Aeronautics*. 1931, Report.
27. Whitcomb, R.T. *Review of NASA supercritical airfoils*. in *International Council of the Aeronautical Sciences Congress*. 1974.
28. Talay, T.A., *Introduction to the Aerodynamics of Flight*. 1975.
29. McGhee, R.J., *Low-speed aerodynamic characteristics of a 17-percent-thick medium speed airfoil designed for general aviation applications*. 1980: National Aeronautics and Space Administration, Scientific and Technical ….
30. McGhee, R.J., W.D. Beasley, and R.T. Whitcomb. *NASA low-and medium-speed airfoil development*. in *NASA Conf. on Advanced Tech. Airfoil Res.* 1979.
31. Somers, D.M., *Subsonic Natural-Laminar-Flow Airfoil*, in *Natural laminar flow and laminar flow control*. 2012, Springer Science & Business Media.
32. Selig, M.S., M.D. Maughmer, and D.M. Somers, *Natural-laminar-flow airfoil for general-aviation applications.* Journal of aircraft, 1995. **32**(4): p. 710-715.
33. Somers, D.M., *Design of a slotted, natural-laminar-flow airfoil for business-jet applications*. 2012.
34. Somers, D.M. and M.D. Maughmer, *Design and experimental results for the S414 airfoil*. 2010, AIRFOILS INC PORT MATILDA PA.
35. Coder, J.G., *Design of Low-Speed Slotted, Natural-Laminar-Flow Airfoil Reproducing Transonic Behaviors.* Journal of Aircraft, 2021. **58**(3): p. 526-535.
36. Somers, D.M., *Discussion on SNLF Airfoils*, S. Kumpatla, Editor.

37. Eppler, R., *Airfoil data*, in *Airfoil Design and Data*. 1990, Springer. p. 163-512.
38. Eppler, R., *Airfoil program system "PROFIL00." user's guide. Richard Eppler.* 2000.
39. Drela, M., *A User's Guide to MSES 2.95.* Massachusetts Institute of Technology, Cambridge, MA, 1996.
40. *The University Leadership Initiative (ULI)*. Available from: https://nari.arc.nasa.gov/uli.
41. *NASA University Leadership Initiative*. Available from: https://nasa-uli.utk.edu/.
42. Ortiz-Melendez, H.D., J.G. Coder, and A. Shmilovich. *High-Lift Simulations of Slotted, Natural-Laminar-Flow Airfoils*. in *AIAA Scitech 2019 Forum*. 2019.
43. Schmitz, S., *Drag Decomposition Using Partial-Pressure Fields in the Compressible Navier–Stokes Equations.* AIAA journal, 2019. **57**(5): p. 2030-2038.
44. *Abaqus 6.14*. 2014, Dassault Systems Simulia Corp.: Providence, RI.
45. Bottai, A., R.L. Campbell, and M.L. Jonson. *Vibrations of a High-Aspect-Ratio, Multi-Element Wing*. in *AIAA SCITECH 2022 Forum*. 2022.
46. Yoder, S., et al., *Characterization of topology optimized Ti-6Al-4V components using electron beam powder bed fusion.* Additive Manufacturing, 2018. **19**: p. 184-196.
47. Colletti, C., V.G. Awate, and P.J. Ansell. *Effect of geometric parameters and flow conditions on the frequency of fluidic oscillators for active flow control*. in *AIAA Scitech 2019 Forum*. 2019.
48. Awate, V.G. and P.J. Ansell. *Characterization of Inclined Oscillating Jet and Crossflow Interaction for Use in Active Flow Control*. in *AIAA Scitech 2020 Forum*. 2020.
49. Colletti, C., A. Shmilovich, and A. Khodadoust. *Flow Control for Enhanced High-Lift Performance of Slotted Natural Laminar Flow Wings*. in *AIAA Scitech 2021 Forum*. 2021.
50. Bottai, A.M., M.L. Jonson, and R.L. Campbell. *Investigation of the role of higher order torsion & bending modes in flutter stability for flexible slender wings*. in *AIAA Aviation 2019 Forum*. 2019.
51. Anderson, J.D., *Aircraft performance and design*. Vol. 1. 1999: WCB/McGraw-Hill Boston.
52. Coder, J.G., *Discussion on Aerodynamic Center and Center of Pressure*, C.M. Arndt, Editor. 2022.
53. Baweja, C., et al. *Analysis and optimization of dimpled surface modified for wing planforms*. in *2016 7th International Conference on Mechanical and Aerospace Engineering (ICMAE)*. 2016. IEEE.
54. Spaid, F.W. and R.J. Hakkinen, *On the boundary layer displacement effect near the trailing edge of an aft-loaded airfoil.* Zeitschrift für angewandte Mathematik und Physik ZAMP, 1977. **28**(5): p. 941-950.

55. Sriram, P., A. Gopalarathnam, and A. Misenheimer, *High-Downforce Airfoil Design for Motorsports.* SAE International Journal of Materials and Manufacturing, 2012. **5**(2): p. 478-489.
56. Selig, M.S. and J.J. Guglielmo, *High-lift low Reynolds number airfoil design.* Journal of aircraft, 1997. **34**(1): p. 72-79.
57. Liebeck, R.H., *Subsonic airfoil design.* Applied computational aerodynamics, 1990. **125**: p. 501-530.
58. U.S. Department of Transportation, F.A.A., Flight Standards Service, *Pilot's Handbook of Aeronautical Knowledge*. 2016, AFS-630, P.O. Box 25082, Oklahoma City, OK 73125: U.S. Department of Transportation, Federal Aviation Administration, Airman Testing Standards Branch.
59. Zhang, G., et al. *The Design of Static Test Scheme for Composite Aileron Structure of Large Aircraft*. in *IOP Conference Series: Materials Science and Engineering*. 2021. IOP Publishing.
60. Qiao, G., et al., *A review of electromechanical actuators for More/All Electric aircraft systems.* Proceedings of the Institution of Mechanical Engineers, Part C: Journal of Mechanical Engineering Science, 2018. **232**(22): p. 4128-4151.
61. Keller, D., *High-lift design for a forward swept natural laminar flow wing.* CEAS Aeronautical Journal, 2020. **11**(1): p. 81-92.
62. Janker, P., et al. *New actuators for aircraft and space applications*. in *11th International Conference on New Actuators, Bremen, Germany*. 2008.
63. Barbarino, S., et al., *A review of morphing aircraft.* Journal of intelligent material systems and structures, 2011. **22**(9): p. 823-877.
64. Hartwich, P.M., et al., *AFC-enabled simplified high-lift system integration study*. 2014.
65. Michell, A.G.M., *LVIII. The limits of economy of material in frame-structures.* The London, Edinburgh, and Dublin Philosophical Magazine and Journal of Science, 1904. **8**(47): p. 589-597.
66. Drucker, D.C. and W. Prager, *Soil mechanics and plastic analysis or limit design.* Quarterly of applied mathematics, 1952. **10**(2): p. 157-165.
67. Dorn, W., *Automatic design of optimal structures.* J. de Mecanique, 1964. **3**: p. 25-52.
68. Bendsøe, M.P. and N. Kikuchi, *Generating optimal topologies in structural design using a homogenization method.* Computer methods in applied mechanics and engineering, 1988. **71**(2): p. 197-224.
69. Verbart, A., *Topology optimization with stress constraints.* 2015.
70. Krog, L., A. Tucker, and G. Rollema. *Application of topology, sizing and shape optimization methods to optimal design of aircraft components*. in *Proc. 3rd Altair UK HyperWorks users conference*. 2002.
71. Walker, D. and D. Liu. *Topology optimization of an aircraft wing*. in *56th AIAA/ASCE/AHS/ASC Structures, Structural Dynamics, and Materials Conference*. 2015.

72. Yang, R. and A. Chahande, *Automotive applications of topology optimization.* Structural optimization, 1995. **9**(3): p. 245-249.
73. James, K. and J.R. Martins. *Three-dimensional structural topology optimization of an aircraft wing using level set methods*. in *12th AIAA/ISSMO Multidisciplinary Analysis and Optimization Conference*. 2008.
74. Dunning, P.D., B.K. Stanford, and H.A. Kim, *Coupled aerostructural topology optimization using a level set method for 3D aircraft wings.* Structural and Multidisciplinary Optimization, 2015. **51**(5): p. 1113-1132.
75. Munk, D.J., D. Verstraete, and G.A. Vio, *Effect of fluid-thermal–structural interactions on the topology optimization of a hypersonic transport aircraft wing.* Journal of Fluids and Structures, 2017. **75**: p. 45-76.
76. Félix, L., A.A. Gomes, and A. Suleman, *Topology optimization of the internal structure of an aircraft wing subjected to self-weight load.* Engineering Optimization, 2020. **52**(7): p. 1119-1135.
77. Zhu, J.-H., W.-H. Zhang, and L. Xia, *Topology optimization in aircraft and aerospace structures design.* Archives of Computational Methods in Engineering, 2016. **23**(4): p. 595-622.
78. Abaqus, V., *6.14 Documentation.* Dassault Systemes Simulia Corporation, 2014. **651**(6.2).
79. Bendsoe, M.P. and O. Sigmund, *Topology optimization: theory, methods, and applications*. 2003: Springer Science & Business Media.
80. Bendsøe, M.P., *Optimization of structural topology, shape, and material*. Vol. 414. 1995: Springer.
81. Coder, J.G. *Design of a slotted, natural-laminar-flow airfoil for transition validation experiments*. in *AIAA Scitech 2020 Forum*. 2020.
82. Arndt, C.M., D.L. Stefanski, and S.C. TerMaath. *Investigation of Fore-Aft Element Connectors for a Slotted, Natural-Laminar-Flow Airfoil*. in *AIAA SCITECH 2021 Forum*. 2021. Virtual.
83. Young, T.M., *Performance of the Jet Transport Airplane: Analysis Methods, Flight Operations, and Regulations*. 2017: John Wiley & Sons.
84. *Aluminum 6061-T6; 6061-T651*. Material Property Data].
85. *AutoCAD*. 2021, Autodesk, Inc.
86. Stefanski, D.L., et al. *Development of a Predictive Capability for Laminar-Turbulent Transition in HPCMP CREATETM-AV Kestrel Component COFFE using the Amplification Factor Transport Model*. in *2018 AIAA Aerospace Sciences Meeting*. 2018.
87. Stefanski, D.L., et al. *Improvements to the Amplification Factor Transport Transition Model for Finite-Element Implementations*. in *AIAA Scitech 2019 Forum*. 2019.
88. Glasby, S. and J. Erwin, *Introduction to COFFE: The Next Generation HPCMP CREATE-AV CFD Flow Solver.* AIAA Paper, 2016. **1054**.

89. Center, N.L.R. *CRM.65.AIRFOIL SEctions*. Common Research Model 2012; Available from: https://commonresearchmodel.larc.nasa.gov/crm-65-airfoil-sections/.
90. *XFOIL Subsonic Airfoil Development System*. 2013, Free Software Foundation, Inc.
91. *Titanium Ti-6Al-4V (Grade 5), Annealed*. Material Property Data]. Available from: https://asm.matweb.com/search/SpecificMaterial.asp?bassnum=mtp641.
92. NASA. *Shape Effects on Drag*. 2021; Available from: https://www.grc.nasa.gov/www/k-12/airplane/shaped.html.
93. *ASTM A36 Steel, bar*. Material Property Data]. Available from: https://www.matweb.com/search/datasheet.aspx?matguid=d1844977c5c8440cb9a3a967f8909c3a&ckck=1.
94. Bradley, M.K., C.K. Droney, and T.J. Allen, *Subsonic ultra green aircraft research. phase ii-volume i; truss braced wing design exploration.* National Aeronautics and Space Administration, Langley Research Center, 2015.
95. *ImageJ*. 2021, National Institutes of Health.
96. *M35J Technical Data Sheet*. Toray Composite Materials America, Inc.
97. Niu, C., *Airframe stress analysis and sizing*. 1997: AD Adaso/Adastra Engineering LLC.
98. *VisualAnalysis Edu*. Integrated Engineering Software.
99. Bradley, M.K. and C.K. Droney, *Subsonic Ultra Green Aircraft Research: Phase I Final Report. sl: NASA, 2011*. CR-2011-216847.
100. Arndt, C.M., et al., *Nondetermimistic Parameter Space Characterization of the Damage Tolerance of a Composite/Metal Structure*. 2022: Preprint arXiv: 2210.14054.
101. Ashby, M.F., *Materials Selection in Mechanical Design*. 4th ed. 2011, Oxford: Elsevier.
102. Baker, A.A., *Repair of cracked or defective metallic aircraft components with advanced fibre composites—an overview of Australian work.* Composite Structures, 1984. **2**(2): p. 153-181.
103. Baker, A.A., *A proposed approach for certification of bonded composite repairs to flight-critical airframe structure.* Applied Composite Materials, 2011. **18**(4): p. 337-369.
104. Baker, A.A., L.F. Rose, and R. Jones, *Advances in the bonded composite repair of metallic aircraft structure*. 2003: Elsevier.
105. Clark, R.J. and D.P. Romilly, *Bending of bonded composite repairs for aluminum aircraft structures: A design study.* Journal of aircraft, 2007. **44**(6): p. 2012-2025.
106. Colombi, P., A. Bassetti, and A. Nussbaumer, *Delamination effects on cracked steel members reinforced by prestressed composite patch.* Theoretical and applied fracture mechanics, 2003. **39**(1): p. 61-71.

107. Khan, S., S.K. Sarang, and I. Hiratsuka, *Study of bending strength for aluminum reinforced with epoxy composite.* SAE International Journal of Materials and Manufacturing, 2016. **9**(3): p. 781-787.
108. Kim, H.S. and D.G. Lee, *Optimal design of the press fit joint for a hybrid aluminum/composite drive shaft.* Composite structures, 2005. **70**(1): p. 33-47.
109. Buyukozturk, O., O. Gunes, and E. Karaca, *Progress on understanding debonding problems in reinforced concrete and steel members strengthened using FRP composites.* Construction and Building Materials, 2004. **18**(1): p. 9-19.
110. *Aviation Maintenance Technician Handbook*. 2012, Oklahoma City, OK: Airman Testing Standards Branch.
111. Wang, C., L. Rose, and R. Callinan, *Analysis of out-of-plane bending in one-sided bonded repair.* International Journal of Solids and Structures, 1998. **35**(14): p. 1653-1675.
112. Lee, J., M. Cho, and H.S. Kim, *Bending analysis of a laminated composite patch considering the free-edge effect using a stress-based equivalent single-layer composite model.* International journal of mechanical sciences, 2011. **53**(8): p. 606-616.
113. Goodmiller, G.R. and S.C. TerMaath. *Investigation of composite patch performance under low-velocity impact loading*. in *55th AIAA/ASMe/ASCE/AHS/SC Structures, Structural Dynamics, and Materials Conference*. 2014.
114. Seamone, A., A.M. Waas, and P. Davidson. *Experimental Analysis of Low Velocity Impact on Carbon Fiber Reinforced Polymer (CFRP) Composite Panels*. in *AIAA SCITECH 2022 Forum*. 2022.
115. Benyahia, F., et al., *Experimental and numerical analysis of bonded composite patch repair in aluminum alloy 7075 T6.* Materials & Design, 2015. **73**: p. 67-73.
116. Ouinas, D., B.B. Bouiadjra, and B. Serier, *The effects of disbonds on the stress intensity factor of aluminium panels repaired using composite materials.* Composite structures, 2007. **78**(2): p. 278-284.
117. Denney, J. and S. Mall, *Characterization of disbond effects on fatigue crack growth behavior in aluminum plate with bonded composite patch.* Engineering Fracture Mechanics, 1997. **57**(5): p. 507-525.
118. Smith, K.R., *Correlating Fracture Toughness and Surface Roughness for a Ductile Epoxy Adhered to Aluminum Substrates.* 2021.
119. Webb, L.J., A.B. Harman, and D. Mollenhauer. *Enhanced failure prediction of adhesively bonded composite clamped tapered beam specimens with manufacturing induced defects using discrete damage modelling*. in *AIAA SCITECH 2022 Forum*. 2022.
120. Ramji, M., R. Srilakshmi, and M.B. Prakash, *Towards optimization of patch shape on the performance of bonded composite repair using FEM.* Composites Part B: Engineering, 2013. **45**(1): p. 710-720.

121. Bouiadjra, B.B., et al., *Comparison between rectangular and trapezoidal bonded composite repairs in aircraft structures: a numerical analysis.* Materials & Design, 2011. **32**(6): p. 3161-3166.
122. Mall, S. and D. Conley, *Modeling and validation of composite patch repair to cracked thick and thin metallic panels.* Composites Part A: applied science and manufacturing, 2009. **40**(9): p. 1331-1339.
123. Ouinas, D., et al., *Progressive edge cracked aluminium plate repaired with adhesively bonded composite patch under full width disbond.* Composites Part B: Engineering, 2012. **43**(2): p. 805-811.
124. Hosseini-Toudeshky, H., et al., *Numerical and experimental fatigue crack growth analysis in mode-I for repaired aluminum panels using composite material.* Composites Part A: applied science and manufacturing, 2007. **38**(4): p. 1141-1148.
125. Chang, F.-K. and K.-Y. Chang, *A progressive damage model for laminated composites containing stress concentrations.* Journal of composite materials, 1987. **21**(9): p. 834-855.
126. Perugini, P., A. Riccio, and F. Scaramuzzino. *Three-dimensional progressive damage analysis of composite joints*. in *Proceedings of the eighth international conference on The application of artificial intelligence to civil and structural engineering computing*. 2001.
127. Donadon, M., et al., *A progressive failure model for composite laminates subjected to low velocity impact damage.* Computers & Structures, 2008. **86**(11-12): p. 1232-1252.
128. Bednarcyk, B.A., J. Aboudi, and S.M. Arnold, *Micromechanics modeling of composites subjected to multiaxial progressive damage in the constituents.* AIAA journal, 2010. **48**(7): p. 1367-1378.
129. Kashfuddoja, M. and M. Ramji, *An experimental and numerical investigation of progressive damage analysis in bonded patch repaired CFRP laminates.* Journal of Composite materials, 2015. **49**(4): p. 439-456.
130. Akterskaia, M., E. Jansen, and R. Rolfes. *Progressive failure analysis of stiffened composite panels using a two-way loose coupling approach including intralaminar failure and debonding*. in *2018 AIAA/ASCE/AHS/ASC Structures, Structural Dynamics, and Materials Conference*. 2018.
131. Sápi, Z., R. Butler, and A.T. Rhead. *Numerical prediction of failure in composite t-joints using progressive damage modelling*. in *2018 AIAA/ASCE/AHS/ASC Structures, Structural Dynamics, and Materials Conference*. 2018.
132. Jones, R., W. Chiu, and R. Smith, *Airworthiness of composite repairs: failure mechanisms.* Engineering Failure Analysis, 1995. **2**(2): p. 117-128.
133. Papanikos, P., et al., *Progressive damage modelling of bonded composite repairs.* Theoretical and Applied Fracture Mechanics, 2005. **43**(2): p. 189-198.

134. Shiravand, A. and M. Asgari, *Hybrid metal-composite conical tubes for energy absorption; theoretical development and numerical simulation.* Thin-Walled Structures, 2019. **145**: p. 106442.
135. Zhu, G., et al., *On crushing characteristics of different configurations of metal-composites hybrid tubes.* Composite Structures, 2017. **175**: p. 58-69.
136. Zheng, G., Z. Wang, and K. Song, *Energy absorption on metal-composite hybrid structures: Experimental and numerical simulation.* Thin-Walled Structures, 2020. **150**: p. 106571.
137. Shin, D.K., H.C. Kim, and J.J. Lee, *Numerical analysis of the damage behavior of an aluminum/CFRP hybrid beam under three point bending.* Composites Part B: Engineering, 2014. **56**: p. 397-407.
138. Nguyen, A.T., et al., *Loading, support and geometry effects for pin-reinforced hybrid metal-composite joints.* Composites Part A: Applied Science and Manufacturing, 2017. **98**: p. 192-206.
139. Action, J. and V. Goyal. *Design of a Fail-Safe Crack Arrested Test Specimen for Certification of Bonded Unitized Composite Structures*. in *AIAA SCITECH 2022 Forum*. 2022.
140. Finlay, J., et al. *Experimentally Validated Progressive Failure Modeling of Composite Pi Joints*. in *AIAA SCITECH 2022 Forum*. 2022.
141. Novak, J.K. and A.S. Selvarathinam. *A Comparison of Discrete Damage Modeling Methods: the Effect of Stacking Sequence on Progressive Failure of the Skin Laminate in a Composite Pi-joint Subject to Pull-off Load*. in *AIAA Scitech 2021 Forum*. 2021.
142. Heng, B. and S.C. TerMaath. *Prediction of Damage Tolerance in Metallic Structure Repaired with a Co-Cured Composite Patch*. in *2018 AIAA/ASCE/AHS/ASC Structures, Structural Dynamics, and Materials Conference*. 2018.
143. Arndt, C.M., et al. *Damage Tolerance Prediction for a Hybrid Composite/Metal Structure under Three Point Bending*. in *AIAA Scitech 2019 Forum*. 2019.
144. Kleemola, H. and M. Nieminen, *On the strain-hardening parameters of metals.* Metallurgical transactions, 1974. **5**(8): p. 1863-1866.
145. Turon, A., et al., *A damage model for the simulation of delamination in advanced composites under variable-mode loading.* Mechanics of materials, 2006. **38**(11): p. 1072-1089.
146. Benzeggagh, M.L. and M. Kenane, *Measurement of mixed-mode delamination fracture toughness of unidirectional glass/epoxy composites with mixed-mode bending apparatus.* Composites science and technology, 1996. **56**(4): p. 439-449.
147. Hart, D.C., E.P. Udinski, and J.M. Noland Jr., *CG Task Force Composite Patch Material Testing*. 2016, NSWCCD: Carderock, MD.

148. Mandell, J.F., S.-S. Wang, and F.J. McGarry, *The extension of crack tip damage zones in fiber reinforced plastic laminates.* Journal of Composite Materials, 1975. **9**(3): p. 266-287.
149. Hallett, S.R. and M.R. Wisnom, *Experimental investigation of progressive damage and the effect of layup in notched tensile tests.* Journal of Composite Materials, 2006. **40**(2): p. 119-141.
150. Johnson, A.F., A.K. Pickett, and P. Rozycki, *Computational methods for predicting impact damage in composite structures.* Composites Science and Technology, 2001. **61**(15): p. 2183-2192.
151. Johnson, A.F., *Modelling fabric reinforced composites under impact loads.* Composites Part A: Applied Science and Manufacturing, 2001. **32**(9): p. 1197-1206.
152. Turon, A., et al., *An engineering solution for mesh size effects in the simulation of delamination using cohesive zone models.* Engineering fracture mechanics, 2007. **74**(10): p. 1665-1682.
153. *DICE, Distribution-based Input for Computation Evaluations*. 2016, Naval Surface Warfare Center: Carderock, Bethesda, MD.
154. McKay, M., R. Beckman, and W. Conover, *Acomparisonof three methodsforselecting valuesofinputvariablesinthe analysisofoutputfrom acomputercode.* Technometrics, 1979. **21**(2): p. 239-245.
155. Shields, M.D. and J. Zhang, *The generalization of Latin hypercube sampling.* Reliability Engineering & System Safety, 2016. **148**: p. 96-108.
156. Rayas-Sánchez, J.E., *EM-based optimization of microwave circuits using artificial neural networks: The state-of-the-art.* IEEE Transactions on Microwave Theory and Techniques, 2004. **52**(1): p. 420-435.
157. *TensorFlow, Large-Scale Machine Learning on Heterogenous Systems*. 2015, Google Brain: Mountain View, CA.
158. Saltelli, A., S. Tarantola, and F. Campolongo, *Sensitivity analysis as an ingredient of modeling.* Statistical Science, 2000: p. 377-395.
159. Romo-Pérez, M., et al., *Sodium accumulation has minimal effect on metabolite profile of onion bulbs.* Plant Physiology and Biochemistry, 2021. **168**: p. 423-431.
160. Wang, Y., et al., *Testing rebound hardness for estimating rock properties from core and wireline logs in mudrocks.* Journal of Petroleum Science and Engineering, 2022. **210**: p. 109973.

Vita

Corey Michael Arndt was born in Pittsburgh, PA in December of 1993. He grew up with an aspiration with civil engineering and entered the class of 2016 at the Pennsylvania State University. Here he acquired a B.S. in Civil Engineering with a minor in Engineering Mechanics. During his undergraduate career he was granted the ability to work under two different research groups lead by Dr. Cannon and Dr. Rajabipour. After graduating Corey began working in Imler, PA designing metal buildings. With some encouragement from friends and family, he enrolled at the University of Tennessee, Knoxville to pursue a Ph.D. in Mechanical Engineering in 2018 and accepted a graduate research position under Dr. Stephanie TerMaath. He concurrently earned a M.S. in Mechanical Engineering with the Interdisciplinary Graduate Minor in Computational Sciences. Corey graduated from the University of Tennessee in December of 2022. He had accepted an offer for employment and began work in August of 2022 while finishing his Dissertation.